# STUDIES IN APPLIED AND FUNDAMENTAL QUANTUM MECHANICS: DUALITY, TOMOGRAPHY, CRYPTOGRAPHY AND HOLOGRAPHY

Eliot Bolduc

Thesis Submitted to the Faculty of Graduate and Postdoctoral Studies
In partial fulfillment of the requirements
for the degree of
Master of Science in Physics

Ottawa-Carleton Institute of Physics
Department of Physics
University of Ottawa

# Abstract

This thesis encompasses a collection of four pieces of work on wave-particle duality, weak-value-assisted tomography, high-dimensional quantum key distribution, and phase-only holograms. In the work on duality, we derive a novel duality relation, and we sketch a thought experiment that leads to an apparent violation of the duality principle. In the project on tomography, we perform a state determination procedure with weak values, and we study the accuracy of the method. In the quantum cryptography project, we optimize an experimental implementation of a quantum cryptography system where two parties share information with the orbital angular momentum degree of freedom of entangled photon pairs. Finally, in the work on holography, we establish the exact solution to the encryption of a phase-only hologram, and experimentally demonstrate its application to spatial light modulators. The four projects provide improvements on measurement procedures in applied and fundamental quantum mechanics.

# Résumé

Cette thèse comprend quatre projets portant soit sur les fondements ou les applications de la mécanique quantique. Ils portent notamment sur la dualité onde-particule, la tomographie d'états quantiques avec des valeurs faibles, la distribution de clefs quantiques en hautes dimensions, ainsi que sur les hologrammes à modulation de phase. En premier lieu, après la dérivation d'une nouvelle relation de dualité, nous expliquons une violation apparente de la dualité onde-particule. En deuxième lieu, nous appliquons une procédure de tomographie quantique sur un état de polarisation de la lumière en mesurant des valeurs faibles. En troisième lieu, nous implémentons un système de cryptographie quantique selon lequel deux interlocuteurs partagent de l'information avec le moment angulaire orbital de paires de photons intriqués. Finalement, nous démontrons la solution exacte à l'encodage simultané de la phase et de l'amplitude d'un mode spatial transverse dans un hologramme à modulation de phase.

# Contents

# List of Figures

# CV

## Publications:

1. J. Leach, **E. Bolduc**, D. J. Gauthier, and R. W. Boyd, "Secure information capacity of photons entangled in many dimensions," *Physical Review A*, vol. 85, no. 6, p. 060304, 2012

2. J. Z. Salvail, M. Agnew, A. S. Johnson, **E. Bolduc**, J. Leach, and R. W. Boyd, "Full characterization of polarization states of light via direct measurement," *Nature Photonics*, vol. 7, pp. 316–321

3. **E. Bolduc**, N. Bent, E. Santamato, E. Karimi, and R. W. Boyd, "Exact solution to simultaneous intensity and phase masking with a single phase-only hologram," *Optics Letters*, 2013, [Accepted, but not officially published before submission of the thesis]

## Conference Proceedings

1. **E. Bolduc**, J. Leach, and R. Boyd, "The secure information capacity of photons entangled in high dimensions," in *Quantum Information and Measurement*, Optical Society of America, 2012

2. **E. Bolduc**, J. Leach, and R. W. Boyd, "The secure information capacity of photons entangled in high dimensions," in *Frontiers in Optics 2012/Laser Science XXVIII*, p. FTh4B.7, Optical Society of America, 2012

3. **E. Bolduc**, J. Leach, F. Miatto, G. Leuchs, and R. Boyd, "How to achieve high visibility and high which-way information in a single experiment," in *Physics of Quantum Electronics*, 2013

# Statement of originality and collaborative contributions

To the best of his knowledge, the author states that the four projects described in this Master's thesis constitute original research in the field of physics. In the following paragraphs, we provide the collaborative contributions of each participant in the projects, which are presented in chronological order of start date.

The work on quantum cryptography described in chapter 4 was mainly done by Eliot Bolduc and Dr Jonathan Leach, who was a research assistant in the group of Prof. Robert W. Boyd at the time. J. Leach had the idea, initiated the work and designed the experiment. Both J. Leach and E. Bolduc performed the experiment and analyzed the data. E. Bolduc theoretically generalized the results. The work resulted in publication 1. All authors contributed to writing the paper.

Jeff Salvail, who was a Coop student at the time, initiated the work on tomography with weak values described in chapter 3. It resulted in publication 2. The experiment was designed by J. Salvail, A. Johnson, J. Leach and E. Bolduc. The experiment was performed mostly by J. Salvail and the results were also analyzed by J. Salvail. Megan Agnew and Allan Johnson, two undergraduate students at the time, helped in the experiment. All authors participated to writing the paper. E. Bolduc later theoretically elaborated on the accuracy of the method.

Prof. R. W. Boyd initiated the work of chapter 2. J. Leach had an intuitive explanation for the apparent violation reported by Menzel *et al.* [7]. E. Bolduc later derived a novel duality relation and precisely explained their results.

Ebrahim Karimi, a post-doctoral fellow, had the idea and derived the theory of the hologram encryption method of chapter 5. E. Karimi and E. Bolduc designed the experiment. E. Bolduc wrote the hologram encryption programs. E. Bolduc and Nico-

las Bent performed the experiment. All authors contributed to writing publication 3.

# Chapter 1

# Introduction

The author decided to take part in four projects which developed in the course of his Master's degree. Each project was conducted independently of the others, and successfully completed. They all provide advances in fundamental or applied quantum mechanics. In each body of work, we study the impact of the measurement procedure on the outcome of an experiment and suggest or implement possible improvements. Instead of the chronological order, we present the four projects in order of the more fundamental to the more applied: wave-particle duality in the presence of an environment, weak-value-assisted tomography, high-dimensional quantum key distribution and modal encryption of phase-only holograms.

According to wave-particle duality, a building block of fundamental quantum mechanics, the wave-like and particle-like behaviors of a quantum state in an interferometer are mutually exclusive. Wave-like behavior refers to the observation of an interference pattern, while particle-like behavior alludes to the which-way information. If this information is completely available, no interference pattern can be observed. In chapter 2, we derive a new duality relation that bounds the visibility of an interference pattern and the which-way knowledge in an interferometer where two paths are coupled to an auxiliary system. We then show how biased sampling of a subset of the auxiliary system can lead to an apparent violation of the duality principle. This work improves the current understanding of duality and helps to solve the case of a controversial experiment on fundamental quantum mechanics [7, 8].

The experimental determination of a quantum state is in general not a straightforward task because a quantum state-vector is specified with complex coefficients, but the outcome of a measurement is always real-valued. In standard quantum state to-

mography, the state-vector is unambiguously identifiable by the real-valued outcomes of an informationally complete set of projective measurements. Alternatively, one can retrieve the state-vector by measuring weak values instead of projections [9, 10]. In chapter 3, we provide the proof-of-principle demonstration of weak-value-assisted tomography of a two-dimensional state, namely, the polarization state of light. We also study the accuracy of the method as a function of the weakness of the measurements. The method is very direct in that the coefficients of the state under study are proportional to the weak values, and no post-measurement processing is required.

Quantum key distribution (QKD) protocols offer the holy grail of cryptography: absolute security in a communication channel between two parties. The laws of quantum mechanics forbid perfect cloning of a state, and, as a consequence, eavesdropping inherently introduces noise into a QKD system. Absolute security is only ensured when the observed noise level is below the eavesdropping-caused threshold. In a realistic QKD system, noise is always present, and for the sake of absolute security, it must be considered as coming from an eavesdropper. In chapter 4, we discuss our implementation of important elements of a secure quantum communication channel with photons entangled in the orbital angular momentum (OAM) degree of freedom. In principle, the OAM space is discrete and infinite, and the information encoded in a photon pair is unbounded. In practice, we consider a finite subset of this infinite space. The ability to generate a high number of different OAM modes with high signal to noise ratio is technologically challenging. Given a set of experimental parameters such as detection efficiency and photon production rate, we find the OAM subspace dimension that maximizes the secure information shared between two parties. This work opens up the way for efficient implementations of QKD systems in high dimensions.

Computer generated phase-only holograms, such as spatial light modulators, can be used to control both the phase and the intensity profile of an optical beam. An important application of phase-only holograms is the generation of arbitrary transverse spatial modes. Numerous encryption methods already exist to perform such a task, but their theoretical result is always an approximation to the desired transverse spatial mode. In chapter 5, we provide the exact solution to simultaneous phase and intensity encryption of a phase-only hologram, such that the result is in principle exactly equal to the desired mode. We expect that our method will have a high

impact in optical communications, quantum tomography of transverse spatial modes and experiments in fundamental quantum mechanics.

# Chapter 2

# A fair-sampling perspective on an apparent violation of duality

## 2.1 Introduction

In the event in which a quantum mechanical particle can take two possible paths, the duality principle states that "the observation of an interference pattern and the acquisition of which-way information are mutually exclusive" [11].

### 2.1.1 Duality and its apparent violation

Since Bohr first noticed in 1927 the complementary behaviors of interference and which-way information in the two-slit experiment [12], numerous studies have reenforced the duality principle [11] [13] [14] [15]. It was confirmed by experimental evidence with massive particles like neutrons [16], with atoms [17] and even with $C_{60}$ molecules of picometer-size de Broglie wavelength [18]. Having passed every test, duality has indubitably become a solid fundamental and universal principle of quantum mechanics.

Recently, however, Menzel *et al.* reported an experimental "apparent violation" of the duality principle [7] [8]. They implemented Young's two-slit experiment with photons entangled in position and momentum generated through spontaneous parametric downconversion (SPDC), and measured both an interference pattern with high visibility and high which-way information in a single experiment. Motivated by explaining this surprising result, we analyze duality with a fair sampling perspective.

### 2.1.2 Fair sampling

The concept of fair sampling has received much of attention in the context of tests of the Bell inequalities and non-locality. In order to rule out locality completely, one would ideally avoid having to make any assumption, including the fair-sampling assumption, which states that the measured sample of particles is representative of the ensemble under study. To ensure that this is the case, the detection efficiency must be above a particular threshold [19], which depends on the type of Bell inequality, and all the measurements must be performed without bias. In other words, all relevant subsets of an ensemble must be sampled with equal probability. The result of a test of fundamental quantum mechanics performed with biased sampling bears meaning only when the measurement configurations are all specified and taken into account.

### 2.1.3 Summary

In this work, we derive the tightest possible relation between which-alternative knowledge[1] and average visibility of the corresponding interference pattern in the presence of an environment, an improvement on the bound of the known inequalities. We then study the effect of biased sampling on tests of the duality principle. We demonstrate how to use our relation by applying it to a thought experiment of our making, inspired by that of Menzel *et al.*. We also show that biased sampling causes an apparent violation of the duality principle.

## 2.2 The duality relations

A duality relation bounds the visibility of an interference pattern and the corresponding available which-alternative information in an interferometer. Young's two-slit experiment is one of many ways to produce the experimental conditions in which an interference pattern and which-way knowledge can be obtained. Here, we restrict ourselves to a two-alternative system, where the alternatives can correspond to any degree of freedom: two arms of an interferometer, two slits, orthogonal polarizations or two orbital angular momentum states for instance. Without specifying any degree of freedom, we consider a pure normalized two-alternative quantum state of the form

[1]The term "which-alternative" is more general than "which-way" in that it applies to any degree of freedom.

$|\psi\rangle = \lambda_1|1\rangle + \lambda_2|2\rangle$, where $\lambda_1$ and $\lambda_2$ are the complex amplitudes of alternatives 1 and 2.

### 2.2.1 The Greenberger-Yasin relation

There are two distinct ways of gaining which-alternative information, namely, by prediction and retrodiction. We review the former, and then derive a new duality relation for the latter. One can partially *predict* the outcome of a which-alternative measurement if a state is prepared such that a particular alternative is more likely than the other. The prediction is not necessarily perfect, but a guess on the more probable option yields more correct than wrong results. Greenberger and Yasin quantify the which-alternative information for a pure state $|\psi\rangle$ with the positive difference between the probabilities of occurence, $\mathcal{P} = ||\lambda_1|^2 - |\lambda_2|^2|$ [16], a quantity now known as *predictability*. It corresponds to one's ability to predict the outcome of a which-alternative measurement in the basis $\{|1\rangle, |2\rangle\}$. The fact that only one outcome is possible for any one measurement is usually interpreted as particle-like behavior, a concept that owes its origins to pre-quantum physics. The complementary quantity that brings to light the wave-like behavior of the state is the visibility of the interference pattern. The visibility is obtained by projecting $|\psi\rangle$ onto the superposition state $(|1\rangle + \mathrm{e}^{\imath\phi}|2\rangle)/\sqrt{2}$, where $\phi$ is a phase that is scanned to produce the interference pattern. The visibility of the resulting interference pattern is given by $\mathcal{V} = 2|\lambda_1\lambda_2|$. For a pure two-alternative state, we have the equality [16],

$$\mathcal{P}^2 + \mathcal{V}^2 = 1. \tag{2.2.1}$$

In the presence of noise or a statistical mixture of two alternatives, the coherence is reduced and the above relation becomes an inequality: $\mathcal{P}^2 + \mathcal{V}^2 \leq 1$.

### 2.2.2 The Englert-Bergou relation

In addition to the principal two-alternative state, consider the existence of an *environment* [11] or an *auxiliary system* [14]; the two terms are equivalent, but employed by different authors. If the two-alternative state is coupled to an auxiliary system, the latter contains information about the former, and which-alternative is available through retrodiction. This concept is better explained through an example. Notably,

Schwindt *et al.* have experimentally coupled each path of a Mach-Zehnder interferometer to arbitrary polarization states with birefringent wave plates, making the which-way information accessible through a measurement of the polarization [20]. In this experiment, the Mach-Zehnder interferometer and the polarization degree of freedom played the roles of the two-alternative system and the auxiliary system, respectively. A measurement on the auxiliary system yields which-alternative information by retrodiction, since the collapse of the two-alternative state occurs before obtainment of the which-way information [14]. When the auxiliary system is known, the composite state can generally be broken into its parts, and each state of the auxiliary system is associated with a probability of occurrence, which-alternative information and interference pattern, see Fig. 1 of reference [15] for a pictorial description.

In the basis $\{|a_i\rangle\}$ of $D$ dimension for the auxiliary system, the state of the the composite system is written $|\Psi\rangle = \sum_{i=1}^{D} \alpha_i |\psi_i, a_i\rangle$, where the complex amplitudes $\alpha_i$ are normalized and $|\psi_i\rangle = \lambda_{1,i}|1\rangle + \lambda_{2,i}|2\rangle$. The which-alternative knowledge[2] associated to the composite system is given by the statistical average of the predictabilities, which average is performed on the auxiliary states $|a_i\rangle$: $\langle\mathcal{P}\rangle = \sum_{i=1}^{D} p_i \mathcal{P}_i$, where $p_i = |\alpha_i|^2$, the probability of occurrence of the auxiliary state $|a_i\rangle$ and $PP_i$ is the predictability associated with the state $|a_i\rangle$. By virtue of the pure states $|\psi_i\rangle$, the quantities $\langle\mathcal{P}^2\rangle = \sum_{i=1}^{D} p_i \mathcal{P}_i^2$ and $\langle\mathcal{V}^2\rangle = \sum_{i=1}^{D} p_i \mathcal{V}_i^2$ sum to unity:

$$\langle\mathcal{P}^2\rangle + \langle\mathcal{V}^2\rangle = 1. \tag{2.2.2}$$

In the case where the auxiliary system is parametrized by a continuous variable, the sums are replaced by integrals. The Englert-Bergou inequality between the which-alternative knowledge and the average visibility is given by [15]: $\langle\mathcal{P}\rangle^2 + \langle\mathcal{V}\rangle^2 \leq 1$, which holds even in the case of partly or completely mixed states. We have used the fact that $\langle\mathcal{P}\rangle^2 \leq \langle\mathcal{P}^2\rangle$ and $\langle\mathcal{V}\rangle^2 \leq \langle\mathcal{V}^2\rangle$.

### 2.2.3 Our new tight duality relation

In order to find an *equality* for the which-alternative knowledge and the average visibility, the physically relevant quantities, we make use of the variances of each distribution: $\sigma_{\mathcal{P}}^2 = \sum_{i=1}^{D} p_i(\mathcal{P}_i - \langle\mathcal{P}\rangle)^2$ and $\sigma_{\mathcal{V}}^2 = \sum_{i=1}^{D} p_i(\mathcal{V}_i - \langle\mathcal{V}\rangle)^2$. From Eq. 2.2.2

[2] In reference [15], the notation for which-alternative knowledge is $\mathcal{K}$ instead of $\langle\mathcal{P}\rangle$.

and the identities $\sigma_{\mathcal{P}}^2 = \langle \mathcal{P}^2 \rangle - \langle \mathcal{P} \rangle^2$ and $\sigma_{\mathcal{V}}^2 = \langle \mathcal{V}^2 \rangle - \langle \mathcal{V} \rangle^2$, it follows that

$$\langle \mathcal{P} \rangle^2 + \langle \mathcal{V} \rangle^2 = 1 - \sigma_{\mathcal{P}}^2 - \sigma_{\mathcal{V}}^2. \tag{2.2.3}$$

Since predictability and visibility are bounded between 0 and 1, each variance can take a maximum value of 1/4. The RHS of Eq. 2.2.3 is thus inherently greater or equal to 1/2. In the presence of noise or uncontrolled coupling to the environment, the RHS of Eq. 2.2.3 becomes an upper bound to the LHS, which upper bound is as tight as possible.

Eq. 2.2.3 holds only when all states of the environment $\{|a_i\rangle\}$ are sampled with equal probability. Since the environment is comprised of $D$ states, the sampling probability for any state $|a_i\rangle$ should be $1/D$. When this part of the fair sampling assumption is reduced, the measured statistics do not represent the state at hand and the RHS of Eq. 2.2.3 no longer bounds its LHS. In particular, this occurs when selecting only a subset of the auxiliary system while rejecting the rest. For instance, one could only measure the subset which corresponds to the highest predictability $\mathcal{P}_{\max}$ and also the one corresponding to the maximum visibility $\mathcal{V}_{\max}$. The maximum values $\mathcal{P}_{\max}$ and $\mathcal{V}_{\max}$ are in general from different subsets of the environment. For non-zero variances, the maximum value in each distribution is greater than its respective average value: $\mathcal{P}_{\max} > \langle \mathcal{P} \rangle$ and $\mathcal{V}_{\max} > \langle \mathcal{V} \rangle$. Since the quantity $(\mathcal{P}_{\max}^2 + \mathcal{V}_{\max}^2)$ can in principle approach 2, it is possible to observe both high predictability and high visibility in a single experiment. This can appear to be a violation of the duality principle, but it rather is a consequence of biased sampling in the measurement of which-alternative information and visibility.

## 2.3 A theoretical example of an apparent violation

The table is now set to show the conditions that lead to an apparent violation of duality in the context of a realistic experiment. We build a thought experiment inspired by the work of Menzel *et al.*. In summary, we start from a two-photon state generated through SPDC. One of the photons traverses a two-slit mask, while the other is used to measure the which-slit information. We then calculate the two-dimensional interference pattern in the far-field of the mask given that partial which-slit information is acquired. In the two-dimensional interference pattern, one of the

dimensions acts as an auxiliary system. The visibility of the interference pattern is dependent on the position on one of the axes. We calculate the quantities appearing in Eq. 2.2.3 for a given set of experimental parameters and show the impact of biased sampling of a subset of the auxiliary system on the outcome of the thought experiment.

### 2.3.1 The theory of degenerate spontaneous parametric down-conversion

For our purposes, it suffices to consider the SPDC process with a type I crystal, whose theoretical description is simpler than that of a type II crystal. When there is nearly no birefringent walk-off compared to the pump diameter, the two-photon transverse spatial mode function of degenerate SPDC has a simple analytical form [21] [22]. As a function of the transverse wavevectors of the signal $\mathbf{p_s}$ and idler $\mathbf{p_i}$ photons with $\mathbf{p} = p_x\hat{\mathbf{x}} + p_y\hat{\mathbf{y}}$, the single-frequency two-photon mode function is given by

$$\Phi(\mathbf{p_s}, \mathbf{p_i}) = N\,\tilde{E}\left(\mathbf{p_s} + \mathbf{p_i}\right)\,\tilde{F}\left(\frac{\mathbf{p_s} - \mathbf{p_i}}{2}\right), \tag{2.3.1}$$

where $N$ is a normalization constant, $\tilde{E}(\mathbf{p})$ is the angular spectrum of the pump laser, and $\tilde{F}$ is the phase-matching function. Under the assumption that the transverse wavevectors of the signal and idler photons are much smaller than their total wavevectors[3], the phase-matching function is of the form $\tilde{F}(\mathbf{p}) = \mathrm{sinc}(\varphi + L\,|\mathbf{p}|^2/k_p)$, where $\varphi$ is the phase mismatch parameter, $L$ is the thickness of the crystal and $k_p$ is the wavevector of the pump inside the crystal.

Because of momentum conservation, the signal and idler photons are anti-correlated in transverse wavevector space. The momentum correlations are mostly determined by the angular spectrum of the pump, while the phase-matching function dictates the general shape of the two-dimensional probability distribution of the individual photons, which we shall refer to as "the singles". If the pump beam is collimated and has infinite width at the crystal, its angular spread approaches the Dirac distribution $\delta(\mathbf{p_s} - \mathbf{p_i})$, a plane wave. In this limit, it is easy to show that the intensity profile of the singles in the far-field of the crystal is exactly given by $|\tilde{F}(\mathbf{p_{s,i}})|^2$, where $\mathbf{p_{s,i}}$ is

[3]This is known as the paraxial approximation. In our thought experiment below, we have $|\mathbf{p_s}|/|\mathbf{k_s}| \approx |\mathbf{p_i}|/|\mathbf{k_i}| \approx 0.07$, where $k_s$ ($k_i$) is the total wavevector of the signal (idler) photon.

the transverse wavevector of either the signal or the idler photon.

In order to describe the position correlations in coordinate space, we perform a 4-dimensional Fourier transform on the two-photon mode function: $\Psi(\mathbf{r_s}, \mathbf{r_i}) = \mathrm{FT}[\Phi(\mathbf{p_s}, \mathbf{p_i})]$, where $\mathbf{r} = r_x\hat{\mathbf{x}} + r_y\hat{\mathbf{y}}$ is the transverse coordinate in the plane of the crystal. Since the mode function in wavevector space is separable in $(\mathbf{p_s} + \mathbf{p_i})$ and $(\mathbf{p_s} - \mathbf{p_i})$, the mode function at the output facet of the crystal is written [23] [24] [25]

$$\Psi(\mathbf{r_s}, \mathbf{r_i}) = N' E(\mathbf{r_s} + \mathbf{r_i})\, F(\mathbf{r_s} - \mathbf{r_i}), \tag{2.3.2}$$

where $N'$ is a normalization constant, $E(\mathbf{2r})$ is the transverse spatial mode of the pump at the crystal and $F(\mathbf{r})$ is the phase-matching function in coordinate space: $F(\mathbf{r}) = (2\pi)^{-1} \int \mathrm{sinc}(\varphi + L\,|\mathbf{p}|^2/k_p) \mathrm{e}^{-\imath \mathbf{p}\cdot\mathbf{r}}\, d\mathbf{p}$. If the phase mismatch parameter is different from zero, $\varphi \neq 0$, this integral has no known analytical solution and has to be performed numerically. Its result determines the position correlations between the signal and idler photons. In the limit of a crystal with an infinitely small thickness, the phase-matching function in coordinate space approaches a Dirac distribution, $(F(\mathbf{r}) \to \delta(\mathbf{r}))$. In this limit, the signal and idler photons are perfectly correlated in coordinate space, and the general shape of the singles is exactly given by the intensity profile of the pump at the crystal. However, when the thickness of the crystal is of the same order of magnitude as the features in the transverse intensity profile of the pump, the latter appears smeared out in the distribution of the singles[4] [21].

### 2.3.2 Theoretical description of our thought experiment

In our thought experiment, we use a two-slit mask with a slit separation $d$ in the image plane of the output facet of the crystal on the signal photon side. Upon measurement of the idler photon position, the correlations allow one to gain knowledge about which slit the signal photon traverses *while* measuring the interference pattern in the far-field of the two-slit mask. We model the mask with the transmission function $W(r_{s,y}) = T(r_{s,y}) + B(r_{s,y})$, where $T$ and $B$ stand for the "top" and "bottom" slits and correspond to rectangle functions of width $\Delta$ at positions $d/2$ and $-d/2$,

[4] Fig. 2.7 shows the singles for an $\mathrm{HG}_{01}$ pump mode which width is comparable to the width of the correlations. The intensity profile of the singles does not vanish in the center because of the smearing out effect, which is not due to imperfect imaging, but to the large thickness of the crystal. We give more details on this subject in section 2.5.2.

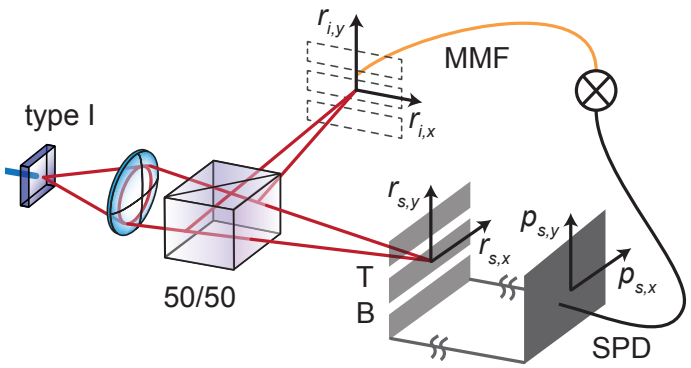


Figure 2.1: Our thought experiment, inspired by Menzel *et al.*. Photon pairs entangled in position and momentum are generated through degenerate SPDC with a type I crystal and a wide Gaussian pump mode. The signal and idler photons are separated by a 50/50 beam-splitter. On the path of the signal photon, the plane of the crystal is imaged with unit magnification to the plane of a two-slit mask made of slit T at $r_{s,y} = d/2$ and slit B at $r_{s,y} = -d/2$. While the signal photon traverses the mask, the idler photon is collected by an optical fiber (MMF), whose input facet is in the image plane of the crystal and centered at $r_{i,y} = d/2$ and $r_{i,x} = 0$. Through position correlations, we gain which-slit information of the signal photon upon detection of the idler photon. We collect the signal photons in the far-field of the mask with a scanning point detector (SPD). All measurements are performed in coincidence, such that the interference pattern of the signal photons is conditional on the detection of idler photons. In a real experiment, interference filters would be placed before the detectors to ensure degenerate SPDC.

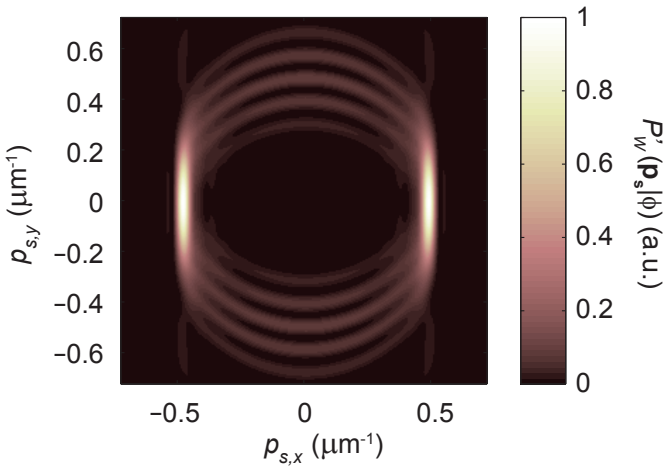


Figure 2.2: Theoretically predicted interference pattern of the signal photons in the far-field of the two-slit mask conditioned on the detection of idler photons: $P'_W(\mathbf{p_s}|\phi_i)$.

respectively[5]. The unnormalized two-photon mode function after the mask is given by $\Psi_S(\mathbf{r_s}, \mathbf{r_i}) = \Psi(\mathbf{r_s}, \mathbf{r_i})S(r_{s,y})$, where $S$ can be replaced by $W$, $T$ or $B$. The single-slit amplitudes $\Psi_T(\mathbf{r_s}, \mathbf{r_i})$ and $\Psi_B(\mathbf{r_s}, \mathbf{r_i})$ are needed in the thorough analysis of the test of the duality principle and are physically obtainable by blocking the bottom slit or the top slit, respectively. As we are interested in the joint probability of the signal photon being detected in the far-field of the mask and the idler photon in the near-field of the crystal, we perform a Fourier transform on the signal photon: $\Psi'_S(\mathbf{p_s}, \mathbf{r_i}) = (2\pi)^{-1} \int d\mathbf{r}\, \Psi_S(\mathbf{r}, \mathbf{r_i})\, \mathrm{e}^{\imath \mathbf{r}\cdot\mathbf{p_s}}$.

The idler photon is detected with a multimode fiber of width $w_f$ at position $(r_{i,x} = 0, r_{i,y} = d/2)$. We model this fiber with a Gaussian function: $\phi_i(\mathbf{r_i}) = \exp[-(r_{i,x}^2 + (r_{i,y} - d/2)^2)/(2w_f^2)]$. Upon detection of an idler photon, the conditional distributions of the signal photon after the mask in coordinate space and wavevector space are respectively written

$$P_S(\mathbf{r_s}|\phi) = N_P \int d\mathbf{r'_i}\, |\Psi_S(\mathbf{r_s}, \mathbf{r'_i})\, \phi_i(\mathbf{r'_i})|^2 \quad \text{and} \tag{2.3.3}$$

$$P'_S(\mathbf{p_s}|\phi) = N_P \int d\mathbf{r'_i}\, |\Psi'_S(\mathbf{p_s}, \mathbf{r'_i})\, \phi_i(\mathbf{r'_i})|^2\,, \tag{2.3.4}$$

where the normalization constant is given by $N_P^{-1} = \int\int d\mathbf{r'_s} d\mathbf{r'_i}\, |\Psi_W(\mathbf{r'_s}, \mathbf{r'_i})\, \phi_i(\mathbf{r'_i})|^2$.

[5]We chose the letter $W$ for the two-slit mask because it looks like what it represents: two slits with light diffracting out.

In view of the duality relations, the probability distribution $P'_W(\mathbf{p_s}|\phi_i)$ is comprised of one main degree of freedom and one that belongs to the environment: the vertical and horizontal directions, respectively. In general, the visibility of the interference pattern depends on the degree of freedom of the environment and can thus vary as a function of $p_{s,x}$. In their experiment, Menzel *et al.* selected one particular value of $p_{s,x}$ for the observation of the interference pattern, which, as we will show, happens to correspond to the maximum value of the visibility $\mathcal{V}_{\max}$. For the which-alternative measurement however, they acquired the *average* predictability by measuring the two-dimensional position correlations in coordinate space, that is in the plane of the slit. In our formalism, the average predictability in coordinate space is expressed as

$$\langle \mathcal{P} \rangle = \int d\mathbf{r'_s} \, |P_T(\mathbf{r'_s}|\phi_i) - P_B(\mathbf{r'_s}|\phi_i)|. \tag{2.3.5}$$

We rather obtain the average predictability in wavevector space, which allows us to retrieve the which-alternative knowledge in the same basis as the visibility. We retrieve $P'_T(\mathbf{p_s}|\phi_i)$ and $P'_B(\mathbf{p_s}|\phi_i)$ by way of sequentially blocking slit T and B. We then integrate the distributions in wavevector space over the main degree of freedom, $p_y$, and obtain the marginal probability distributions $M_T(p_{s,x}) = \int dp'_{s,y} P'_T(p_{s,x}, p'_{s,y}|\phi_i)$ and $M_B(p_{s,x}) = \int dp'_{s,y} P'_B(p_{s,x}, p'_{s,y}|\phi_i)$. For brevity, we henceforth omit writing the argument $p_{s,x}$. The marginal signal probability distribution for the two slits simultaneously in the same basis is $M_W = M_T + M_B$. Predictability and visibility can both be expressed as a function of $p_{s,x}$: $\mathcal{P} = |M_T - M_B|/M_W$ and $\mathcal{V} = 2\sqrt{|M_T M_B|}/M_W$. The average predictability and average visibility are respectively given by

$$\langle \mathcal{P} \rangle = \int dp_{s,x} \, |M_T - M_B| \quad \text{and} \tag{2.3.6}$$

$$\langle \mathcal{V} \rangle = \int dp_{s,x} \, 2\sqrt{|M_T M_B|} \, . \tag{2.3.7}$$

Because the which-way knowledge is independent of the basis chosen to perform its measurement, the two ways of retrieving it are equivalent. The last quantities left to find are the following variances:

$$\sigma^2_{\mathcal{P}} = \int dp_{s,x} \, M_W \, (\mathcal{P} - \langle \mathcal{P} \rangle)^2 \quad \text{and} \tag{2.3.8}$$

$$\sigma^2_{\mathcal{V}} = \int dp_{s,x} \, M_W \, (\mathcal{V} - \langle \mathcal{V} \rangle)^2. \tag{2.3.9}$$

Using Eq. 2.3.2 to 2.3.9, we check that Eq. 2.2.3 is satisfied with a numerical example. In our model, the pump spatial transverse mode does not play a key role and need not be of any special kind. We thus consider a plane-wave, which consists in a very good approximation to a collimated Gaussian beam at the crystal. The pump term in Eq. 2.3.2 can then be ignored, making the SPDC mode function completely determined by the phase-matching function. For the numerical calculations, the set of parameters that we use is $\{\varphi = -19,\ L = 2\text{ mm}, d = 70\ \mu\text{m},\ \Delta = d/4\ \mu\text{m},\ w_f = 10\ \mu\text{m},\ n = 1.65,\ \lambda_p = 405\text{ nm}\}$, with $k_p = 2\pi n/\lambda_p$.

Since there is no known analytical form for the phase-matching function, we compute Eq. 2.3.3 and 2.3.4, for $S = \{W, T \text{ and } B\}$, numerically. The two-dimensional interference pattern $P'_W(\mathbf{p_s}|\phi_i)$ is shown in Fig. 2.2. The visibility is strongly dependent on the degree of freedom of the environment, $p_{s,x}$. This strong dependence is explained by the fact that the sinc term in the phase-matching function is non-separable in $p_x$ and $p_y$. This effect can be fully described with classical optics. For instance, consider a two-dimensional classical transverse spatial mode $\Omega(p_x, p_y)$, which is sent to the two-slit mask $W(r_y)$. Through the convolution theorem, the resulting two-dimensional interference pattern $I(p_x, p_y)$ is determined by the convolution of the input mode in wavevector space with the Fourier transform of the two-slit mask: $I(p_x, p_y) \propto |\Omega(p_x, p_y) * \text{FT}[W(r_y)](p_y)|^2$. Hence, the resulting interference pattern at a given value of $p_x$ only depends on the input distribution at the same value of $p_x$. If the input mode is non-separable in its two arguments, the input distribution along $p_y$ depends on $p_x$ and so does the interference pattern.

We can now compute the relevant quantities: $\{\langle\mathcal{P}\rangle = 0.816,\ \langle\mathcal{V}\rangle = 0.331,\ \mathcal{V}_{\max} = 0.982,\ \sigma^2_{\mathcal{P}} = 0.077,\ \sigma^2_{\mathcal{V}} = 0.148\}$. The total marginal probability, the predictability and the visibility as a function of $p_{s,x}$ are shown in Fig. 2.3. In our example, we have $\langle\mathcal{P}\rangle^2 + \langle\mathcal{V}\rangle^2 = 1 - \sigma^2_{\mathcal{P}} - \sigma^2_{\mathcal{V}} = 0.775$, which is consistent with Eq. 2.2.3. The apparent violation occurs only when we consider the visibility at $p_{s,x} = 0$ instead of the average visibility. Here, the biased sampling relation $\mathcal{B} = \langle\mathcal{P}\rangle^2 + \mathcal{V}^2_{\max}$ reaches a value of 1.630, which is more than twice as much as the limit for the averages, thus showing high which-alternative information and high visibility in a single experiment. It is this quantity $\mathcal{B}$ that can be deduced from the reported results of Menzel *et al.*. The apparent violation of the duality principle is due to the fact that they (and we) favor one specific subset of the environment, $p_{s,x} = 0$, which corresponds to the

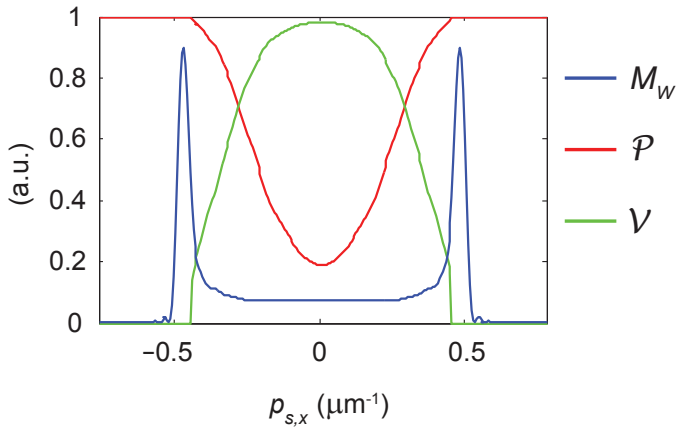


Figure 2.3: Plot of (blue) the probability distribution $M_W(p_{s,x})$ of the signal photons in wavevector space conditional on the detection of idler photons. The scale for $M_W(p_{s,x})$ has been modified to fit the distribution on the same graph as the two other curves, which correspond to (red) the predictability $\mathcal{P}$ and (green) the visibility $\mathcal{V}$ as a function of the degree of freedom of the environment. These quantities satisfy the equality $\mathcal{P}^2 + \mathcal{V}^2 = 1$ for all values of $p_{s,x}$.

maximum visibility $\mathcal{V}_{\max}$ in the distribution. This is a form of biased sampling, or a break-down of the fair sampling assumption.

The measured subset for the measurement of the visibility must have a low probability of occurrence for $\mathcal{B}$ to surpass Eq. 2.2.3 by a large amount. Notably, in the ideal case where i) a single state of the environment has vanishing probability and a corresponding value of $\mathcal{V}_{\max} = 1$, and ii) all other visibilities are zero, $\mathcal{B}$ approaches the value of 2. As indicated in Fig. 2.3, the probability of finding a signal photon where the visibility is the highest, the region around $p_{s,x} = 0$, is indeed low albeit non-zero. This low probability of occurrence is an important factor contributing to the apparent violation of the duality principle.

## 2.4 Conclusions

In conclusion, we have derived the tightest possible relation between the average predictability and the average visibility of a two-alternative system in the presence of an environment. This duality relation proved useful in the analysis of an apparent violation of the duality principle, similar to the one reported by Menzel *et al.*. The

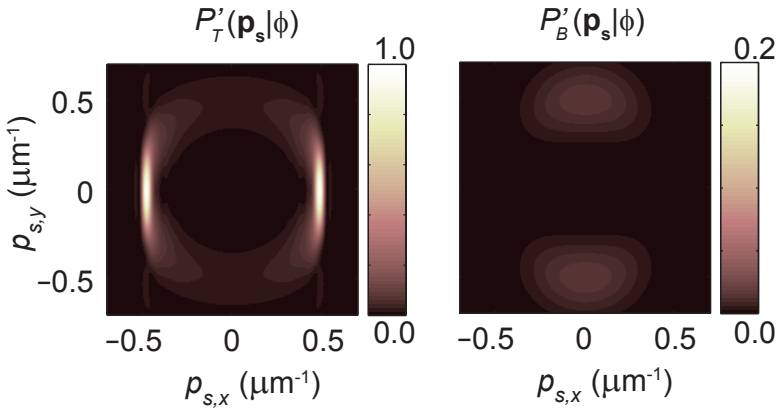


Figure 2.4: Far-field distribution of the signal photons conditional on the detection of idler photons when a) slit B is blocked and b) slit T is blocked. The photons arriving at position $|p_{s,x}| = 0.5\ \mu\text{m}^{-1}$ almost exclusively come from slit T, whereas photons arounds $|p_{s,x}| = 0\ \mu\text{m}^{-1}$ do not carry much which-slit information, if any, which is consistent with the observed high visibility at this position in the superposition state distribution $P'_W(\mathbf{p_s}|\phi_i)$ in Fig. 2.2. The scale of the distribution of $P'_B(\mathbf{p_s}|\phi_i)$ is divided by 5 for better image contrast.

selection of one particular subset of the environment for the measurement of the visibility is the key to understand this apparent violation. According to our analysis, the duality principle is safe and sound, but our new duality relation remains to be thoroughly tested.

## 2.5 Supplementary material

### 2.5.1 Details of our numerical calculations

The transverse two-photon mode function has four degrees of freedom in coordinate space and four corresponding degrees of freedom in wavevector space: $\{\mathbf{r_s}, \mathbf{r_i}\}$ and $\{\mathbf{p_s}, \mathbf{p_i}\}$. Numerical manipulation of the two-photon mode function can be computationally intensive. For example, if one wants to specify each degree of freedom with 512 pixels each, the total number of discrete positions is greater than $10^{10}$, which is too much for a normal computer to handle. We thus manipulate small subsets of the whole state at a time. For the calculation of $P'_W(\mathbf{p_s}|\phi)$ in Fig. 2.2 for instance, we numerically specify the amplitude distribution of $\Psi_W(\mathbf{r_s}, \mathbf{r_i} = \mathbf{r'_i})$ for one specific value of $\mathbf{r'_i}$ and perform a fast Fourier transform on this high resolution distribution,

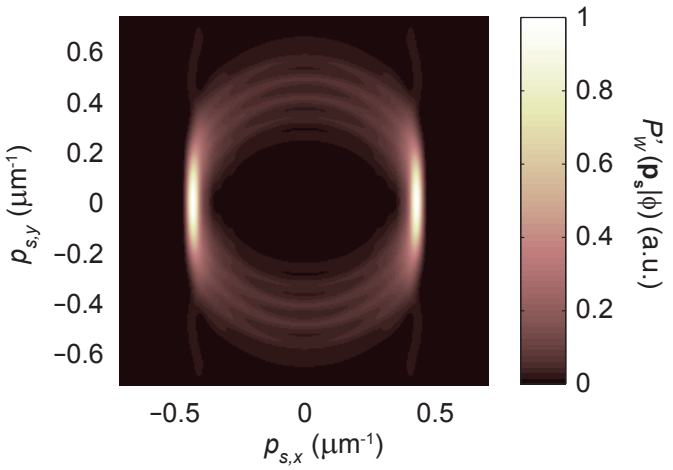


Figure 2.5: Conditional interference pattern, $P'_W(\mathbf{p_s}|\phi_i)$, obtained in our thought experiment with an $HG_{01}$ pump mode. The visibility of the interference pattern is lower than for the $HG_{00}$ pump mode (Fig. 2.2). While the number of bright fringes on the top or bottom of the ring is odd for the $HG_{00}$ pump mode, it is even for the $HG_{01}$ pump mode.

which yields $\Psi'_W(\mathbf{p_s}, \mathbf{r_i} = \mathbf{r'_i})$. We repeat the process for all values of $\mathbf{r'_i}$; we truncate at $|\mathbf{r_i}| = 3w_f$, where $w_f$ is the 1/e width of the optical fiber. We finally add the corresponding probability distributions $|\Psi'_W(\mathbf{p_s}, \mathbf{r_i} = \mathbf{r'_i})|^2$ together, weighted by the optical fiber function $\phi(\mathbf{r'_i})$. See MATLAB code in the appendix A.

In Fig. 2.4, we depict two intermediate steps in the calculation of the visibility and the predictability: the result of the computation of $P'_T(\mathbf{p_s}|\phi_i)$ and $P'_B(\mathbf{p_s}|\phi_i)$. The integrals of these quantities over $p_{s,y}$ give the marginal distribution $M_T(p_{s,x})$ and $M_B(p_{s,x})$, respectively, which are directly used in the calculation of the visibility and the predictability.

### 2.5.2 Impact of the $HG_{01}$ pump mode

In their original paper [7], Menzel *et al.* make a case that their choice of an $HG_{01}$ pump mode had a special role in the apparent violation of the duality principle. We thus study the impact of replacing our Gaussian pump mode by an $HG_{01}$ pump mode in our thought experiment. We find that there is a significant change in the average visibility and average predictability and that the duality relations remain satisfied.

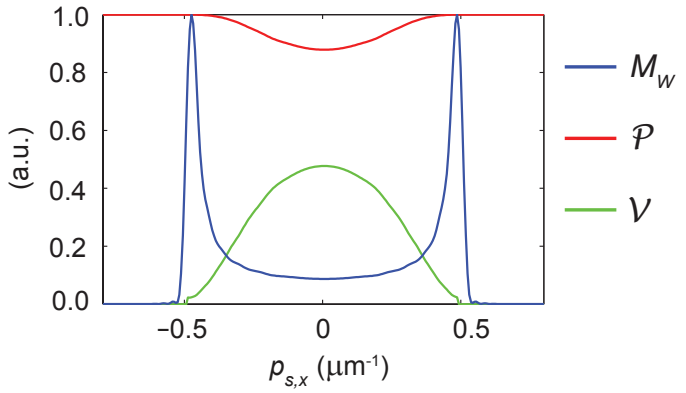


Figure 2.6: (blue) Marginal probability distribution of the signal photon, (red) predictability and (green) visibility as a function of the degree of freedom of the environment for an $\mathrm{HG}_{01}$ pump mode. Although the visibility is generally lower than for a gaussian pump mode, the predictability is higher.

The pump term in Eq. 2.3.2 becomes

$$E(r_x, r_y) = N\, r_y \exp\left(\frac{-(r_y^2 + r_x^2)}{8w_0^2}\right), \tag{2.5.1}$$

such that $E(2\mathbf{r})$ accurately describes the pump mode with $w_0$ as the 1/e width. To account for a small experimental misalignment, we also sightly change the position of the optical fiber by an amount $\delta$: $\phi(\mathbf{r_i}) = \exp[-(r_{i,x}^2 + (r_{i,y} - d/2 + \delta)^2)/(2w_f^2)]$. We chose the same set of parameters as above, for the Gaussian pump beam, except for $\{w_0 = 35\ \mu\mathrm{m},\ \delta = 7\ \mu\mathrm{m}\}$. By choosing a non-zero $\delta$, we also allow for a stronger apparent violation in the case of an $\mathrm{HG}_{01}$ pump mode.

The two-dimensional conditional far-field distribution of the signal photons is illustrated in Fig. 2.5. Also, the marginal probability distribution for the signal photon along $p_{s,x}$, the predictability and the visibility are shown in Fig. 2.6. We obtain the following results: $\{\langle\mathcal{P}\rangle = 0.974,\ \langle\mathcal{V}\rangle = 0.1538,\ \mathcal{V}_{\max} = 0.477,\ \sigma_{\mathcal{P}}^2 = 0.0015,\ \sigma_{\mathcal{V}}^2 = 0.0253\}$. The biased sampling relation amounts to $\mathcal{B} = 1.176$, which still appears to be a violation of our duality relation, but Eq. 2.2.3 is in fact satisfied with an $\mathrm{HG}_{01}$ pump mode. The main change from the case of a Gaussian pump beam is that the which-slit information is now close to unity, but at the expense of a correspondingly low average visibility. The reason for this difference is explained by the intensity dip in the middle of the $\mathrm{HG}_{01}$ pump mode, which help us predict

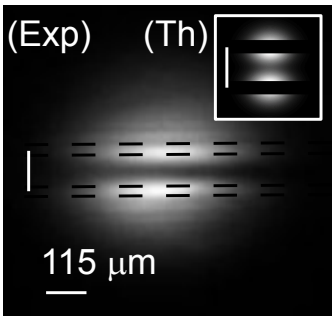


Figure 2.7: (Exp) Experimentally recorded and (Th) theoretically obtained distribution of the singles in the near-field of the two-slit mask. In the experiment, a microscope cover slip induces a $\pi$-jump in the middle of the pump beam, creating an $HG_{01}$-like mode. We simply chose an $HG_{01}$ pump mode in our model. The real slit separation is 345±50 $\mu$m and the magnification from the plane of the crystal to that of the camera is 3.0±0.5, but the scale is shown for a unit magnification for both the experiment and the theory.

which slit the signal photon traverses. To gain intuition about this effect, we can picture the two-slit mask at its exit facet with conceptual back-projection. In the ray picture, the signal and idler photons are generated at the very same position inside the crystal in 3-dimensional space and with exactly opposite momentum. Because of the momentum anti-correlations, the only way that the two photons of a given pair can pass through opposite slits is when they are born around $r_y = 0$. However, there is no light in this region of the $HG_{01}$ mode. This intuitively explains the increase in predictability and the corresponding decrease in visibility.

### 2.5.3 An experimental confirmation

In addition to the conditional behavior of the signal photon, our theory can predict the unconditioned behavior of the signal photon, that is the singles in SPDC light. The singles can easily be obtained from Eq. 2.3.3 and 2.3.4 with $w_f \to \infty$. If the optical fiber that collects the idler photon is wide enough to cover all space, the conditional probability distributions of the signal photon, $P_W(\mathbf{r_s}|\phi)$ and $P'_W(\mathbf{p_s}|\phi)$ with $w_f \to \infty$, become identical to that of the singles.

Since it is very easy to measure the singles in the laboratory, we experimentally record the their two-dimensional profile in the near-field and the far-field of a two-slit mask with an EMCCD camera and compare the result with theory as a test for the

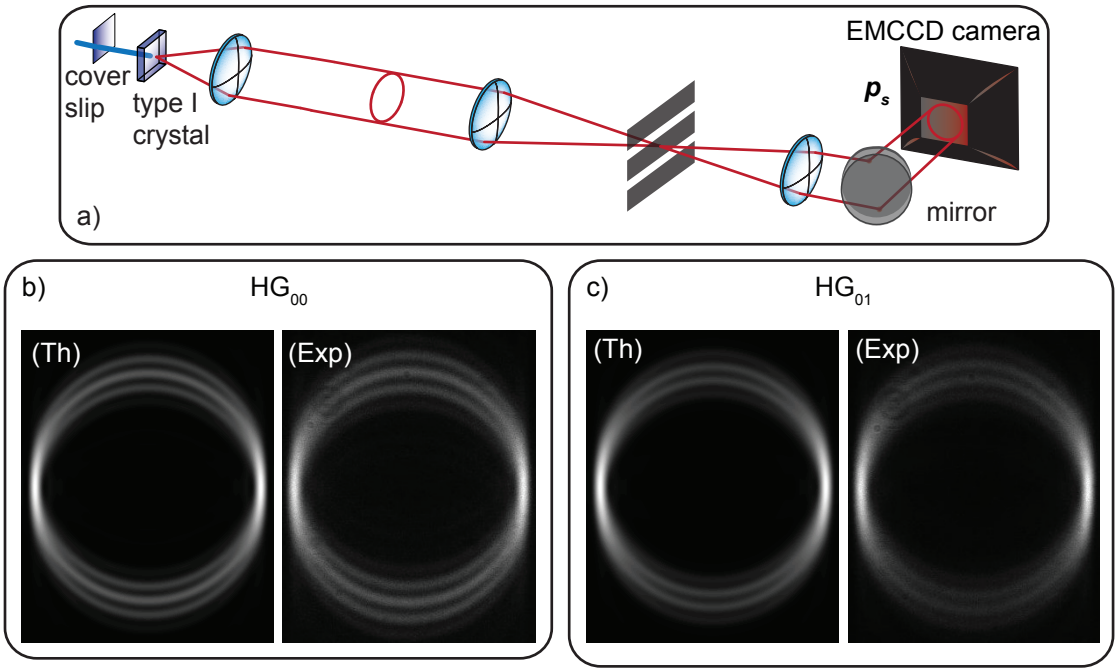


Figure 2.8: a) Experimental setup that we use to record images of the single counts. We insert a microscope cover slip in half of the pump beam in order to control the phase difference between each half. The plane of the crystal is imaged to a two-slit mask with a magnification of 3. In the configuration shown here, an EMCCD camera is located in the far-field of the mask, but we also record the near-field by adding a second lens (not shown) between the mask and the camera. We control the bandwidth of the SPDC light with a 10-nm interference filter (not shown). Shown are the experimentally recorded (Exp) and (Th) theoretically modelled distribution of the singles in the far-field of the two-slit mask for an b) $HG_{00}$ and c) $HG_{01}$ pump mode. For the latter, we observe the characteristic intensity dip in the middle of each interference pattern, on the top and the bottom. In other words, the number of bright fringes goes from being odd to even when the pump mode changes from $HG_{00}$ to $HG_{01}$.

validity of our model. Our experimental setup is depicted in Fig. 2.8 a). We can transform the input Gaussian pump mode into an $HG_{01}$-like mode with a microscope cover slip that we insert in half of the beam, see Fig. 2.7. If the cover slip produces a phase shift of $\beta 2\pi$, where $\beta$ is an integer, the input mode is effectively unchanged. The cover slip turns the input mode into the $HG_{01}$-like mode by producing a phase shift of $(2\beta+1)\pi$ in half of the beam. The input parameters in our model are $\{\varphi = -19,\ L = 3\text{ mm}, d = 115\ \mu\text{m},\ \Delta = d/3\ \mu\text{m},\ n = 1.65,\ \lambda_p = 355\text{ nm},\ w_0 = 70\ \mu\text{m},\ \delta = 0\}$. The experimental results are in excellent agreement with the theoretical predictions, see Fig. 2.8 b) and c). As mentioned above, the intensity dip in the center of the $HG_{01}$ mode causes the position correlations to be very high and the visibility of the interference pattern to drop. We even see this effect in visibility of the the singles, which is lower for the $HG_{01}$ pump mode. We attribute the slight difference between the frequency of the fringes in the theory and the experiment to the experimental uncertainty on the magnification of the optical system.

# Chapter 3

# Weak-value-assisted tomography

**This chapter is based on the following paper:**

1. J. Z. Salvail, M. Agnew, A. S. Johnson, **E. Bolduc**, J. Leach, and R. W. Boyd, "Full characterization of polarization states of light via direct measurement," *Nature Photonics*, vol. 7, pp. 316–321

## 3.1 Introduction to standard quantum state tomography

In the process of standard quantum state tomography, one performs an informationally complete set of projective measurements on an ensemble of identical quantum states in order to retrieve their density matrix. This process is crucial when one wants to determine a quantum state without prior information. Here, we show the relation between an informationally complete set of measurement outcomes and the density matrix of a discrete quantum state of finite dimension. Retrieving the density matrix from the measurement outcomes amounts to a simple linear algebra problem. The theory presented in this introduction is already known; see the work of A. J. Scott for instance [26]. In order to write the state reconstruction in a simple formula, we use a formalism that might be new to the reader.

The density matrix of a $D$-dimensional state is completely specified by $D^2$ parameters, which also corresponds to the minimum number of projective measurements required to determine a density matrix unambiguously. Instead of writing a projector on the state $|A\rangle$ in its usual matrix form, $\hat{A} = |A\rangle\langle A|$, it is more convenient

in the context of standard tomography to write it as a $D^2$-dimensional line-vector, $(\hat{A}| = \langle A| \otimes \langle A|$, where $\otimes$ is the Knonecker product. In this notation, the line-vector $(i|$ has a dimension of $D^2$ and is filled with zeros except at the $i^{\text{th}}$ position, where the value is unity. The transpose of the line-vector $(i|$ is the column-vector $|i)$. We can build a $D^2$-dimensional matrix $\mathcal{S}$ with a set of $D^2$ projectors $\{A_i\}$ stacked on top of each other:

$$\mathcal{S} = \sum_{i=1}^{D^2} |i)(\hat{A}_i|. \tag{3.1.1}$$

Each line of this $D^2$ by $D^2$ matrix indeed corresponds to a projector. The conventional and general form of the density matrix is $\rho = \sum_{i=1}^{D} p_i |\psi_i\rangle\langle\psi_i|$, where $p_i$ is the probability of finding state $|\psi_i\rangle$. The density matrix is a statistical mixture of the pure states $\{\psi_i\}$. Instead of using the conventional form and without loss of generality, we write the density matrix in a single column[1], a notation compatible with the matrix $\mathcal{S}$,

$$|\rho) = \sum_{i=1}^{D} p_i |\psi_i\rangle \otimes |\psi_i\rangle. \tag{3.1.2}$$

After performing all the projective measurements, the outcomes are then stacked in a vector $|\mathcal{M})$ to satisfy the linear relation $\mathcal{S}|\rho) = |\mathcal{M})$. Finally, the density matrix is retrieved through inversion of the matrix of projectors:

$$|\rho) = \mathcal{S}^{-1}|\mathcal{M}). \tag{3.1.3}$$

The condition for the inverse matrix $\mathcal{S}^{-1}$ to exist is that all of its projectors must be linearly independent. Eq. 3.1.3 shows that the minimum number of measurements required to retrieve the density matrix is indeed $D^2$ when we make no assumption about its form. If inferior to $D^2$, the number of equations is lower than the number unknowns in the density matrix, and the linear algebra problem is underdetermined.

Although its result is theoretically exact, one drawback of this method is that the matrix found with Eq. 3.1.3 is not necessarily a physical density matrix because of the experimental errors on the outcomes. There is no restriction yet to the form of the result. In order to find a result which lies in the space of density matrices, one

[1]It then becomes the density *vector* of dimension $D^2$, but we keep referring to it as the density matrix.

must perform a search for the density matrix which has the maximum likelihood of producing the measured outcomes. This post-measurement processing can be computationally intensive for a very high-dimensional density matrix and can even render the task impossible.

## 3.2 Accuracy of weak-value-assisted tomography

It was shown by Lundeen *et al.* that so-called weak values can be used to perform quantum state tomography [9]. The exact form of the weak value is accessible for an infinitely weak coupling strength between the system to be measured and the pointer used to measure it, but in the realistic scenario where this is not the case, only an approximation to the weak value can be retrieved experimentally. Here, we theoretically study the accuracy of the tomographic procedure of a two-dimensional state with weak measurements. This work relates to publication 2, where a polarization qubit was experimentally coupled to two positions in space.

The direct result of the weak-coupling tomographic method introduced in [9] is a physical state vector. It makes the assumption that the state under study is pure, but it requires no matrix inversion and no post-measurement processing. In high Hilbert space dimensions, the absence of post-processing can save a significant amount of time. The directness and the time-efficient nature of the weak-coupling tomographic method makes it attractive for quantum state determination in photonics, in which the pure-state assumption is often valid. The drawback of this technique, however, lies in the inherent uncertainty on the retrieved quantum state. With the standard procedure, the weak value cannot be measured with infinite precision even in the ideal case of a noiseless experimental apparatus.

In this work, we quantify the accuracy of the weak-coupling tomographic method applied to a two-dimensional state. In order to achieve this, we show the exact relation between weak values and the coefficients of the state vector. We then derive the exact outcome of a standard weak measurement, which gives an approximation to the weak value. From the outcome of the weak measurements, we construct the two-dimensional state that would be the result of an experimental procedure, and compare it with the actual initial state by calculating their fidelity.

### 3.2.1 Relation Between Weak Values and the State-Vector

We perform a theoretical tomographic procedure on the two-dimensional state

$$|\Psi\rangle = \cos\alpha\, \mathrm{e}^{i\varphi}|1\rangle + \sin\alpha|2\rangle, \tag{3.2.1}$$

where the real parameters $\alpha$ and $\varphi$ determine the complex coefficients of the eigenstates $|1\rangle$ and $|2\rangle$. We shall refer to the quantum state under study, $|\Psi\rangle$, as the *main* system. As it is not always possible to directly perform a measurement on the main degree of freedom, the standard procedure is to couple it to the spatial degree of freedom[2]. After an interaction and a measurement, the spatial degree of freedom *points* towards a particular outcome or eigenvalue. We thus call the state of the spatial degree of freedom the *pointer*. When strongly coupled to position, the eigenstates are sent to very different positions, such that they are very well resolved. In the weak coupling regime however, there is an important overlap between the pointers of each eigenstates. Upon projection of the main system into a final post-selected state, the pointer behaves in a peculiar way. In order to describe the behavior of the this post-selected state, Aharonov, Albert and Vaidman introduced the weak value of an operator $A$ [27]:

$$\langle A\rangle_W = \frac{\langle f|A|\Psi\rangle}{\langle f|\Psi\rangle}. \tag{3.2.2}$$

where $|f\rangle$ is a final post-selected state.

Before showing how to measure a weak value, let us make the link between weak values and tomography. Let $A_1$ and $A_2$ be the eigenstate observables $|1\rangle\langle 1|$ and $|2\rangle\langle 2|$ and the final state be a superposition state, namely $|f\rangle = (|1\rangle + \mathrm{e}^{i\gamma}|2\rangle)/\sqrt{2}$, where $\gamma$ is an arbitrary phase, which we set to $\gamma = 0$. From the initial state 3.2.1, the weak values of $A_1$ and $A_2$ are respectively given by

$$\begin{aligned} \langle A_1\rangle_W &= \nu^{-1}\cos\alpha\, \mathrm{e}^{i\varphi} \quad \text{and} \\ \langle A_2\rangle_W &= \nu^{-1}\sin\alpha, \end{aligned} \tag{3.2.3}$$

where $\nu = \mathrm{e}^{i\varphi}\cos\alpha + \sin\alpha$. The pure two-dimensional quantum state can be written

[2]For example, a polarizing beam-splitter is used to separate the polarization eigenstates.

in terms of the above weak values [9]:

$$|\Psi\rangle = \nu\langle A_1\rangle_W|1\rangle + \nu\langle A_2\rangle_W|2\rangle, \tag{3.2.4}$$

Since $\nu$ has the role of a normalizing constant, its measurement is not required in the tomographic process. Because of the identity $\langle A_1\rangle_W+\langle A_2\rangle_W = 1$ [2], the measurement of a single weak value suffices to construct the state vector. Eq. 3.2.4 is exact, but a weak value cannot be retrieved exactly in a realistic scenario, where the coupling is never infinitely weak. The accuracy on the measurements of the weak values has a direct impact on the precision of the retrieved state from Eq. 3.2.4.

### 3.2.2 Exact model of weak-coupling measurements

In order to show the accuracy of the tomographic procedure, we model every step of the weak value measurement exactly. Firstly, let us weakly couple the eigenstates of the main system, $|1\rangle$ and $|2\rangle$, to different positions in space, such that they can be partially resolved. Consider an initial one-dimensional Gaussian pointer state centered on $x = 0$:

$$\phi(x) = \frac{1}{(\sigma^2\pi)^{1/4}} \exp\left(\frac{-x^2}{2\sigma^2}\right), \tag{3.2.5}$$

where $\sigma$ is the 1/e width of the pointer. Upon an arbitrary interaction which need not be specified in details, eigenstates 1 and 2 translate from average position $x = 0$ to average positions $x = d$ and $x = -d$, respectively. The composite state of the main system and the pointer is given by $|\Psi'\rangle = W\cos\alpha\, e^{i\varphi}|1\rangle|\phi(x-d)\rangle + W\sin\alpha\,|2\rangle|\phi(x+d)\rangle$, where $W$ is a normalization constant. The eigenstates are quasi-perfectly resolved under the condition that $d > 3\sigma$. The strength of the measurement $s$ can be quantified with the ratio of the displacement of the pointer to its width: $s = d/\sigma$. Our weak measurement procedure requires a projection of the main system onto the final state, namely $|f\rangle = (|1\rangle + |2\rangle)/\sqrt{2}$. The projection results in $|\Psi''\rangle = N\cos\alpha\, e^{i\varphi}|\phi(x-d)\rangle + N\sin\alpha\,|\phi(x+d)\rangle$, where $N$ is the new normalization constant. The coefficients of the main system are simply transferred to the pointer state. In other words, all the information about the main system is now contained in the pointer state. After the interaction and the post-selection, the expectation value of the pointer in coordinate space is given by

$$\langle\Psi''|x|\Psi''\rangle = \frac{-d\cos(2\alpha)}{1+\exp(-s^2)\cos\varphi\sin(2\alpha)}. \tag{3.2.6}$$

The main result of Aharonov, Albert and Vaidman in [27] is that the real and imaginary parts of the weak value are respectively related in a simple way to the expectation value of the post-interaction pointer in coordinate space and momentum space. In our case, the relations are

$$\begin{aligned} \Re[\langle A_1\rangle_W] &\approx \frac{d+\langle x\rangle}{2d}, \qquad & \Im[\langle A\rangle_1] &\approx \frac{-\sigma^2\langle k\rangle}{2d}, \\ \Re[\langle A_2\rangle_W] &\approx \frac{d-\langle x\rangle}{2d}, \qquad & \Im[\langle A\rangle_2] &\approx \frac{\sigma^2\langle k\rangle}{2d}, \end{aligned} \tag{3.2.7}$$

where $k$ is the wavenumber of the pointer. The parameters $d$ and $\sigma$ both have to be measured to retrieve the weak values. We don't show the lengthy derivation of the above relations, but a very similar derivation can be found in [27].

To read the imaginary part of the weak values, we need to express the post-interaction state in momentum space. After a Fourier transform, we find $|\Psi'''\rangle = N\cos\alpha\,\mathrm{e}^{i\varphi}|\Phi(k)\rangle + N\sin\alpha\,|\Phi(-k)\rangle$, with $\Phi(k) = (\sigma^2/\pi)^{1/4}\exp\left(-k^2\sigma^2/2\right)\exp(ikd)$. The expectation value of the post-interaction pointer state in momentum space is given by

$$\langle\Psi'''|k|\Psi'''\rangle = \frac{1}{\sigma^2}\frac{d\exp(-s^2)\sin(2\alpha)\sin\varphi}{1+\exp\left(-s^2\right)\cos\varphi\sin(2\alpha)}. \tag{3.2.8}$$

The table is now set to construct the initial state (Eq. 3.2.4) with the exact outcomes of the weak measurements (Eq. 3.2.7). After a lengthy but straightforward calculation, we find that the constructed state $|\Psi_c\rangle$ is given by

$$\begin{aligned} |\Psi_c\rangle &= D_1\cos\alpha\,\mathrm{e}^{i\varphi}|1\rangle + D_2\sin\alpha\,|2\rangle, \quad \text{with} \\ D_1 &= \left(\cos\alpha\,\mathrm{e}^{i\varphi} + \mathrm{e}^{-s^2}\sin\alpha\right)/\sqrt{M} \quad \text{and} \\ D_2 &= \left(\cos\alpha\,\mathrm{e}^{i\varphi}\,\mathrm{e}^{-s^2} + \sin\alpha\right)/\sqrt{M}, \end{aligned} \tag{3.2.9}$$

where $M = \cos^4\alpha + \sin^4\alpha + 2^{-1}\sin^2(2\alpha)\,\mathrm{e}^{-2s^2} + \sin(2\alpha)\cos\varphi\,\mathrm{e}^{-s^2}$. In the limit of strong measurements, $s\to\infty$, the constructed state takes the form $|\Psi_c^{\text{strong}}\rangle = \cos^2\alpha|1\rangle + \sin^2\alpha|2\rangle$. The phase information is completely lost, and the real amplitudes are squared. In this case, the measured state does not represent the main system well unless the latter is one of the two eigenstates.

### 3.2.3 Average fidelity between the initial state and the measured state

We quantify the general accuracy of the method as a function of the weakness of the measurements with the fidelity between the constructed state and the initial state: $F(s) = |\langle\Psi_c|\Psi\rangle|$. We let the parameters $\alpha$ and $\varphi$ have any value between $-\pi$ and $\pi$, such that all possible initial states are covered with equal probability. The average fidelity is then

$$\langle F(s)\rangle = \frac{1}{\pi^2}\int_{-\frac{\pi}{2}}^{\frac{\pi}{2}}\int_{-\frac{\pi}{2}}^{\frac{\pi}{2}} d\alpha\, d\varphi\, |\langle\Psi_c|\Psi\rangle|. \tag{3.2.10}$$

A graph of Eq. 3.2.10 as a function of the strength of the measurements is shown in Fig. 3.1. The above integral does not have a known analytical solution. We thus perform it numerically by breaking the continuous variables into $n$ discrete points. Here we study the specific case of a two-dimensional state, but one could generalize the integrals to higher dimensions. In $D$ dimensions, the number of parameters required to specify a state-vector is $2D-2$. The total number of discrete points in the numerical calculation then scales exponentially with dimension: $n^{2D-2}$, and the integral quickly becomes impossible to solve. One can however highly reduce the number of points by assuming that the fidelity is unity for states which satisfy the condition $\langle f|\Psi\rangle > \delta$, where $\delta$ is small enough to ensure that the relations 3.2.7 are nearly exact. As a consequence, the integrals must only be numerically performed in the small region satisfying $\langle f|\Psi\rangle \leq \delta$.

For future use, it might be more convenient to manipulate an analytical formula rather than the numerically solving Eq. 3.2.10. We thus fit the result to an exponential function of the form $a + (1-a)\exp(-(s/b)^c)$, where the optimal values of the parameters are $\{a = 0.873,\ b = 1.14,\ c = 2.46\}$. Fig. 3.1 shows a plot of the average fidelity as a function of the strength of the measurements and the exponential fit. The first parameter $a$ is determined by the saturation value of the fidelity in the strong coupling regime. The other parameters, $b$ and $c$, are determined by the width and the steepness of the exponential curve, respectively.

The tomographic procedure yields accurate results in the very weak coupling regime. Notably, for $s \leq 1/4$, the fidelity is above 0.998. However, in this weak coupling regime, there is an important experimental disadvantage. When the initial state is nearly orthogonal to the final state, $\langle f|\Psi\rangle \approx 0$, the post-interaction state and

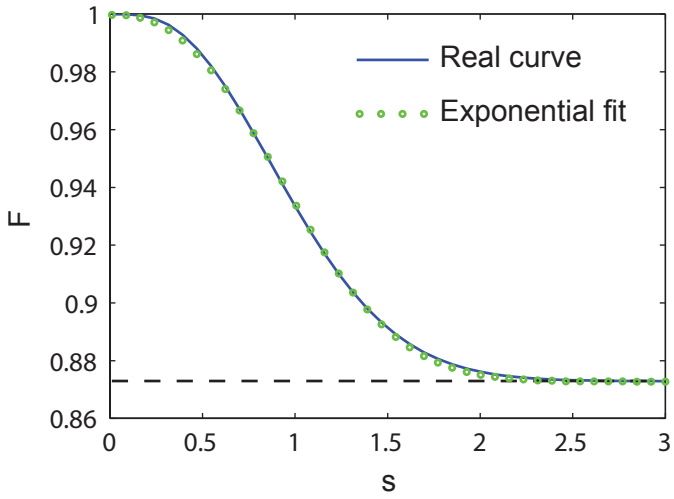


Figure 3.1: Fidelity between the initial state $|\Psi\rangle$ and the measured state $|\Psi_m\rangle$ through the tomographic process with weak values as function of the strength of the measurement. For a measurement strength of $s = 2$, the distance between the eigenvalues of $|1\rangle$ and $|2\rangle$ (2d) is equal to the 1/e width of the initial pointer. In this strong measurement regime, the eigenvalues are distinguishable, and the phase information is lost.

the final state are also nearly orthogonal, and the probability of detection is extremely low: $|\langle f|\Psi'\rangle|^2 \approx 0$. When the detection probability reaches the level of the noise in the system, the accuracy on the measured values of $\langle x\rangle$ and $\langle k\rangle$ is strongly affected. This effect is not taken into account in the current analysis, but it is important to consider it in the design of an experiment. Stronger coupling regimes do not suffer from low detection probability, which make their experimental implementation easier to achieve.

In the regime of moderate coupling, for $1/4 < s < 2$, the measured state does not generally correspond to the actual state under study. It is possible, however, to construct the actual state with arbitrary accuracy from the imperfect measurements of the weak values. The approximation in the simple relations Eq. 3.2.7 break down when the main system and the post-selected states are about orthogonal, i.e. when $\langle f|\Psi\rangle \approx 0$. We can avoid this break down by choosing a different superposition for the post-selected state. For instance, we could chose $|f'\rangle = (|1\rangle - |2\rangle)/\sqrt{2}$ upon realization that $|f\rangle = (|1\rangle + |2\rangle)/\sqrt{2}$ is too close to being orthogonal to the main system, which realization is made through observation of the low probability associated with near-orthogonal projection. Changing the post-selected state is not necessarily the best

solution since it requires reconfiguration of the experimental setup. Instead, we can find the parameters of the main system, $\alpha$ and $\varphi$, from the outcomes of the expectation values, $\langle x \rangle$ and $\langle k \rangle$. Recall that the displacement $d$ and the width of the initial pointer state $\sigma$ are measured properties of the experiment. We thus have two independent equations, Eq. 3.2.6 and 3.2.8, and two unknowns. The outcomes of the measurements form an informationally complete set, and identify the initial state unambiguously. To find the exact values of $\alpha$ and $\varphi$, we can solve the equations for these parameters. In doing so, we lose the directness of Eq. 3.2.4, but we retrieve the wave vector exactly.

### 3.2.4 Conclusions

In conclusion, we have calculated the average fidelity between an arbitrary two-dimensional quantum state and the state retrieved through a weak-value-assisted tomographic procedure. We modelled an interaction which couples with arbitrary strength the two-dimensional state to positions in space. The initial gaussian pointer had a 1/e width of $\sigma$, and after interaction, the pointer was shifted by an amount $d$ for one eigenstate and $-d$ for the other. The strength of the measurement was quantified as $s = d/\sigma$. In the very weak coupling regime, namely $s < 1/4$, the average fidelity was higher than 0.998, while in the strong coupling regime ($s \geq 2$), the average fidelity saturated to the value of 0.873. Our analysis could be generalized to D-dimensional systems.

In the following publication, we describe an experiment where we use weak-value-assisted tomography to experimentally retrieve polarization states of light. We directly determine the coefficients of a two-dimensional pure state with the technique developed by Lundeen *et al.* (2011) [9]. We also measure the elements of the Dirac distribution, which is informationally equivalent to the density matrix, with the method of Lundeen *et al.* (2012) [10]. Our experimental setup is based on that of Ritchie *et al.* [28], who performed the first experimental realization of a measurement of a weak value. Their pointer displacement was $d = 0.32$ $\mu$m and the 1/e width of the pointer was $\sigma = 39$ $\mu$m. The strength of the coupling was thus less than 0.01, allowing high accuracy for a tomographic procedure even though they were not necessarily aware of the possibility.

nature photonics

ARTICLES

PUBLISHED ONLINE: 3 MARCH 2013 | DOI: 10.1038/NPHOTON.2013.24

# Full characterization of polarization states of light via direct measurement

Jeff Z. Salvail[1]*, Megan Agnew[1], Allan S. Johnson[1], Eliot Bolduc[1], Jonathan Leach[1] and Robert W. Boyd[1,2]

**Ascertaining the physical state of a system is vital in order to understand and predict its behaviour. However, due to their fragile nature, the direct observation of quantum states has, until recently, been elusive. Historically, determination of the quantum state has been performed indirectly through the use of tomography. We report on two experiments showing that an alternative approach can be used to determine the polarization quantum state in a simple, fast and general manner. The first experiment entails the direct measurement of the probability amplitudes describing pure polarization states of light, the first such measurement on a two-level system. The second experiment entails the direct measurement of the Dirac distribution (a phase-space quasi-probability distribution informationally equivalent to the density matrix), demonstrating that the direct measurement procedure is applicable to general (that is, potentially mixed) quantum states. Our work has applications to measurements in foundational quantum mechanics, quantum information and quantum metrology.**

Measurement plays a vital role in the practice of science. This is especially so in the case of quantum mechanics, where the measurement process is fundamental to the formulation of the theory. A crucial feature of quantum mechanics is that a measurement of one variable of a system erases information about the corresponding conjugate variable. The classic example is that determining the position of a particle disturbs its momentum, and vice versa. These measurements, known as strong measurements, collapse the wavefunction such that no additional information can be obtained.

To completely determine a quantum state, which is described in general by complex numbers, one must perform multiple measurements on many identical copies of the system. Quantum tomography[1] is one method of quantum state determination that uses strong measurements[2–6]. Tomographic reconstruction entails estimating the complex numbers that describe the state from the real-valued probabilities that result from strong measurements. Consequently, this approach can be considered indirect state determination due to the requirement for post-processing.

The first demonstration of direct quantum wavefunction measurement was reported recently[7]. In this study, the transverse spatial wavefunction, that is, the probability amplitude for photon detection at each position, was measured directly. In contrast to tomography, this method is considered direct because the measurement apparatus records the complex probability amplitudes describing the state, so there is no need for post-processing. The technique for direct quantum state determination is applicable to many different systems, which, as the authors of ref. 7 point out, includes the polarization degree of freedom. Recently it has been proposed that this technique can be generalized to measure all aspects of a general quantum state, that is, so that it is compatible with mixed states[8].

Although familiar and convenient, the density matrix is not the only way to describe a general quantum state. A state can be expressed in terms of its Dirac quasi-probability distribution (or phase-space representative), which is informationally equivalent to the density matrix $\rho$ (refs 8–11). Quasi-probability distributions have been studied theoretically, in the context of discrete systems[12,13], and measured directly, for the case of the spatial Wigner function[14,15]. The Dirac distribution is particularly useful because of its relation to the direct measurement technique[8].

Directly measuring a quantum system relies on the technique of weak measurement: extracting so little information from a single measurement that the state does not collapse[16–30]. The first measurement of a weak value was the amplified transverse displacement between the polarization components of light induced by a birefringent crystal[19]. More recently, the technique has been used to observe the transverse displacement of a beam of light by only several ångstroms[25] and an angular rotation on the order of femtoradians[26]. Weak measurement was recently proposed as a tool to study nonlinear optical phenomena with single photons by amplifying the apparent photon number[29]. Weak measurements have also allowed observation of apparent super-luminal velocity[21] and the mapping of average photon trajectories after they pass through a double slit[28].

The main results of our Article are the direct measurements of the wavefunction and Dirac distributions for polarization states of light. These results are the first direct measurements that are applicable to qubits—the fundamental unit of quantum information. We demonstrate direct state measurement in a two-dimensional Hilbert space by weakly coupling the polarization state of light to the spatial degree of freedom. This study extends previous work on polarization weak measurements[17,19,24]. We obtain the weak value by introducing a small spatial shift between the horizontal and vertical polarization components, then strongly measuring the polarization in the diagonal/antidiagonal basis. Importantly, our experimental implementation determines the general description of the state, and, in contrast with previous experimental work, it is not limited to pure states.

In our experimental procedure, we use direct measurement to determine the polarization state of the photons in an intense beam of light that has been prepared such that each photon is in the same quantum polarization state. Thus, even though the light beam is intense, our procedure determines the quantum

[1]Department of Physics, University of Ottawa, Ottawa, Canada K1N 6N5, [2]Institute of Optics, University of Rochester, Rochester, New York 14627, USA.
*e-mail: jeff.salvail@gmail.com

polarization state of each photon. We note that the technique outlined in this Article could be used for single-photon states, although the detection process would need to be altered accordingly. The basic procedure outlined in this Article could still be used in this situation, although the detection process would need to be performed using single-photon detectors. In this regard, we note that recent work has shown that cooled[28] or commercial electron-multiplying[31] charge-coupled device (CCD) cameras can be operated at the single-photon level with sufficient sensitivity to determine quantum features of the light field.

## Theory

In any quantum measurement, the observer couples an unknown probe state to a pointer that reads out the value. For example, a birefringent crystal can couple the polarization state of light to the spatial degree of freedom; in this case, the initial polarization state is called the probe state, and the spatial degree of freedom of the light is considered the pointer. If the pointer state is a Gaussian mode with width $w$, a strong measurement separates the eigenstates of the measurement operator $\hat{A}$ by an amount $\delta \gg w$, such that the eigenstates are completely resolved.

Weak measurements occur in the opposite regime, where the coupling is much less than the pointer width, $\delta \ll w$. In this case, the eigenstates of $\hat{A}$ are not resolved by the pointer, so the wavefunction does not collapse. Therefore, a subsequent measurement performed on the quantum state can be used to extract further information. If the subsequent measurement is strong, such that the eigenstates are resolved, we can choose to consider only the statistics of one particular outcome; this is called post-selection and the chosen outcome of interest is the post-selected state. The average result of the weak measurement is called the weak value and is given by

$$\langle \hat{A} \rangle_{\phi}^{W} = \frac{\langle \phi | \hat{A} \rho | \phi \rangle}{\langle \phi | \rho | \phi \rangle} \tag{1}$$

where $\rho$ is the density operator that describes the initial state and $|\phi\rangle$ is the final, post-selected, state[20,23]. In the case where the initial state is pure and may be described by the state vector $|\psi\rangle$ (that is, $\rho = |\psi\rangle\langle\psi|$), the weak value in equation (1) simplifies to the form first introduced by Aharonov, Albert and Vaidman[16]:

$$\langle \hat{A} \rangle_{\phi}^{W} = \frac{\langle \phi | \hat{A} | \psi \rangle}{\langle \phi | \psi \rangle} \tag{2}$$

In the case where $|\psi\rangle = |\phi\rangle$, the expectation value of the weak measurement is equal to the standard expectation value of the operator $\hat{A}$. In general, the initial and final states may differ, and the weak value can be complex. For the specific case where the initial and final states are nearly orthogonal, the weak value can become arbitrarily large, leading to the amplification effect discussed above. The complex nature of the weak value, combined with the fact that weak measurement does not significantly disturb the system, enables the direct measurement of the quantum state via weak measurements.

The complex weak value is determined by characterizing the pointer. The pointer's position indicates the real part of the weak value $\mathrm{Re}[\langle \hat{A} \rangle_{\phi}^{W}]$, and the pointer's momentum indicates the imaginary part $\mathrm{Im}[\langle \hat{A} \rangle_{\phi}^{W}]$ (ref. 32).

In the specific case that the weak and final measurements are of mutually unbiased[33] variables (Supplementary Note S1), the weak values have a direct relationship to the state description. The coefficients $c_i$ of a wave vector $|\psi\rangle$ that describes a pure quantum state can be written in terms of specific weak values:

$$c_i = \langle a_i | \psi \rangle = \nu \langle \pi_{a_i} \rangle_{b_j}^{W} \tag{3}$$

Here, the weakly measured observable $\pi_{a_i} = |a_i\rangle\langle a_i|$ is the projector into the $i$th state of the basis $\mathcal{A}$ (ref. 7). The factor $\nu$ is a constant of normalization independent of $i$ and may be taken to be real. Equation (3) shows that the wavefunction describing a pure state can be directly measured by scanning weak measurements in basis $\mathcal{A}$ and post-selecting on a fixed state in the mutually unbiased basis $\mathcal{B}$, then normalizing the wavefunction.

The procedure that uses equation (3) can be extended to give a technique to directly measure the most general description of the quantum state. The simplest such generalization entails measuring weakly in basis $\mathcal{A}$, followed by recording the results of all outcomes of the strong measurement in basis $\mathcal{B}$. In terms of the density operator $\rho$, the elements of the Dirac distribution[9], which describes a general quantum state, can be written in terms of specific weak values as

$$S_{ij} = \langle b_j | a_i \rangle \langle a_i | \rho | b_j \rangle = p_{b_j} \langle \pi_{a_i} \rangle_{b_j}^{W} \tag{4}$$

That is to say, the $(i,j)$th element of the Dirac distribution is equal to the result of the weak measurement of $\pi_{a_i}$ followed by post-selection on state $b_j$, multiplied by the probability of successful post-selection $p_{b_j} = \langle b_j | \rho | b_j \rangle$ (ref. 8). Importantly, one can always invert equation (4) and calculate the density matrix $\rho$ from the measured Dirac distribution $S$. For further details on equations (3) and (4), see Supplementary Notes S2 and S3.

The Dirac distribution is an underused but elegant way to describe a general quantum state. In particular, it is very useful for visualizing discrete systems. In our work, we use the 'left' phase-space representative of Chaturvedi *et al.*[10] throughout, and discuss only the discrete (that is, $N$-level) Hilbert space version. The connection between Dirac distribution, joint probabilities and the weak value was also explored by Hofmann[11].

An important result is that a single weak value completely determines the wavefunction of a qubit (Supplementary Note S2). For a single photon, the weak measurement has very large uncertainty, so the above procedure must be repeated on many photons, or equivalently on a classical light beam, to establish the weak value with a high degree of confidence.

## Experiment

We performed two experiments. First, we implemented the technique encapsulated by equation (3) to measure a variety of pure polarization wavefunctions. Second, we applied the technique summarized by equation (4) to measure the Dirac distribution of a variety of states. The only difference between the two experiments is in the nature of the strong measurement: in the first experiment, a single strong measurement outcome is required, whereas in the second experiment, all eigenstates of the strong measurement are recorded.

A brief summary of the experimental procedures is now given (see Fig. 1 for a schematic). The probe (polarization) and pointer (spatial mode) states were first prepared (Fig. 1a). The weak measurement was then performed with a quartz plate, which slightly displaces the two orthogonal polarization components $|H\rangle$ and $|V\rangle$ of the probe laterally (Fig. 1b). Third, the strong measurement in the $D/A$ basis was performed (Fig. 1c). To measure the wavefunction, we post-selected the final state by projecting the polarization into the diagonal state $|D\rangle$ using a linear polarizer (LP) oriented to transmit diagonally polarized light. To measure the Dirac distribution, a calcite crystal was used to separate components $|D\rangle$ and $|A\rangle$ so that they did not overlap. Finally, the wavefunction or Dirac distribution was read out by imaging the near- and far-fields of the plane immediately after the quartz onto separate regions of interest of a CCD camera (Fig. 1d). Two regions were used to read out the wavefunction and four were needed to read out the Dirac distribution.

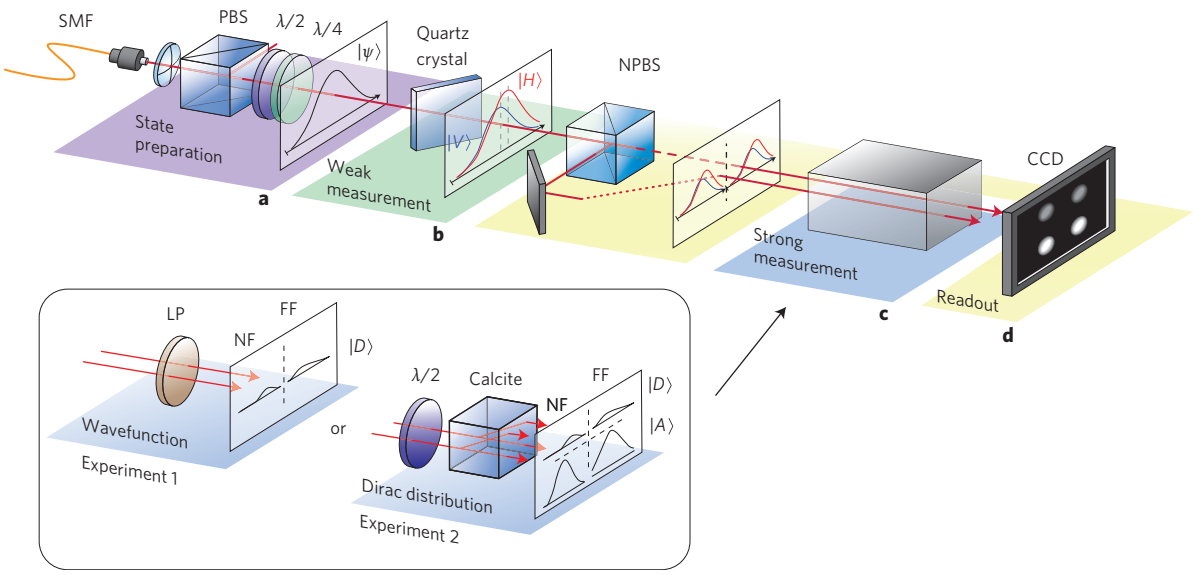


**Figure 1 | Schematic representation of the experiment. a**, The output of the single-mode fibre (SMF) is a near-Gaussian transverse mode of light. A polarizing beamsplitter (PBS) and waveplate(s) create a known pure polarization state. **b**, A quartz crystal at an oblique angle performs the weak measurement by introducing a small (compared to the beam waist) lateral displacement between horizontal and vertical polarization components. **c**, A strong measurement in a basis (diagonal/antidiagonal) mutually unbiased from the weak measurement is used to complete the direct measurement. Inset: To measure the wavefunction, a linear polarizer oriented to transmit diagonally polarized light performs the strong measurement and post-selection. To measure the Dirac distribution, a $\lambda/2$ wave-plate and calcite beam displacer carry out the strong measurement. **d**, A 50:50 non-polarizing beamsplitter (NPBS) splits the light into two sub-ensembles. These are imaged in the near-field (dotted line, NF) and far-field (dashed line, FF) of the quartz crystal onto non-overlapping regions of the CCD camera.

To demonstrate our ability to perform the direct measurement of the polarization state, we measured the probability amplitudes of three sets of input polarization states, each corresponding to a different great circle on the Poincaré sphere. The states were created by appropriate orientation of a half-wave plate and, optionally, a quarter-wave plate. In the second experiment, we created a number of states in the same fashion and measured their Dirac distributions, then calculated the associated density matrix.

## Results

Figure 2 shows the measured weak values and corresponding polarization probability amplitudes as a function of input polarization angle. Figure 3 shows the calculated Stokes parameters for each measured $|\psi\rangle$ in Fig. 2 (blue points). We also show calculated Stokes parameters for two additional paths around the Poincaré sphere. Measured weak values and probability amplitudes are included in Supplementary Figs S1 and S2 for all these states.

Figure 4 shows directly measured Dirac distributions and the corresponding density matrices of different polarization states. A variety of states were created for calibration, as in the first experiment, but here all outcomes of the strong measurement are considered.

## Discussion

Figure 2 shows that the largest divergence between theory and result in experiment 1 occurs when the initial state is antidiagonal and therefore orthogonal to the post-selected state of the diagonal. In this limit, the weak value is undefined, whereas the pointer reaches a maximum displacement (see refs 16,34). This difficulty is overcome by the full state characterization technique performed in experiment 2. Recalling equation (4), it is precisely in this regime where $p_{b_j}$ goes to zero, cancelling the effect of the breakdown of the weak-value approximation.

We note that density matrices determined by the technique demonstrated herein are not guaranteed to be precisely Hermitian due to measurement noise. For example, the density matrices shown in Fig. 4 have small imaginary components along the diagonal, with a magnitude on the order of the measurement uncertainty (~3%).

The similarity between equations (3) and (4) suggests a simple connection between the coefficients of the wavefunction and the entries of its Dirac distribution. In the case that the state is pure, we may combine the two equations to determine the real constant of proportionality that relates the two:

$$c_i = \frac{\nu}{p_{b_j}} S_{ij} \tag{5}$$

We see that there is a column $j$ of the Dirac distribution that is proportional to the wavefunction $c_i$. It is, in particular, the column corresponding to the choice of post-selection in equation (3) that renders $\nu$ independent of $i$ (and hence $\nu$ can be taken to be real).

Equation (5) has particular relevance to our experiment for the states that have a constant of normalization $\nu$ equal to unity and a probability of post-selection equal to one-half. These states lie on the great circle of the Poincaré sphere that includes $\{|H\rangle, |R\rangle, |V\rangle, |L\rangle\}$ (red points in Fig. 3, weak values and probability amplitudes in Supplementary Fig. S1). Each state on this circle is from a basis that is mutually unbiased with respect to the strong measurement $\pi_D$. For these states, we see that $c_i = 2S_{ij}$ and hence the wavefunction is twice a column of the Dirac distribution. See Fig. 4 for two examples.

The technique we demonstrate compares favourably with quantum tomography with regard to inferring the density matrix from measurement results. Tomography via maximum likelihood estimation or least-squares fitting, which is an example of an inverse problem, becomes prohibitively difficult as the dimension of the state or number of particles in a multipartite state increases. The difficulty arises from the computational requirements of varying the vast number of fit parameters needed to estimate the state[6,35]. In contrast, no fitting is required to determine the density matrix from the directly measured Dirac distribution because it is

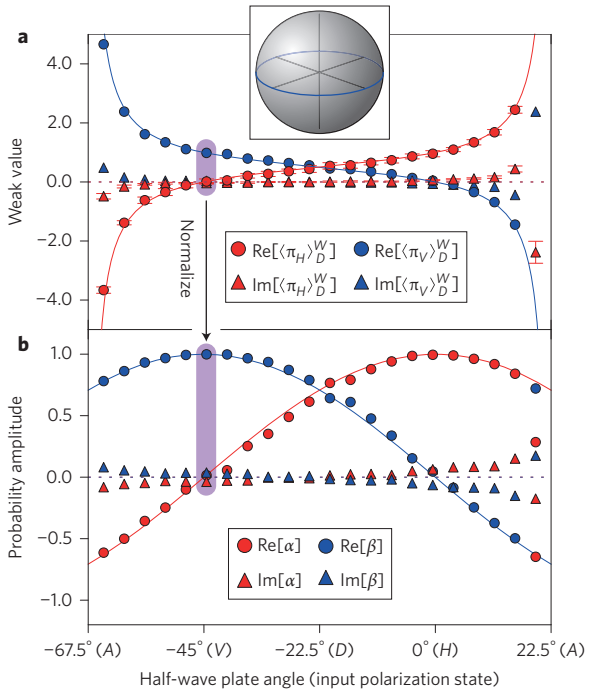


**Figure 2 | Results of experiment 1 with linearly polarized probe states.** **a**, Measured average weak values plotted as a function of input polarization angle; 0° is defined as parallel to the optical table. For clarity, error bars are shown only for the red points, and indicate the standard deviation of 100 independently measured weak values. **b**, Real and imaginary components of the probability amplitudes determined by normalizing the weak values of each test state, where $|\psi\rangle = \alpha|H\rangle + \beta|V\rangle$. For both panels, the solid lines are the theoretical predictions of the real components, and the dotted lines are the theoretical predictions of the imaginary components. Inset: a Poincaré sphere with the path taken indicated by the blue line.

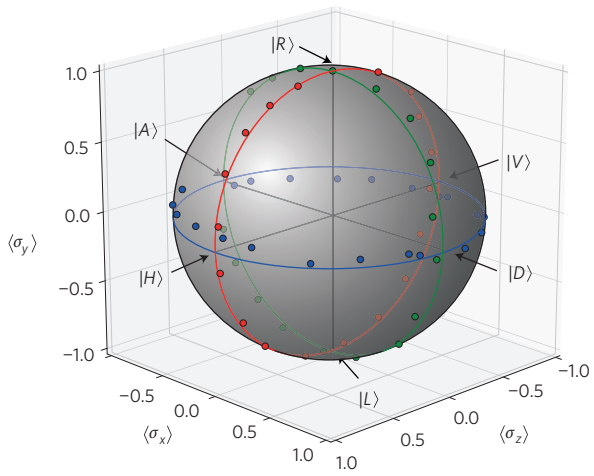


**Figure 3 | Measured states on the Poincaré sphere.** A Poincaré sphere with the set of directly measured states, indicated by their calculated Stokes parameters $\langle\sigma_x\rangle = \langle\psi|(\pi_D - \pi_A)|\psi\rangle$, $\langle\sigma_y\rangle = \langle\psi|(\pi_R - \pi_L)|\psi\rangle$, $\langle\sigma_z\rangle = \langle\psi|(\pi_H - \pi_V)|\psi\rangle$. Blue points indicate states created by rotating the half-wave plate. Red (green) points indicate calculated Stokes parameters for states created by rotating the half-wave plate, followed by a quarter-wave plate at fixed angle of 0° (45°). Solid lines indicate paths taken for each data set.

calculated analytically. Hence, we anticipate that for high-dimensional quantum systems in particular, direct measurement will become a widely used technique for quantum state determination.

The technique we present has several logical extensions, such as directly measuring polarization of single photons or multipartite states. Because, for the case of coherent states, the photon detection amplitude is analogous to the classical Maxwell field, the main difference between our experiment and the single-photon experiment is one of a technical nature. One possibility is to measure the spatial distribution of the single photons with a cooled CCD[28] or electron-multiplying CCD[31]. To measure the Dirac distribution describing polarization-entangled photons, our weak and strong measurement schemes would be duplicated for the signal and idler photons, together with a multiplexed coincident measurement scheme. The required sixteen post-selection probabilities and joint weak values[32] can be established by measuring all four combinations of position and momentum of both pointers, for each of the four

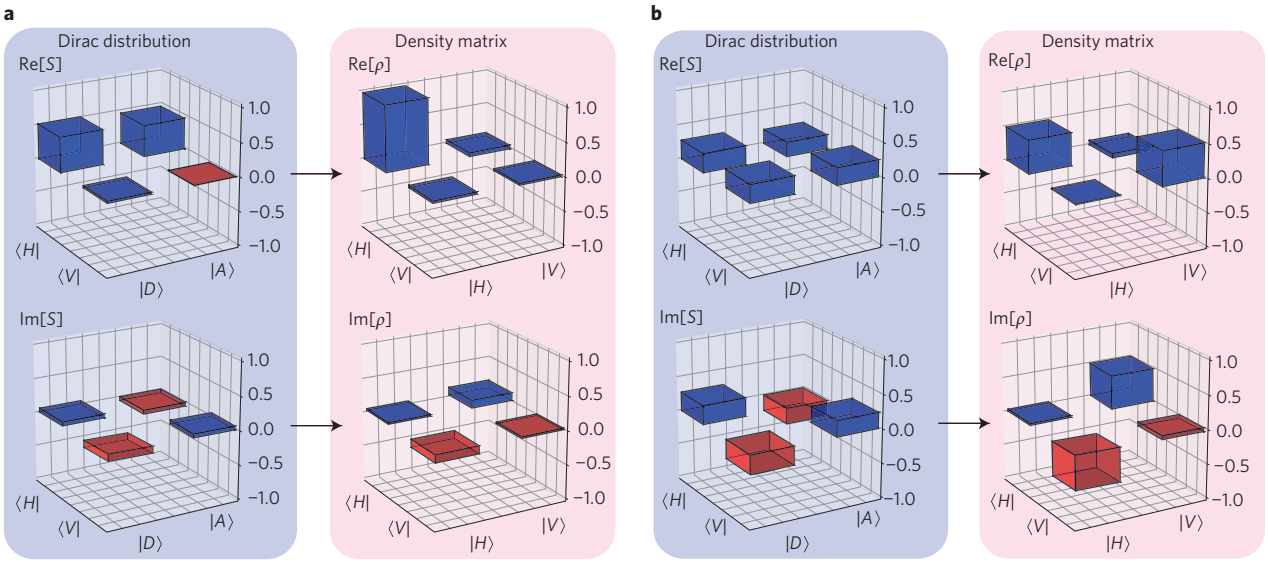


**Figure 4 | Results of experiment 2. a**,**b**, The directly measured Dirac distributions (left) and corresponding density matrices (right) for the horizontal linear polarization state $|H\rangle$ (**a**) and left-hand circular polarization state $|L\rangle = 1/2((1+i)|H\rangle + (1-i)|V\rangle)$ (**b**). The axes of the Dirac distribution are the mutually unbiased bases $H/V$ and $D/A$; the density matrix describes the state in terms of only one basis, $H/V$. Red towers indicate negative values.

post-selection outcomes. This could be achieved with presently available technology using screening slits in the appropriate planes, and triggered bucket detectors.

Direct measurement can also be extended to study other discrete systems, such as the coupled spin qubits that exist in solid-state implementations of quantum information experiments[36,37]. The entire direct measurement process can be viewed as a quantum circuit, where the weak interaction is viewed as an entangling operation between the pointer and probe (see, for example, ref. 38). This means the complex-valued description of an unknown state can be determined and used within the context of a larger quantum algorithm. Additionally, the relationship between the number of photons and the associated uncertainty of the measured state is an open question, and this is an area currently under investigation.

## Conclusion

In summary, we have performed the first direct measurements of general polarization states of light. We obtained our results through parallel measurements of the real and imaginary components of the weak value of polarization. An important result is that a single weak value, corresponding to the weak measurement of only one observable, determines both complex coefficients of the pure state of a qubit. We provide some ideas for plausible extensions to this work. Direct measurement using weak values is poised to be a very promising alternative to quantum tomography. This is especially the case in discrete high-dimensional systems or experiments where the quantum state must be recorded directly by the apparatus.

## Methods

A near-Gaussian pointer state was prepared by passing HeNe laser light through a single-mode fibre (SMF). The probe was then prepared by polarizing the light with a polarizing beamsplitter (PBS), then rotating the angle of polarization with a half-wave plate ($\lambda/2$) and/or quarter-wave plate ($\lambda/4$).

The weak measurement was performed by coupling polarization information to the spatial degree of freedom of the light. Light incident at an oblique angle on an $X$-cut quartz crystal undergoes a polarization-dependent parallel displacement. By aligning the extraordinary axis with the $x$-axis and rotating the crystal about the $y$-axis, horizontal and vertical polarizations become slightly separated in $x$. We took the $z$-axis to be the direction of propagation of the light, $x$ to be the transverse direction parallel to the optical table, and $y$ to be the transverse direction perpendicular to the table. The angle of incidence was adjusted to $\sim 40^\circ$ to ensure the two optical paths through the crystal were equal, mod $2\pi$, through the ordinary and extraordinary axes (based on a crystal thickness of 700 μm).

It is important that the pointer state be a Gaussian with a flat phase-front. We collected the SMF output with a microscope objective (×10) and focused the light onto the quartz crystal (~45 cm away). This ensured that the phase-front was approximately flat over the region of interaction with the quartz.

After strong measurement, the real part of the weak value is proportional to the average position $\langle x\rangle$ of the post-selected intensity distribution immediately behind the quartz. The quartz plane was imaged onto the camera by two sets of relay optics. The first set imaged ($2f_1-2f_2$ imaging system, $f_1 = 100$ mm, $f_2 = 125$ mm) to a spatial filter (adjustable iris) that allowed us to eliminate back-reflections created in the quartz crystal. The second set imaged ($2f_1-2f_2$ imaging system, $f_1 = 75$ mm, $f_2 = 250$ mm) the iris plane onto the camera. The imaginary part of the weak value is proportional to the average position of the intensity distribution in the far-field $\langle p_x\rangle$ of the quartz plane. A Fourier-transform lens ($f = 300$ mm) mapped the far-field distribution of the iris plane onto the camera.

We established the expectation value of each pointer by first integrating each intensity distribution $I(x, y)$ along $y$ to find $I(x) = \sum_{y\ \text{pixels}} I(x, y)\Delta y$, followed by finding the average $\langle x\rangle = \sum_{x\ \text{pixels}} xI(x)\Delta x / \sum_{x\ \text{pixels}} I(x)\Delta x$. This procedure was repeated with the image of the far-field to establish $\langle p_x\rangle$, and for each strong measurement outcome.

The expectation values $\langle x\rangle$ and $\langle p_x\rangle$ of the pointer, and their corresponding standard deviations, were established by averaging 100 CCD images, each with a 2,000-μs exposure time. The only exception was for the data used to calibrate the weak values for Fig. 4b, where we averaged over 50 CCD images, each with a 500-μs exposure time. This was to reduce the effect of spot drift over the course of the calibration run where many states were measured sequentially.

A simple background subtraction was performed before calculating the pointer's position and momentum. We subtracted the value of the minimum pixel from all pixels on each exposure to reduce the effect that the background had on calculating the average. For the post-selection probability measurements used to determine the Dirac distribution, background subtraction was performed for each region of interest by subtracting the recorded intensity when the laser was blocked. The intensity after background subtraction of the near-field image corresponding to the outcome $|D\rangle$ was $I_D$ and for $|A\rangle$ was $I_A$. Thus, the probabilities were calculated according to $p_D = I_D/(I_D + I_A)$ and $p_A = I_A/(I_D + I_A)$.

The weak value was obtained from average pixel number by

$$\langle \pi_H\rangle_D^W = a\langle x\rangle - b + i(c\langle p_x\rangle - d) \tag{6}$$

where $a$, $b$, $c$, $d$ are constants that must be determined by calibrating the measurement apparatus. Another set of calibration constants $a'$, $b'$, $c'$, $d'$ must be determined for the post-selection of $|A\rangle$ to convert average pixel to $\langle \pi_H\rangle_A^W$. We performed calibrations of the measurement apparatus by measuring the wavefunctions and Dirac distributions of known pure states and comparing $\langle x\rangle$ and $\langle p_x\rangle$ to theoretically calculated weak values.

Received 20 August 2012; accepted 14 January 2013; published online 3 March 2013

## References


1. D'Ariano, G. M., Paris, M. G. A. & Sacchi, M. F. Quantum tomography. *Adv. Imag. Electron. Phys.* **128,** 205–308 (2003).
2. Banaszek, K., D'Ariano, G. M., Paris, M. G. A. & Sacchi, M. F. Maximum-likelihood estimation of the density matrix. *Phys. Rev. A* **61,** 010304 (1999).
3. White, A. G., James, D. F. V., Munro, W. J. & Kwiat, P. G. Exploring Hilbert space: accurate characterization of quantum information. *Phys. Rev. A* **65,** 012301 (2001).
4. Itatani, J. *et al.* Tomographic imaging of molecular orbitals. *Nature* **432,** 867–871 (2004).
5. Resch, K. J., Walther, P. & Zeilinger, A. Full characterization of a three-photon Greenberger–Horne–Zeilinger state using quantum state tomography. *Phys. Rev. Lett.* **94,** 070402 (2005).
6. Agnew, M., Leach, J., McLaren, M., Roux, F. S. & Boyd, R. W. Tomography of the quantum state of photons entangled in high dimensions. *Phys. Rev. A* **84,** 062101 (2011).
7. Lundeen, J. S., Sutherland, B., Patel, A., Stewart, C. & Bamber, C. Direct measurement of the quantum wavefunction. *Nature* **474,** 188–191 (2011).
8. Lundeen, J. S. & Bamber, C. Procedure for direct measurement of general quantum states using weak measurement. *Phys. Rev. Lett.* **108,** 070402 (2012).
9. Dirac, P. A. M. On the analogy between classical and quantum mechanics. *Rev. Mod. Phys.* **17,** 195–199 (1945).
10. Chaturvedi, S. *et al.* Wigner–Weyl correspondence in quantum mechanics for continuous and discrete systems—a Dirac-inspired view. *J. Phys. A* **39,** 1405–1423 (2006).
11. Hofmann, H. F. Complex joint probabilities as expressions of reversible transformations in quantum mechanics. *New J. Phys.* **14,** 043031 (2012).
12. Feynman, R. P. Negative probability. In *Quantum Implications: Essays in Honour of David Bohm* Ch. 13 (eds Healy, B. J. & Peat, F. D.) 235–248 (Routledge, 1987).
13. Leonhardt, U. Quantum-state tomography and discrete Wigner function. *Phys. Rev. Lett.* **74,** 4101–4105 (1995).
14. Mukamel, E., Banaszek, K., Walmsley, I. & Dorrer, C. Direct measurement of the spatial Wigner function with area-integrated detection. *Opt. Lett.* **28,** 1317–1319 (2003).
15. Smith, B. J., Killett, B., Raymer, M., Walmsley, I. & Banaszek, K. Measurement of the transverse spatial quantum state of light at the single-photon level. *Opt. Lett.* **30,** 3365–3367 (2005).
16. Aharonov, Y., Albert, D. Z. & Vaidman, L. How the result of a measurement of a component of the spin of a spin-1/2 particle can turn out to be 100. *Phys. Rev. Lett.* **60,** 1351–1354 (1988).
17. Duck, I. M., Stevenson, I. M. & Sudarshan, E. C. G. The sense in which a weak measurement of a spin-1/2 particle's spin component yields a value 100. *Phys. Rev. D* **40,** 2112–2117 (1989).
18. Knight, J. M. & Vaidman L. Weak easurement of photon polarization. *Phys. Lett. A* **143,** 357–361 (1990).
19. Ritchie, N. W. M., Story, J. G. & Hulet, R. G. Realization of a measurement of a weak value. *Phys. Rev. Lett.* **66,** 1107–1110 (1991).
20. Wiseman, H. Weak values, quantum trajectories, and the cavity-QED experiment on wave–particle correlation. *Phys. Rev. A* **65,** 032111 (2002).
21. Solli, D. R., McCormick, C. F., Chiao, R. Y., Popescu, S. & Hickmann, J. M. Fast light, slow light, and phase singularities: A connection to generalized weak values. *Phys. Rev. Lett.* **92,** 043601 (2004).
22. Resch, K. J., Lundeen, J. S. & Steinberg, A. M. Experimental realization of the quantum box problem. *Phys. Lett. A* **324,** 125–131 (2004).
23. Johansen, L. Weak measurements with arbitrary probe states. *Phys. Rev. Lett.* **93,** 120402 (2004).
24. Pryde, G. J., O'Brien, J. L., White, A. G., Ralph, T. C. & Wiseman, H. M. Measurement of quantum weak values of photon polarization. *Phys. Rev. Lett.* **94,** 220405 (2005).
25. Hosten, O. & Kwiat, P. Observation of the spin hall effect of light via weak measurements. *Science* **319,** 787–790 (2008).

26. Dixon, P. B., Starling, D. J., Jordan, A. N. & Howell, J. C. Ultrasensitive beam deflection measurement via interferometric weak value amplification. *Phys. Rev. Lett.* **102,** 173601 (2009).
27. Popescu, S. Viewpoint: weak measurements just got stronger. *Physics* **2,** 32 (2009).
28. Kocsis, S. *et al.* Observing the average trajectories of single photons in a two-slit interferometer. *Science* **332,** 1170–1173 (2011).
29. Feizpour, A., Xing, X. & Steinberg, A. M. Amplifying single-photon nonlinearity using weak measurements. *Phys. Rev. Lett.* **107,** 133603 (2011).
30. De Gosson, M. A. & de Gosson, S. M. Weak values of a quantum observable and the cross-Wigner distribution. *Phys. Lett. A* **376,** 293–296 (2012).
31. Edgar, M. P. *et al.* Imaging high-dimensional spatial entanglement with a camera. *Nature Commun.* **3,** 984 (2012).
32. Lundeen J. S. & Resch, K. J. Practical measurement of joint weak values and their connection to the annihilation operator. *Phys. Lett. A* **334,** 337–344 (2005).
33. Wootters, W. K. & Fields, B. D. Optimal state-determination by mutually unbiased measurements. *Ann. Phys.* **191,** 363–381 (1989).
34. Geszti, T. Postselected weak measurement beyond the weak value. *Phys. Rev. A* **81,** 044102 (2010).
35. Agnew, M., Leach, J. & Boyd, R. W. Observation of entanglement witnesses for orbital angular momentum states. *Eur. Phys. J. D* **66,** 156 (2012).
36. Simmons, S. *et al.* Entanglement in a solid-state spin ensemble. *Nature* **470,** 69–72 (2011).
37. Steger, M. Quantum information storage for over 180 s using donor spins in a $^{28}$Si 'semiconductor vacuum'. *Science* **336,** 1280–1283 (2012).
38. Di Lorenzo, A. Full counting statistics of weak-value measurement. *Phys. Rev. A* **85,** 032106 (2012).


## Acknowledgements

The authors thank K. Piché and F. Miatto for helpful discussions, and P.B. Corkum and C. Zhang for lending us the quartz crystal. This work was supported by the Canada Excellence Research Chairs (CERC) Program. In addition, R.W.B. acknowledges support from the DARPA InPho program.

## Author contributions

J.Z.S. initiated the study. The experiment was designed by J.Z.S., A.S.J., E.B. and J.L. The experiment was performed by J.Z.S., M.A. and A.S.J., and data analysis was performed by J.Z.S. R.W.B. supervised all aspects of the project. All authors contributed to the text of the manuscript.

## Additional information

Supplementary information is available in the online version of the paper. Reprints and permission information is available online at http://www.nature.com/reprints. Correspondence and requests for materials should be addressed to J.Z.S.

## Competing financial interests

The authors declare no competing financial interests.

nature photonics

SUPPLEMENTARY INFORMATION

DOI: 10.1038/NPHOTON.2013.24

# Full characterisation of polarisation states of light via direct measurement: Supplementary Information

Jeff Z. Salvail,[1†] Megan Agnew,[1] Allan S. Johnson,[1] Eliot Bolduc,[1] Jonathan Leach,[1] Robert W. Boyd[1,2]

[1] *Dept. of Physics, University of Ottawa, Ottawa, Canada*

[2] *Institute of Optics, University of Rochester, Rochester, USA and*

[†] *e-mail: jeff.salvail@gmail.com*

## Note 1: Mutually unbiased bases

Two bases $\mathcal{A}$ and $\mathcal{B}$ are said to be mutually unbiased if $|\langle a_i|b_j\rangle|^2 = 1/N$ for all states $|a_i\rangle$ in $\mathcal{A}$ and all states $|b_j\rangle$ in $\mathcal{B}$, where $N$ is the dimension of the Hilbert space in which $|\psi\rangle$ lives and upon which $\rho$ operates [1]. The indices $i$ and $j$ take the integers from 0 to $N-1$. For example, the horizontal/vertical polarisation basis $\mathcal{A} = \{|H\rangle, |V\rangle\}$ is mutually unbiased with respect to the diagonal/anti-diagonal polarisation basis $\mathcal{B} = \{|D\rangle = 1/\sqrt{2}(|H\rangle + |V\rangle), |A\rangle = 1/\sqrt{2}(|H\rangle - |V\rangle)\}$.

## Note 2: The wavefunction and weak values

We summarize the technique proposed and performed by Lundeen *et al.* in Ref. [2], where a spatial wavefunction of an ensemble of single photons was measured directly, using polarisation as the pointer.

Recall that any state vector $|\psi\rangle$ in the Hilbert space spanned by $\mathcal{A}$ can be written as

$$|\psi\rangle = \sum_i c_i |a_i\rangle, \tag{1}$$

where each $c_i \equiv \langle a_i|\psi\rangle$ is a probability amplitude that cannot be accessed directly by strong measurements. The set $\{c_i\}$ is the wavefunction of the state expressed in the $\mathcal{A}$ basis.

Consider a weak measurement of the projection operator $\pi_{a_i} \equiv |a_i\rangle\langle a_i|$, and post-selection on a state $|\phi\rangle = |b_j\rangle$, where $|b_j\rangle$ and $|a_i\rangle$ are states in mutually unbiased bases. In this case, the definition gives the weak value

$$\langle \pi_{a_i} \rangle^W_{b_j} = \frac{\langle b_j|a_i\rangle\langle a_i|\psi\rangle}{\langle b_j|\psi\rangle} = \frac{1}{\nu}\langle a_i|\psi\rangle, \tag{2}$$

where $\nu$ is a constant of normalisation and is equal to

$$\nu = \frac{\langle b_j|\psi\rangle}{\langle b_j|a_i\rangle}. \tag{3}$$

Crucially, for the specific case where the weak and final measurements are mutually unbiased, the magnitude of the constant $\nu$ is independent of $i$. In general, only for one choice of $|b_j\rangle$ will the phase of $\nu$ be independent of $i$. This ensures that the weak values are proportional through $\nu$ to the complex probability amplitudes $c_i$. Thus, we can substitute the $c_i$ in equation (1) with the normalised weak values from equation (2) to re-express the wavevector as

$$|\psi\rangle = \nu \sum_i \langle \pi_{a_i} \rangle^W_{b_j} |a_i\rangle. \tag{4}$$

Observation of the wavefunction is therefore performed by measuring each coefficient in turn and normalising the magnitude of the wavefunction to unity, which determines $\nu$.

The wavefunction is determined by measuring the pointer state. The pointer's position indicates the real part of the weak value $\mathrm{Re}[\langle \pi_{a_i} \rangle^W_{b_j}]$, and the pointer's momentum indicates the imaginary part $\mathrm{Im}[\langle \pi_{a_i} \rangle^W_{b_j}]$ [3]. Returning to the example where the pointer is the spatial degree of freedom, the complex weak value $\langle \pi_{a_i} \rangle^W_{b_j}$ is established by measuring the expectation values $\langle x\rangle$ and $\langle p_x\rangle$ of the spatial mode: $\mathrm{Re}[\langle \pi_{a_i} \rangle^W_{b_j}] = \langle x\rangle/\delta$ and $\mathrm{Im}[\langle \pi_{a_i} \rangle^W_{b_j}] = k\langle p_x\rangle/\delta$. The constant of proportionality $k = 2\sigma^2/\hbar$, with $\sigma$ the beam waist, is related to the measurement backaction [3].

DOI: 10.1038/NPHOTON.2013.24

In our work, we make use of the fact that not all the weak values $\langle\pi_{a_i}\rangle_{b_j}^W$ are independent. Taking the sum of a complete set of weak values corresponding to projectors $|a_i\rangle\langle a_i|$ with fixed post-selection $|b_j\rangle$, we obtain unity:

$$\begin{aligned}\sum_{i=0}^{N-1}\langle\pi_{a_i}\rangle_{b_j}^W &= \sum_i \frac{\langle b_j|a_i\rangle\langle a_i|\rho|b_j\rangle}{\langle b_j|\rho|b_j\rangle}\\ &= \langle b_j|\left(\sum_i |a_i\rangle\langle a_i|\right)\frac{\rho|b_j\rangle}{\langle b_j|\rho|b_j\rangle}\\ &= 1.\end{aligned} \tag{5}$$

This result is true for any post-selection $|b_j\rangle = |\phi\rangle$ and relies on the fact that $\sum_i |a_i\rangle\langle a_i|$ is equal to the identity operator when the set of all $|a_i\rangle$ is a complete basis. Therefore, measuring all but one weak value is sufficient to determine the wavefunction. Importantly, for a qubit, a single weak value determines the pure state in the two-dimensional Hilbert space.

We now consider the direct measurement of the polarisation wavefunction of a photon. Although the context of our work is polarisation, these results are general and apply to all two-state quantum systems. The polarisation state of a photon can be written as a linear combination of basis elements

$$|\psi\rangle = \alpha|H\rangle + \beta|V\rangle, \tag{6}$$

where $\alpha, \beta$ are complex probability amplitudes, and $|\alpha|^2 + |\beta|^2 = 1$. Recalling equation (4), we may express the polarisation state as

$$|\psi\rangle = \nu\left(\langle\pi_H\rangle_D^W|H\rangle + \langle\pi_V\rangle_D^W|V\rangle\right), \tag{7}$$

where the post-selected state is $|D\rangle$, and therefore mutually unbiased with respect to the measurement operators $\pi_H = |H\rangle\langle H|$ and $\pi_V = |V\rangle\langle V|$. The constant $\nu$ is simply found by normalising the wavefunction and is equal to $(|\langle\pi_H\rangle_D^W|^2 + |\langle\pi_V\rangle_D^W|^2)^{-\frac{1}{2}}$. We now see that the wavefunction is defined in terms of quantities that we can directly measure in the lab. Equation (7) can be simplified by using the fact that $\langle\pi_V\rangle_D^W + \langle\pi_H\rangle_D^W = 1$ as in equation (5). Thus, we may eliminate $\langle\pi_V\rangle_D^W$, and the wavefunction is defined entirely in terms of $\langle\pi_H\rangle_D^W$.

The weak value $\langle\pi_H\rangle_D^W$ can be calculated from its definition and the polarisation state (equation (6)):

$$\begin{aligned}\langle\pi_H\rangle_D^W &= \frac{\langle D|H\rangle\langle H|\psi\rangle}{\langle D|\psi\rangle} = \frac{\alpha}{\alpha+\beta}\\ &= \frac{\cos\theta}{\cos\theta + e^{i\varphi}\sin\theta}.\end{aligned} \tag{8}$$

We take the convention here that the horizontal component has a real coefficient, such that the coefficients are defined by $\alpha = \cos\theta$ and $\beta = e^{i\varphi}\sin\theta$, where $\theta$ is the polarisation angle and $\varphi$ is the phase difference between components. The result of equation (8) can also be obtained through the methods of classical optics. The locations of the peaks of the intensity distributions obtained from the interference of two overlapping Gaussian modes, in the near- and far-fields, are proportional to the real and imaginary parts of equation (8), respectively [4]. In this representation, the two degrees of freedom of a polarisation qubit are $\theta$ and $\varphi$; in terms of weak values, they are the independent real and imaginary parts of $\langle\pi_H\rangle_D^W$. Setting a convention such as this for the phase fixes the gauge, or reference frame, with respect to which the wavefunction is measured. Choosing $\nu$ real actually sets a different phase convention, where the wavevector has an additional global phase coefficient $\exp(-i\arg[\alpha+\beta])$. We plot the wavefunctions in main text Fig. 2, Fig. S1, and Fig. S2 using this phase convention, since it is the natural choice that comes from experiment. The theory curves of main text Fig. 2, Fig. S1, and Fig. S2 are calculated according to equation (8) by setting $\varphi = 0, \pi/2, \pi/4$ respectively, then setting the wavefunction's phase as discussed above.

### Note 3: The Dirac distribution and weak values

We summarize the technique proposed by Lundeen and Bamber in Ref. [5]. The Dirac distribution, named for Dirac who proposed it in Ref. [6], is investigated thoroughly by Chaturvedi *et al.* in Ref. [7]. In our work, we use Chaturvedi *et al.*'s "left" phase-space representative (Dirac distribution) throughout, and discuss only the discrete (i.e., $N$-level)

Hilbert space version. The connection between Dirac distribution, conditional probabilities and the weak value was also explored by Hofmann in [8].

The entry in the $i^{th}$ row and the $j^{th}$ column of the Dirac distribution of the state described by $\rho$ is given by

$$S_{ij} = \langle b_j|a_i\rangle\langle a_i|\rho|b_j\rangle. \tag{9}$$

Recalling the weak value's definition, for weak measurement of a projector $\pi_{a_i}$, we obtain

$$\langle \pi_{a_i}\rangle^W_{b_j} = \frac{\langle b_j|\pi_{a_i}\rho|b_j\rangle}{\langle b_j|\rho|b_j\rangle} = \frac{\langle b_j|a_i\rangle\langle a_i|\rho|b_j\rangle}{\langle b_j|\rho|b_j\rangle}. \tag{10}$$

Substituting equation (10) into equation (9), we now see that the elements of the Dirac distribution that describes a general quantum state can be written in terms of particular weak values that can be directly measured:

$$S_{ij} = \langle b_j|\rho|b_j\rangle\langle \pi_{a_i}\rangle^W_{b_j} = p_{b_j}\langle \pi_{a_i}\rangle^W_{b_j}. \tag{11}$$

That is to say, the $(i,j)^{th}$ element of the Dirac distribution is equal to the result of the weak measurement of $\pi_{a_i}$ with a post-selection on state $b_j$, multiplied by the probability of successful post-selection $p_{b_j} = \langle b_j|\rho|b_j\rangle$. The generalised technique uses the outcome of the strong measurement, and since a mixed state density matrix (and hence Dirac distribution) has more degrees of freedom ($N^2-1$) than a pure state vector ($2N-2$), the strong measurement projection must be scanned through the basis $\mathcal{B}$, in addition to scanning the weak measurement through the complimentary basis $\mathcal{A}$.

To calculate the density matrix $\rho$ from the Dirac distribution $S$, a simple row-by-row discrete Fourier transform can be used, since the $H/V$ basis and $D/A$ basis are not only mutually unbiased but Fourier bases. The relation is

$$\rho_{ij} = \sum_{k=0}^{N-1} S_{ik}\exp\left(\frac{2\pi\imath}{N}(i-k)j\right). \tag{12}$$

In equation (12), we use $\imath$ to denote the imaginary unit which is distinct from the index $i$.

In terms of experiment outcomes, the Dirac distribution is

$$S = \underbrace{\left.\begin{pmatrix} p_D\langle \pi_H\rangle^W_D & p_A\langle \pi_H\rangle^W_A \\ p_D\langle \pi_V\rangle^W_D & p_A\langle \pi_V\rangle^W_A \end{pmatrix}\right\}}_{\text{Right basis axis } |D\rangle,|A\rangle} \text{Left basis axis } \langle H|,\langle V|. \tag{13}$$

Using equation (12) with $N = 2$, we obtain the density matrix

$$\rho = \begin{pmatrix} p_D\langle \pi_H\rangle_D + p_A\langle \pi_H\rangle_A & p_D\langle \pi_H\rangle_D - p_A\langle \pi_H\rangle_A \\ p_D\langle \pi_V\rangle_D - p_A\langle \pi_V\rangle_A & p_D\langle \pi_V\rangle_D + p_A\langle \pi_V\rangle_A \end{pmatrix}. \tag{14}$$

Both axes of this density matrix use the $H/V$ basis.

DOI: 10.1038/NPHOTON.2013.24

## Additional Data

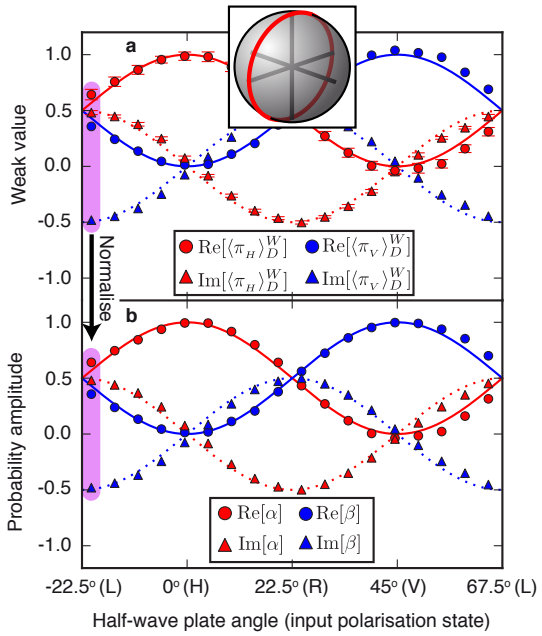


Fig. S1: **Results of experiment 1 with elliptically polarised probe states.** These states created by passing linearly polarised light through a quarter-wave plate with fast axis at 0°. **a,** Measured average weak values plotted as a function of half-wave plate angle, 0° is defined as fast-axis parallel to the optical table. Error bars are shown only for the red points for clarity, and indicate the standard deviation of 100 independently measured weak values. **b,** Real and imaginary components of the probability amplitudes determined by normalising the weak values of each test state, where $|\psi\rangle = \alpha|H\rangle + \beta|V\rangle$. For both panels, the solid lines are the theoretical predictions of the real components, and the dotted lines are the theoretical predictions of the imaginary components. **Inset:** A Poincaré sphere with the path taken indicated by the red line.

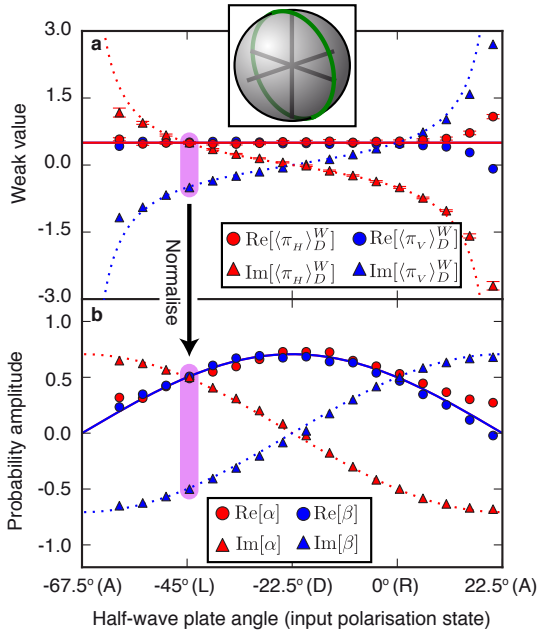


Fig. S2: **Results of experiment 1 with elliptically polarised probe states.** These states created by passing linearly polarised light through a quarter-wave plate with fast axis at 45°. **a,** Measured average weak values plotted as a function of half-wave plate angle, 0° is defined as fast-axis parallel to the optical table. Error bars are shown only for the red points for clarity, and indicate the standard deviation of 100 independently measured weak values. **b,** Real and imaginary components of the probability amplitudes determined by normalising the weak values of each test state, where $|\psi\rangle = \alpha|H\rangle + \beta|V\rangle$. For both panels, the solid lines are the theoretical predictions of the real components, and the dotted lines are the theoretical predictions of the imaginary components. **Inset:** A Poincaré sphere with the path taken indicated by the green line.


[1] Wootters, W. K. & Fields, B. D. Optimal state-determination by mutually unbiased measurements. *Ann. Phys.*, **191,** 363-381 (1989).

[2] Lundeen, J. S., Sutherland, B., Patel, A., Stewart, C. & Bamber, C. Direct measurement of the quantum wavefunction. *Nature*, **474,** 188-191 (2011).

[3] Lundeen J. S. & Resch, K. J. Practical measurement of joint weak values and their connection to the annihilation operator. *Phys. Lett. A*, **334.** 337-344 (2005).

[4] Ritchie, N. W. M., Story, J. G. & Hulet, R. G. Realization of a measurement of a weak value. *Phys. Rev. Lett.*, **66,** 1107-1110 (1991).

[5] Lundeen J. S. & Bamber, C. Procedure for direct measurement of general quantum states using weak measurement. *Phys. Rev. Lett.*, **108,** 70402 (2012).

[6] Dirac, P. A. M. On the analogy between classical and quantum mechanics. *Rev. Mod. Phys.*, **17,** 195-199 (1945).

[7] Chaturvedi, S. *et al.* Wigner-Weyl correspondence in quantum mechanics for continuous and discrete systems—a Dirac-inspired view, *J. Phys. A*, **39,** 1405-1423 (2006).

[8] Hofmann, H. F. Complex joint probabilities as expressions of reversible transformations in quantum mechanics. *New J. Phys.*, **14,** 043031 (2012).

# Chapter 4

# Optimal quantum key distribution with photons entangled in orbital angular momentum

**This chapter is based on the following paper:**

1. J. Leach, **E. Bolduc**, D. J. Gauthier, and R. W. Boyd, "Secure information capacity of photons entangled in many dimensions," *Physical Review A*, vol. 85, no. 6, p. 060304, 2012

## 4.1 Introduction to quantum key distribution

Quantum key distribution (QKD) is a quantum cryptography protocol which guarantees absolute security between two communicating parties, Alice and Bob. The shared information is secure in the sense that the presence of an eavesdropper can always be detected. We first review a famous QKD protocol which works with single photons and then describe a variant of this protocol for entangled photons.

### 4.1.1 The BB84 protocol

After the publication of the no-cloning theorem by Wootter and Zurek in 1982 [29], Bennet and Brassard realized that the laws of quantum mechanics allow for absolute security. They developed a quantum key distribution protocol now known as the BB84 protocol [30], whereby Alice securely communicates a private key to Bob. Essentially,

Alice prepares a two-dimensional quantum state $|\psi\rangle$ in one of the four following forms: $|1\rangle$, $|2\rangle$, $|+\rangle$ or $|-\rangle$, where $|+\rangle$ and $|-\rangle$ are the superposition states $(|1\rangle + |2\rangle)/\sqrt{2}$ and $(|1\rangle - |2\rangle)/\sqrt{2}$, respectively. The states $|1\rangle$ and $|2\rangle$ can correspond to any degree of freedom of light, but Bennet and Brassard chose polarization in the original proposal. After Alice sends her prepared state through a communication channel, Bob receives it and performs a single projective measurement either in the eigenstate basis $\{|1\rangle, |2\rangle\}$ or the superposition basis $\{|+\rangle, |-\rangle\}$. If his choice of basis is the same one as Alice's, the outcome of a measurement corresponds exactly to the prepared state. However, if Alice's and Bob's choices differ, there is a 50% chance that the outcome of Bob's measurement be wrong. For example, if Alice prepared the state $|+\rangle$, but Bob performs a projective measurement in the eigenstate basis $\{|1\rangle, |2\rangle\}$, the outcome is completely random: $|\langle +|1\rangle|^2 = |\langle -|1\rangle|^2 = 1/2$. Therefore, Alice and Bob discard the events where their choice of basis differ, and only keep the informationally relevant ones. They repeat the above process until the key is long enough for their purposes.

Let us study the presence of an eavesdropper, otherwise called Eve, on the result of the protocol. Eve intercepts the state prepared by Alice and performs a projective measurement on it in one of the two bases. She then prepares a state which corresponds to the outcome of her measurement, and sends it to Bob. She tries to go unnoticed, but this is fundamentally impossible. When Alice and Bob make the same choice of basis, Eve makes the wrong one 50% of the time and introduces errors in the communication. For instance, if alice prepares the state $|+\rangle$ and Eve choses the wrong basis, the outcome of her measurement will either correspond to $|1\rangle$ or $|2\rangle$ with equal probability of $1/2$. Bob then makes a measurement in the right basis, but, after the intervention of Eve which irreversibly changed the state, the incorrect outcome $|-\rangle$ is now possible. A careful analysis shows that the above eavesdropping strategy introduces 25% of errors in the system. To check for security, Alice and Bob simply have to compare a subset of their results and verify the error statistics.

### 4.1.2 The Ekert protocol

In the Ekert protocol [31], Alice and Bob each receive one photon of an entangled photon pair. The source of photons produces a Bell state, which could be of the form $|\psi_{\text{Bell}}\rangle = |1\rangle_A|1\rangle_B + |2\rangle_A|2\rangle_B$, where the subscripts $A$ and $B$ stand for Alice's and

Bob's photon, respectively. Alice's and Bob's photons are maximally correlated. For instance, the above Bell state can be rewritten in the basis $\{|+\rangle, |-\rangle\}$, and still be correlated: $|\psi_{\text{Bell}}\rangle = |+\rangle_A|+\rangle_B + |-\rangle_A|-\rangle_B$. If they choose the same basis to perform their projective measurement, the outcome of both measurements will be same for every event. When Eve tries to detect and resend one of the photons, she breaks the entanglement and thus the correlations also. Again, to check for her presence, Alice and Bob verify the error statistics.

Alice and Bob must find the maximum amount of extractable secure information given the fraction of noise that they observe. In general, one must assume that Eve optimally uses the laws of quantum mechanics to achieve her goal. In publication 1, we rely on the theory of Cerf *et al.* to quantify the secure bit rate of our implementation of the communication channel of a QKD system [32]. Instead of the above two-dimensional states, we use orbital angular momentum d-dimensional states.

## 4.2 Introduction to orbital angular momentum states of light

In 1992, Allen *et al.* noticed that light beams can carry orbital angular momentum (OAM) [32]. The Laguerre-Gaussian (LG) transverse spatial modes are specified with two quantum numbers: i) the azimuthal number $\ell$ and ii) the radial number $p$. The modes, with notation $\text{LG}_p^\ell$, carry $\ell\hbar$ units of OAM. In our work, we ignore the radial part of the LG modes and only consider the azimuthal part, which is mathematically defined by an azimuthally varying phase: $\text{LG}^\ell \propto \exp(i\ell\phi)$, where $\phi$ is the azimuthal degree of freedom in transverse cylindrical coordinates. All the modes $\text{LG}^\ell$, with $\ell \in \mathbb{Z}$, are mutually orthogonal. In our implementation of high-dimensional QKD, we use a finite subset of the infinite OAM space. The advantage of using OAM states of light is that there potentially is an infinite number of states to encode with. The density of information encoded into a single photon grows logarithmically with the number of considered states. As shown in publication 1, we construct a superposition basis with the OAM. Before performing a projective measurement, Alice and Bob both choose either the OAM basis and the superposition basis. They only keep the events where they selected the same basis. In the following work, we measure the correlations in both the OAM basis and the superposition basis and calculate the

extractable secure information.

PHYSICAL REVIEW A **85**, 060304(R) (2012)

# Secure information capacity of photons entangled in many dimensions

Jonathan Leach,[1] Eliot Bolduc,[1] Daniel J. Gauthier,[2] and Robert W. Boyd[1,3]
[1]*Department of Physics, University of Ottawa, Ottawa, Ontario, Canada*
[2]*Department of Physics, Duke University, Durham, North Carolina, USA*
[3]*Institute of Optics, University of Rochester, Rochester, New York, USA*
(Received 9 March 2012; published 28 June 2012)

We quantify precisely the maximum secure information capacity of photons entangled in high dimensions for entanglement in the orbital angular momentum and angular degrees of freedom. Our analysis takes careful account of the influence of experimental imperfections, such as nonunity detection efficiency, on the degree of Einstein-Podolsky-Rosen (EPR) entanglement and hence on the secure information capacity of the photon pairs. We find that there is is an optimal dimension that maximizes the secure information capacity whose value can be predicted analytically from the knowledge of only a few experimental parameters.

DOI: 10.1103/PhysRevA.85.060304 PACS number(s): 03.67.Hk, 03.67.Bg, 03.67.Mn, 42.50.−p

*Introduction*. Entanglement is one of the defining properties of quantum mechanics and is a key resource for many quantum information protocols. Systems entangled in high dimensions have recently been proposed as a resource for loophole-free tests of nonlocality [1] in addition to providing dense coding for quantum key distribution (QKD) [2–11]. It is therefore important to understand the mechanisms that affect the degree of entanglement in high-dimensional systems.

The characteristic signature of quantum entanglement is the observation of correlations of spatially separated particles in two or more mutually unbiased bases. One can deduce that the particles are entangled provided that the correlations violate appropriate bounds for separability [12]. The degree of violation of the bound is an important quantity in certain quantum information protocols such as QKD. Crucially, it is known that entanglement is a precondition for secure quantum key distribution [13] and that all entangled states contain secret correlations [14].

Quantum key distribution is a protocol that allows two parties, Alice and Bob, to generate a secure key with which to encode a private message [15–17]. In the Ekert protocol for QKD, Alice and Bob make use of pairs of entangled photons. The protocol is secure against attacks by an eavesdropper, who would necessarily have to disturb the system when attempting to intercept the key. QKD implemented in a high dimensionally entangled space provides the advantages of increased information capacity and higher tolerance to eavesdropping [2–11].

Recent work on high-dimensional spatial entanglement has included studies of full-field position and momentum correlations [18,19] and orbital angular momentum (OAM) and angular position correlations [20–24]. Here, the large Hilbert space of the spatial degree of freedom enables increased information-carrying capacity of the photons compared the two-dimensional polarization degree of freedom.

In this Rapid Communication, we demonstrate the relationship between the degree of Einstein-Podolsky-Rosen (EPR) entanglement of high dimensionally entangled photon pairs and their maximal secure information-carrying capacity. The discrete nature of the OAM states allows us to directly control the size of the state space over a wide range. We find that, because of unavoidable experimental imperfections, there exist both an optimal dimension that maximizes the degree of entanglement and a threshold dimension beyond which there is no entanglement and therefore no secure information. By extracting the key parameters that influence our experiment, we provide a model to predict the maximal secure information capacity of general high dimensionally entangled systems.

*OAM states, angle states, and entanglement*. We consider the OAM modes of light for which there are, in principle, an infinite number of discrete eigenstates. The OAM eigenstates, associated with helical phase fronts $\exp(i\ell\phi)$, are denoted by $|\ell\rangle$. Restricting the size of the state space to a $D$-dimensional space enables the photons to act as qu$D$its. The specific OAM states we consider in our experiment range from $\ell_{\min} = -[(D-1)/2]$ to $\ell_{\max} = [D/2]$, where $[x]$ is the integer part of $x$. Consequently, a basis mutually unbiased with respect to the OAM basis is the angle basis in which the eigenstates are defined by [25–27]

$$|\phi\rangle = \frac{1}{\sqrt{D}} \sum_{\ell=\ell_{\min}}^{\ell_{\max}} e^{i\ell\phi}|\ell\rangle. \tag{1}$$

Here, $\phi = 2\pi n/D$ and $n$ is an integer that ranges from 1 to $D$.

The two photons produced through parametric down-conversion (PDC) are entangled in the OAM and angle degrees of freedom [20–23,28]. The entangled state in the OAM basis is given by

$$|\Psi\rangle = \sum_{\ell=-\infty}^{\infty} c_\ell |\ell_A\rangle|-\ell_B\rangle, \tag{2}$$

where $c_\ell$ is the complex coefficient of the modes, the range of $|c_\ell|^2$ is considered as the spiral bandwidth, and subscripts $A$ and $B$ refer to the signal and idler modes. We probe the state defined in Eq. (2), and we restrict the dimension of the state space by projecting over a finite range of modes.

*Entropic uncertainty relations*. To establish the information content present in a high dimensionally entangled system, consider first the implications of an entropic form of the uncertainty principle for a single particle and then for two entangled particles. For a single particle, one form of the uncertainty principle, which relates the entropies of conjugate variables $X$ and $Y$, is [29,30]

$$H(X) + H(Y) \geqslant \log_2 D. \tag{3}$$

 

The Shannon entropy $H(X)$, which is a measure of information content, is defined by

$$H(X) = -\sum_{n=1}^{D} P(x_n) \log_2 P(x_n), \tag{4}$$

where $P(x_n)$ is the probability of the outcome $x_n$ and $D$ is the dimension of the space. As it is not possible for a single particle to violate inequality (3), it follows that one has complete uncertainty regarding one variable [$H(Y)$ or $H(X) = \log_2 D$] if one has complete knowledge about the other [$H(X)$ or $H(Y) = 0$].

Now consider a pair of high dimensionally entangled particles in systems $A$ and $B$ that exhibit correlations in conjugate degrees of freedom. EPR entanglement can be demonstrated by the violation of the entropic uncertainty relation [12,22,31,32],

$$H_{\text{Inf}}(X_B) + H_{\text{Inf}}(Y_B) \geqslant \log_2 D. \tag{5}$$

Here, $H_{\text{Inf}}(X_B) = H(X_B|X_A)$ and $H_{\text{Inf}}(Y_B) = H(Y_B|Y_A)$ are the inferred entropies of $B$, given precise knowledge of the state of $A$, for the variables $X$ and $Y$. For a maximally entangled system with no noise, perfect correlations will be observed [$H_{\text{Inf}}(X_B) = H_{\text{Inf}}(Y_B) = 0$], and the inequality will be maximally violated.

Finally, consider the implications of Eq. (5) for the secure information capacity of photons entangled in the OAM and angle degrees of freedom. The inferred entropies, $H_{\text{Inf}}(X_B)$ and $H_{\text{Inf}}(Y_B)$, become $H_{\text{Inf}}(\ell_B)$ and $H_{\text{Inf}}(\phi_B)$ respectively, when we associate $X$ with the OAM basis and $Y$ with the angle basis. For the most general eavesdropping attack ( i.e., a coherent attack) the EPR entanglement condition requires the violation of Eq. (5) to have a secure information capacity greater than zero [4,13,14]. Thus, we reformulate Eq. (5) to provide the upper limit of the secure information capacity measured in bits per photon pair, defined through the relation

$$\Delta I \leqslant \log_2 D - [H_{\text{Inf}}(\ell_B) + H_{\text{Inf}}(\phi_B)]. \tag{6}$$

We note that due to the symmetry of the system and the fact that the OAM and angle measurements are mutually unbiased, Eq. (6) is consistent with the general result of Berta *et al.*, who recently considered the uncertainty principle in the presence of quantum memory [33–35].

*Experiment*. A brief summary of the experimental procedure is as follows. First, we choose a pump power to set the photon-pair generation rate. Second, we select a dimension size to restrict the number of states in the Hilbert space. Third, we record the coincidence rates for the projective measurements over ranges $\ell_A$ and $\ell_B \in \{\ell_{\min}, \ldots, \ell_{\max}\}$, and $\phi_A$ and $\phi_B \in \{2\pi/D, \ldots, 2\pi\}$. From the resulting data set, we calculate the secure information capacity via Eq. (6). The second and third stages are repeated for a range of dimensions. Finally, we repeat the above procedures for a range of different pump powers.

To produce entangled photons, we use a 3-mm-long type I BBO ($\beta$ barium borate) crystal pumped with mode-locked ultraviolet laser of 150 mW average power and $\lambda = 355$ nm (Xcyte, JDSU); see Fig. 1. We use the first diffracted orders of spatial light modulators (Pluto, Holoeye) in combination with optical fibers, 10-nm bandpass filters (Chroma), and

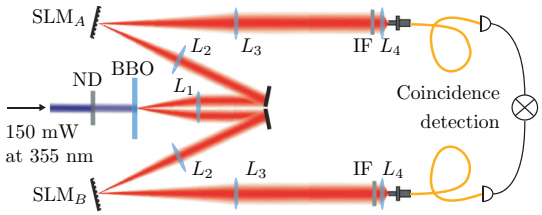


FIG. 1. (Color online) ND, neutral density filter; BBO, $\beta$ barium borate crystal; SLM, spatial light modulator; IF, interference filter; $L_1$, 150 mm; $L_2$, 500 mm; $L_3$, 1000 mm; and $L_4$, 1.45 mm. The combination of the lenses $L_1$ and $L_2$ ($L_3$ and $L_4$), act as a $4f$ imaging system; thus the distance from the crystal to each SLM is 1300 mm (the distance from the SLMs to the fibers is ~2003 mm).

single-photon avalanche photodiodes (Perkin-Elmer) to make projective mode measurements on the entangled photons. The coincidence counting is performed with a timing resolution of 25 ns (National Instruments, PCI-6601). While faster timing electronics are available, our coincidence electronics enables us to investigate the interplay between coincidence rates arising from correlated and uncorrelated events.

For state-space sizes ranging from $D = 2$ to $D = 31$, we perform projective measurements for all possible combinations of the eigenstates in both the OAM and angle bases. These measurements are repeated for four separate pump powers of 0.47, 1.5, 47, and 150 mW. The coincidence counts in the OAM basis are measured using phase-only holograms and single-mode fibers. The angle-state coincidence counts are measured using multimode fibers with the holograms on the SLMs encoded with both the phase and intensity profile of the mode.

*Results*. Samples of the measured correlations are shown in Fig. 2. The two identifiable sources of errors in the data are cross-talk events and uncorrelated coincidences that arise from a nonunity heralding efficiency and finite-timing coincidence electronics. To quantify the degree of EPR entanglement, we calculate $H_{\text{Inf}}(\ell_B)$ and $H_{\text{Inf}}(\phi_B)$ for all of the state space sizes and pump powers; see Fig. 3. As a result of the reduced uncorrelated coincidence count rate, the maximal violation occurs with lowest pair generation rate (ND = 1.5). We can see clearly that increasing the state-space size beyond a certain threshold leads to an inability to confirm the entanglement.

*Estimation of the secure information*. In our model we assume that we generate a maximally entangled state and that the signal and idler arms have identical properties. Thus, the

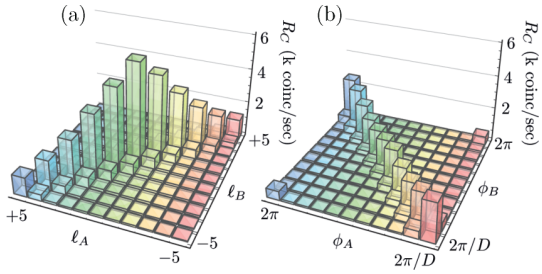


FIG. 2. (Color online) Coincidence count rates for the OAM basis (a) and the angle basis (b) for the case of $D = 11$. For this data set, there is no neutral density filter placed between the pump and the BBO crystal. The integration time for each measurement point is 1 s.

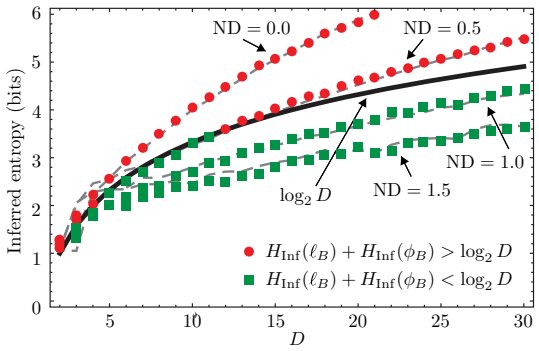


FIG. 3. (Color online) Inferred entropy $H_{\text{Inf}}(\ell_B) + H_{\text{Inf}}(\phi_B)$ as a function of dimension $D$ and pair generation rate. The green squares represent the conditions where inequality (5) is violated and hence the secure information is greater than zero; the red circles represent the conditions where it is not violated and hence there can be no secure information. The gray dashed lines are the theoretical predictions based on our model.

only sources of error are accidental coincidences and cross talk among measurement channels. The parameters that we include are the heralding efficiency $\eta$, the single-photon rates at each detector $S$, the finite resolution of the timing electronics $\Delta t$, and the cross-talk probability $P_X$. We define cross-talk counts as coincidences measured in the two channels adjacent to the signal channel minus the anticipated uncorrelated coincidences.

The joint detection of a photon at detector $A$ and a photon at detector $B$ results in a coincidence. This can be either a coincidence arising from an entangled photon pair or an accidental coincidence arising from uncorrelated events with a probability $P_U = S(1-\eta)^2\Delta t$. The coincidence rates arising from the entangled pairs $R_C$, cross talk $R_X$, and uncorrelated events $R_U$ are given by

$$R_C = S\eta, \quad R_X = R_C P_X, \quad \text{and} \quad R_U = SP_U. \tag{7}$$

Given the assumptions that we have made, the inferred entropies in each basis will be equal. Thus, the calculation of the secure information only requires the inferred entropy in one basis. Assuming $P(x_A) = P(x_B) = 1/D$, the inferred entropy of $X_B$ can be expressed as

$$H_{\text{Inf}}(X_B) = -\frac{R_C + R_U}{R_T}\log_2\frac{R_C + R_U}{R_T} - 2\frac{R_X + R_U}{R_T} \times \log_2\frac{R_X + R_U}{R_T} - (D-3)\frac{R_U}{R_T}\log_2\frac{R_U}{R_T}. \tag{8}$$

Here, the total coincidence rate is given by $R_T = R_C + 2R_X + (D \times R_U)$.[1] The first term of Eq. (8) can be associated with coincidences arising from both entangled pairs and uncorrelated events, the second with both cross-talk and uncorrelated events, and the third solely with uncorrelated events. To gain insight as to why we may not violate Eq. (5), we see that to the first approximation, the third term in Eq. (8) causes $H_{\text{Inf}}(X_B)$ to increase linearly as a function of the size

[1]For the case of $D = 2$, we include only the first two terms of Eq. (8) and the second term is divided by two.

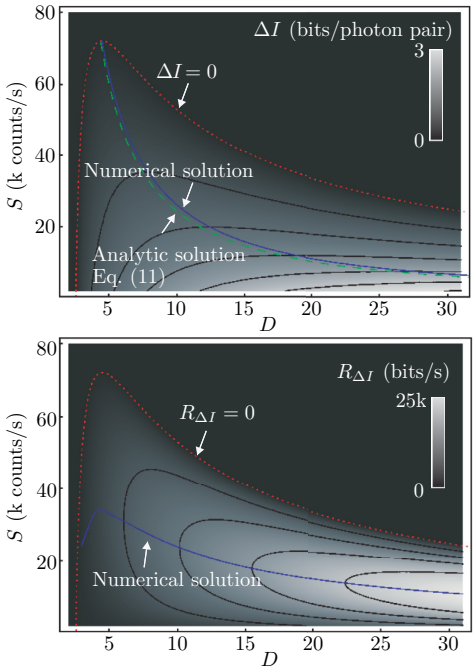


FIG. 4. (Color online) Contour plots of the maximum secure information capacity $\Delta I$ and information rate $R_{\Delta I}$ ($\eta = 5\%$, $P_X = 10\%$, and $\Delta t = 25$ ns). The red dotted lines indicate the threshold to achieve a positive $\Delta I$ and $R_{\Delta I}$, the green dashed line indicates the analytical solution for the optimal dimension $D_{\text{opt}}$ given singles rate $S$, and the blue solid lines indicate the numerically found maxima.

of the space. As a result, the left-hand side of Eq. (5) will be greater than $\log_2 D$ beyond a certain dimension.

An estimate of the maximum secure information capacity is given by inserting Eq. (8) into Eq. (6) [33]:

$$\Delta I(S,\eta,P_U,P_X,D) \leqslant \log_2 D - 2[H_{\text{Inf}}(X_B)]. \tag{9}$$

Equation (9) can be used to determine the experimental conditions that are required to obtain a given level of performance for various situations. For example, the information rate $R_{\Delta I} = S\eta D\Delta I$ measured in bits per sec is most important for QKD, whereas the degree of entanglement $\Delta I$ in bits per photon pair is most important for tests of local hidden variable theories. If one is concerned with maximizing $R_{\Delta I}$, one operates in the maximal possible dimension $D$ and then finds the optimal singles rate $S_{\text{opt}}$. On the other hand, one operates in the maximal possible dimension $D$ with the lowest possible singles rate $S$ if one is concerned with maximizing $\Delta I$.

For parameters appropriate to our experimental conditions, Fig. 4 illustrates the influence of the singles rate and dimension on the secure information capacity and maximum achievable secure bit rate. Note that for a given singles channel rate, there is a maximum in the secure information capacity that occurs at a specific dimension. By solving $\partial_D \Delta I = 0$ for $D$, we we find that

$$D_{\text{opt}}(P_U,\eta) = \frac{\eta}{P_U}\left(\sqrt{\left(\ln\frac{\eta}{P_U}\right)^2 + 1} - \ln\frac{\eta}{P_U}\right), \tag{10}$$

where we have made use of the approximation $(\eta + P_U)/P_U \approx \eta/P_U$ (see the green dashed line in Fig. 4). Equation (10)

provides the optimal dimension for both $\Delta I$ and, to first approximation, the equation scales as $1/S$.

The secure information capacity and maximum secure information rate can fall to zero; the threshold for this behavior is indicated in the figure by the red dotted lines. A secure information capacity of zero occurs at high single-photon rates, where uncorrelated coincidences dominate, and when the dimension of the space is low, where cross talk dominates. In addition, the maximum secure information rate is optimized by maximizing $D$ and then finding the appropriate singles rate $S$. As $\partial_S R_{\Delta I} = 0$ is not easily solved for $S$, we numerically solve to find the optimal singles rate for a given dimension.

*Conclusions*. We experimentally demonstrate the relationship between state-space size and the degree of EPR entanglement for the case of high dimensionally entangled photons. By relating the degree of entanglement of the photon pairs to the maximal secure information-carrying capacity, we find that, because of experimental limitations, there is an optimal dimensionality that maximizes the secure information capacity. Under the conditions of our experiment, the maximum secure information per photon $\Delta I$ is 1.3 bits. The model presented here provides a clear pathway for obtaining even larger values of $\Delta I$, for example by using coincidence circuitry with a smaller time window $\Delta t$.

*Acknowledgments*. We thank N. Lütkenhaus for discussions regarding this work. This work was supported by the Canada Excellence Research Chairs (CERC) Program and the DARPA InPho program.

[1] T. Vértesi, S. Pironio, and N. Brunner, Phys. Rev. Lett. **104**, 060401 (2010).
[2] H. Bechmann-Pasquinucci and W. Tittel, Phys. Rev. A **61**, 062308 (2000).
[3] N. Gisin *et al*., Rev. Mod. Phys. **74**, 145 (2002).
[4] N. Cerf, M. Bourennane, A. Karlsson, and N. Gisin, Phys. Rev. Lett. **88**, 127902 (2002).
[5] F. Grosshans and P. Grangier, Phys. Rev. Lett. **88**, 057902 (2002).
[6] F. Grosshans and N. J. Cerf, Phys. Rev. Lett. **92**, 047905 (2004).
[7] J. Barreiro, N. K. Langford, N. A. Peters, and P. G. Kwiat, Phys. Rev. Lett. **95**, 260501 (2005).
[8] S. Gröblacher *et al*., New J. Phys. **8**, 75 (2006).
[9] I. Ali-Khan and J. C. Howell, Phys. Rev. A **73**, 031801 (2006).
[10] I. Ali-Khan, C. J. Broadbent, and J. C. Howell, Phys. Rev. Lett. **98**, 060503 (2007).
[11] L. Zhang, C. Silberhorn, and I. A. Walmsley, Phys. Rev. Lett. **100**, 110504 (2008).
[12] M. Reid *et al*., Rev. Mod. Phys. **81**, 1727 (2009).
[13] M. Curty, M. Lewenstein, and N. Lütkenhaus, Phys. Rev. Lett. **92**, 217903 (2004).
[14] A. Acín and N. Gisin, Phys. Rev. Lett. **94**, 020501 (2005).
[15] C. Bennett and G. Brassard, *Proceedings of IEEE International Conference on Computers, Systems and Signal Processing* (IEEE, Ottawa, Canada, 1984), p. 175.
[16] A. K. Ekert, Phys. Rev. Lett. **67**, 661 (1991).
[17] A. Ekert, B. Huttner, G. M. Palma, and A. Peres, Phys. Rev. A **50**, 1047 (1994).
[18] J. Leach *et al*., Phys. Rev. A **85**, 013827 (2012).
[19] P. B. Dixon, G. A. Howland, J. Schneeloch, and J. C. Howell, Phys. Rev. Lett. **108**, 143603 (2012).
[20] A. Mair *et al*., Nature (London) **412**, 313 (2002).
[21] J. Goette, S. Franke-Arnold, and S. M. Barnett, J. Mod. Opt. **53**, 627 (2006).
[22] J. Leach *et al*., Science **329**, 662 (2010).
[23] A. Dada *et al*., Nat. Phys. **7**, 677 (2011).
[24] M. Agnew, J. Leach, M. McLaren, F. S. Roux, and R. W. Boyd, Phys. Rev. A **84**, 062101 (2011).
[25] E. Yao *et al*., Opt. Express **14**, 9071 (2006).
[26] B. Jack, M. Padgett, and S. Franke-Arnold, New J. Phys. **10**, 103013 (2008).
[27] S. Franke-Arnold *et al*., New J. Phys. **6**, 103 (2004).
[28] J. Torres, A. Alexandrescu, and L. Torner, Phys. Rev. A **68** (2003).
[29] H. Maassen and J. B. M. Uffink, Phys. Rev. Lett. **60**, 1103 (1988).
[30] A. Rojas González, J. Vaccaro, and S. M. Barnett, Phys. Rev. A **205**, 247 (1995).
[31] S. Walborn, B. G. Taketani, A. Salles, F. Toscano, and R. L. de Matos Filho, Phys. Rev. Lett. **103**, 160505 (2009).
[32] S. P. Walborn, A. Salles, R. M. Gomes, F. Toscano, and P. H. Souto Ribeiro, Phys. Rev. Lett. **106**, 130402 (2011).
[33] M. Berta *et al*., Nat. Phys. **6**, 659 (2010).
[34] Prevedel *et al*., Nat. Phys. **7**, 757 (2011).
[35] C. F. Li *et al*., Nat. Phys. **7**, 752 (2011).

# Chapter 5

# Simultaneous intensity and phase encryption on a hologram

**This chapter is based on the following paper:**

1. **E. Bolduc**, N. Bent, E. Santamato, E. Karimi, and R. W. Boyd, "Exact solution to simultaneous intensity and phase masking with a single phase-only hologram," *Optics Letters*, 2013, [paper accepted in Optics Letters, but not published yet]

## 5.1 Introduction to phase-only holograms

A hologram is commonly thought of as the result of holography, an optical method for physically encoding the intensity and the phase of a coherently illuminated object [33]. In a more general sense, it consists of a pixelated plane which controls the transmission efficiency and the phase shift of a transverse spatial optical field as a function its two coordinates. More specifically, a phase-only hologram only offers the ability to directly modulate the phase profile of an optical field. For instance, a spatial light modulators (SLM) can display a computer-generated hologram where each pixel is fully transparent and applies an arbitrary phase shift.

### 5.1.1 Intensity masking techniques

There exist methods to control the phase profile of an optical field and *indirectly* modulate its intensity profile with phase-only holograms [34–36]. All of them make

use of a modulated phase carrier frequency on the hologram, i.e., a grating with varying diffraction efficiency. The intensity modulation appears in the first diffracted order of the grating. Usually, the encryption of a phase-only hologram is specified by three functions of the transverse coordinates $x$ and $y$: i) the phase encryption function $\mathcal{F}(x, y)$ ii) the intensity masking function $\mathcal{M}(x, y)$ and iii) the carrier frequency function $C(x, y)$, which is optimal in the case of a blazed grating of the form $2\pi x/\Lambda$, where $\Lambda$ is the period of the grating. If the incident field on the hologram is a plane wave, the phase encryption function $\mathcal{F}(x, y)$ and the intensity masking function $\mathcal{M}(x, y)$ depend on the desired output field. In the following discussions, we assume that the incident field is a plane wave, and that the desired output mode is of the form $\Psi(x, y) = A(x, y)\exp(i\,\Phi(x, y))$, where $A(x, y)$ is its real amplitude distribution, and $\Phi(x, y)$ is its phase profile. For brevity, we will omit to write the argument $(x, y)$ of all the functions.

If no intensity masking is required, the encryption of the phase-only hologram $T(x, y)$ takes the simplest form: $T = \exp[i\mathrm{Mod}(\mathcal{F} + \mathcal{C}, 2\pi)]$, where $\mathcal{F} = \Phi$ and $\mathcal{C} = 2\pi x/\Lambda$. The phase encryption function directly imprints the phase of the desired mode and the grating function sends the mode into the first order efficiently.

The difference between the intensity masking methods lies in the mathematical form of the grating modulation. In the method of Kirk and Jones [34], the grating is directly modulated by the intensity masking function. In this case, the imprinted phase profile $T(x, y)$ on the hologram is of the form

$$T_{\mathrm{Kirk}} = \exp[i\,\mathrm{Mod}(\mathcal{F} + \mathcal{M}\ \mathcal{C}, 2\pi)], \tag{5.1.1}$$

with $\mathcal{F} = \Phi$, $\mathcal{M} = 1 + \mathrm{sinc}^{-1}(A')/\pi$ with $A' = A/\max(A)$, $\mathcal{C} = 2\pi\, x/\Lambda$. The authors find the form of the intensity masking function through a Fourier analysis. Notably, the phase encryption function is still identically equal to the phase profile of the desired output mode.

In the method of Davis *et al.*, the intensity masking function simultaneously modulates the phase encryption function and the grating:

$$T_{\mathrm{Davis}} = \exp[i\,\mathcal{M}\,\mathrm{Mod}(\mathcal{F} + 2\pi\, x/\Lambda, 2\pi)], \tag{5.1.2}$$

where $\mathcal{M}$ and $\mathcal{F}$ are left unspecified for the moment. Crucially, Davis *et al.* derive

the form of the field in the plane of the hologram as a function of the diffraction orders. A detailed derivation can be found in the appendix of reference [35]. The field before spatial filtering can be written in terms of all the orders of diffractions $n$ as follows: $T_{\text{Davis}} = \sum T_n \exp[in\mathcal{F}]$, where $T_n = \exp[i(n-\mathcal{M})\pi]\text{sinc}(\pi(n-\mathcal{M}))$. After spatial filtering of all orders except the first one, we find that the resulting spatial mode is given by

$$T_{1,\text{Davis}} = \exp[i(1-\mathcal{M})\pi + i\mathcal{F}]\text{sinc}(\pi(1-\mathcal{M})). \tag{5.1.3}$$

In the our publication 3, we use a hologram encryption method of the type 5.1.2. By setting $T_{1,\text{Davis}}(x,y) = \Psi(x,y)$, we show the form of $\mathcal{F}$ and $\mathcal{M}$ required to produce the desired optical field exactly.

# Exact solution to simultaneous intensity and phase encryption with a single phase-only hologram

**Eliot Bolduc,[1] Nicolas Bent,[1] Enrico Santamato,[2] Ebrahim Karimi,[1,*] and Robert W. Boyd[1,3]**

[1]*Department of Physics, University of Ottawa, 150 Louis Pasteur, Ottawa, Ontario K1N 6N5, Canada*

[2]*Dipartimento di Scienze Fisiche, Università di Napoli "Federico II", Complesso di Monte S. Angelo, 80126 Napoli, Italy*

[3]*Institute of Optics, University of Rochester, Rochester, New York 14627, USA*

**Corresponding author: ekarimi@uottawa.ca*

Received July 19, 2013; revised August 12, 2013; accepted August 13, 2013;
posted August 14, 2013 (Doc. ID 194221); published September 5, 2013

A phase-only hologram applies a modal transformation to an optical transverse spatial mode via phase encoding and intensity masking. Accurate control of the optical field crucially depends on the method employed to encode the hologram. In this Letter, we present a method to encode the amplitude and the phase of an optical field into a phase-only hologram, which allows the exact control of spatial transverse modes. Any intensity masking method modulates the amplitude and alters the phase of the optical field. Our method consists in correcting for this unwanted phase alteration by modifying the phase encryption accordingly. We experimentally verify the accuracy of our method by applying it to the generation and detection of transverse spatial modes in mutually unbiased bases of dimension two and three. 

*OCIS codes:* (090.1760) Computer holography; (100.5090) Phase-only filters; (070.2580) Paraxial wave optics; (260.6042) Singular optics; (270.5568) Quantum cryptography.
http://dx.doi.org/10.1364/OL.38.003546

The generation of optical fields possessing specific transverse intensity and phase distributions is highly important in many different research areas such as stimulated emission depletion microscopy, optical trapping, optical tweezers, communication, data storage, and fundamental quantum mechanics [1–5]. Nowadays, technologies such as spatial light modulators (SLMs) and assorted controllable micromirrors provide an easy way to generate and manipulate optical fields from computer generated phase-only holograms, otherwise called holographic kinoforms [6,7]. Generating an arbitrary beam accurately requires engineering both phase and amplitude structures simultaneously. The current available devices are fabricated to physically control only the phase or amplitude of an optical field, but not both at the same time. Combining these two devices together allows one to control both the phase and amplitude of an optical field. However, there exists techniques to modulate both properties simultaneously with a single device [8].

Over the course of the last five decades, many intensity-masking methods for holographic kinoforms were proposed by many different groups [9–12]. All these techniques make use of a grating pattern whose diffraction efficiency is modulated by a function of the amplitude of the beam. Indeed, intensity masking, i.e., encrypting an arbitrary function of the amplitude onto a holographic kinoform, is a selective process that diffracts only the desired part of the incoming beam into the first order of diffraction and the undesired part, depending on the techniques, remains in the zero order, diffracts into higher orders or both. The diffraction efficiency depends on the depth of phase of the blazing in the grating pattern; the closer to a full-phase, i.e., $2\pi$, variation in the blazing, the more light diffracts [10]. Such a phase modulation gives the ability to control the diffracted intensity as a function of the transverse coordinates and thus allows one to generate or transform any transverse spatial mode within the capabilities of the device.

Recently, Ando *et al.* numerically compared the purity of the generated mode of different intensity masking methods [13]. These methods can yield good approximations to the desired mode transformation, but an exact solution was yet to be found. In this Letter, we present the exact solution to the necessary phase encoding and intensity masking on a phase-only hologram for any given paraxial mode transformation. We experimentally put our technique to the test by generating and detecting orbital angular momentum (OAM) states of light with two SLMs. We choose OAM subspaces of two and three dimensions and consider the states in all mutually unbiased bases (MUBs), which consists of both eigenstates and superposition states.

In solving the problem of encryption of a holographic kinoform, we use a plane wave as the incident optical field, and define the desired output beam as the following scalar paraxial field:

$$E(\mathbf{r}_\perp, z_0) := A(\mathbf{r}_\perp, z_0) e^{i\Phi(\mathbf{r}_\perp, z_0)}, \tag{1}$$

where $\mathbf{r}_\perp$ stands for the transverse coordinate, $A(\mathbf{r}_\perp, z_0) := |E(\mathbf{r}_\perp, z_0)|$ and $\Phi(\mathbf{r}_\perp, z_0) := \mathrm{Arg}(E(\mathbf{r}_\perp, z_0))$ are the amplitude and phase of the optical field at the $z = z_0$ plane, respectively. As Eq. (1) suggests, a scalar optical field is well-defined in the entire space by two independent real functions, one specifying the amplitude profile and the other specifying the phase distribution. This is fundamentally governed by the angular spectrum method, which defines the optical field at any given $z$ plane uniquely if the initial pupil field function is given. In our derivations, we specify $A$ and $\Phi$ in the plane of the hologram ($z = 0$).

 

Let us first consider the simple case of a holographic kinoform with no intensity masking and an imprinted phase profile of $\Psi(m,n) = \mathrm{Mod}(\Phi(m,n) + 2\pi m/\Lambda, 2\pi)$, where $m$ and $n$ are the pixel coordinates and $\Lambda$ is the period of the blazed grating pattern—the type of grating that maximizes the diffraction efficiency. A Fourier analysis shows that, in the limit of infinitely many pixels, the optical field in the first order of diffraction is simply given by $\tilde{E}_{\mathrm{out}} = \mathrm{FT}[\exp(i\Phi(m,n))]$, where FT corresponds to the Fourier transform. To express the output beam in the near-field of the hologram, the standard procedure is to insert a spatial filter that selects only the first diffracted order and go to the Fourier plane of the spatial filter. The output beam in the near-field of the hologram is then written $E_{\mathrm{out}} = \exp(i\Phi(m,n))$. The encrypted phase profile $\Phi(m,n)$ is directly transferred to the output optical field, whose amplitude stays uniform. In the following section, we show how to simultaneously obtain the exact desired amplitude and phase profiles in the image plane, or near-field, of a hologram.

We now consider a very general case of simultaneous phase and amplitude encoding of a phase-only hologram. The imprinted phase profile on the hologram is given by $\Psi(m,n) = \mathcal{M}(m,n)\mathrm{Mod}(\mathcal{F}(m,n) + 2\pi m/\Lambda, 2\pi)$, where $\mathcal{M}$ is a normalized bounded positive function of amplitude, i.e., $0 \le \mathcal{M} \le 1$, and $\mathcal{F}$ is an analytical function of the amplitude and phase profiles of the desired field. Just after passing through the hologram, the input plane wave acquires the imprinted phase profile and is given by

$$T(m,n) = e^{i\mathcal{M}(m,n)\mathrm{Mod}(\mathcal{F}(m,n)+2\pi m/\Lambda,2\pi)}. \tag{2}$$

A calculation based on a Taylor–Fourier expansion shows that the action of this particular optical phase object—after spatial filtering of all orders except the first one—can be expressed as

$$T_1(m,n) = -\mathrm{sinc}(\pi\mathcal{M} - \pi)e^{i(\mathcal{F}+\pi\mathcal{M})}, \tag{3}$$

where $\mathcal{M}$ and $\mathcal{F}$ are both functions of the transverse coordinates on the hologram, i.e., $\{m,n\}$ [10]. Since the output mode must be exactly equal to the desired field of Eq. (1), we find that the two modulation functions are given by

$$\begin{aligned} \mathcal{M} &= 1 + \frac{1}{\pi}\,\mathrm{sinc}^{-1}(A) \\ \mathcal{F} &= \Phi - \pi\mathcal{M}, \end{aligned} \tag{4}$$

where $\mathrm{sinc}^{-1}(\cdot)$ stands for the inverse function of the sinc, and $\mathrm{sinc}(x) = \sin x/x$ is an unnormalized sinc function in the domain of $[-\pi, 0]$, which accounts for the minus sign in Eq. (3). The form of the intensity modulation function $\mathcal{M}$ is such that there is a linear relationship between the desired amplitude and the encoded amplitude, see solid red curve in Fig. 1. Moreover, we cancel the unwanted phase $\pi\mathcal{M}$ in Eq. (3) by subtracting it in the phase encoding function $\mathcal{F}$. Crucially, Eq. (4) decouples the generated phase profile from the two-dimensional amplitude distribution. Replacing the terms of Eq. (4) into $\Psi(m,n)$, the imprinted phase profile on the hologram, completes the description of our method. Since this result is exact, the fidelity of the generated modes should now only be limited by the capabilities of the device it is used with.

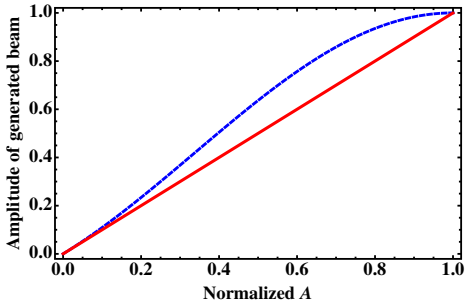


Fig. 1. Amplitude of the generated beam, after selection of the first order of diffraction, as a function of the normalized desired amplitude of Eq. (1). The solid-red curve corresponds to our exact hologram encryption method; the generated amplitude is equal to the desired amplitude. The blue dashed curve is based on the technique reported in [10].

In order to test for the ability to encode and decode information on transverse spatial modes, we experimentally applied our method to the generation and detection of states in MUBs. Eigenstates of $\{|u_i\rangle\}$ and $\{|v_j\rangle\}$ are called MUBs in the Hilbert space of dimension $d$ if $|\langle u_i|v_j\rangle|^2 = 1/d$ for any $i$ and $j$. For a given generated mode, we perform a complete set of projections, whose outcomes allow us to determine the generated mode. The process of reconstructing a state from a complete set of measurement outcomes is know as quantum state tomography. This test is experimentally very reliable, and it is exhaustive, since it requires the generation and detection of all informationally independent eigenstates and superposition states.

Without loss of generality and only for this test, we neglect the radial dependence of the optical field, and we consider only the azimuthal part associated with optical OAM. An optical beam with an azimuthal phase profile of the form $\exp(i\ell\phi)$ carries a well-defined OAM value of $\ell\hbar$ per photon, where $\phi$ is the cylindrical coordinate. These beams are eigenstates of the $z$-component of the OAM operator and form a complete basis in the azimuthal coordinate, $\langle \mathbf{r}|\ell\rangle = \exp(i\ell\phi)$ [5].

MUBs form a complete set of bases. For a Hilbert space of dimension $d$ equal to a prime or the power of a prime, the total number of MUBs is known to be $d+1$ [14]. In the $d = 2$ OAM Hilbert subspace, the $(2+1)$ MUBs are eigenstates of the Pauli matrices. In analogy with polarization, this state space can be mapped on an OAM Poincaré sphere [15]. The set of MUBs in two-dimensional Hilbert space are given by

$$\begin{aligned} \{\mathrm{I}\} &= \{|0\rangle, |1\rangle\} \\ \{\mathrm{II}\} &= \left\{\frac{|0\rangle + |1\rangle}{\sqrt{2}}, \frac{|0\rangle - |1\rangle}{\sqrt{2}}\right\} \\ \{\mathrm{III}\} &= \left\{\frac{|0\rangle + i|1\rangle}{\sqrt{2}}, \frac{|0\rangle - i|1\rangle}{\sqrt{2}}\right\}. \end{aligned} \tag{5}$$

For a three-dimensional OAM Hilbert subspace, the $(3+1)$ MUBs are given by

$$\{\mathrm{I}\}=\{|0\rangle,|1\rangle,|2\rangle\}$$
$$\{\mathrm{II}\}=\left\{\frac{|0\rangle+|1\rangle+|2\rangle}{\sqrt{3}},\frac{|0\rangle+\omega|1\rangle+\omega^2|2\rangle}{\sqrt{3}},\frac{|0\rangle+\omega^2|1\rangle+\omega|2\rangle}{\sqrt{3}}\right\}$$
$$\{\mathrm{III}\}=\left\{\frac{|0\rangle+\omega|1\rangle+\omega|2\rangle}{\sqrt{3}},\frac{|0\rangle+\omega^2|1\rangle+|2\rangle}{\sqrt{3}},\frac{|0\rangle+|1\rangle+\omega^2|2\rangle}{\sqrt{3}}\right\}$$
$$\{\mathrm{IV}\}=\left\{\frac{|0\rangle+\omega^2|1\rangle+\omega^2|2\rangle}{\sqrt{3}},\frac{|0\rangle+\omega|1\rangle+|2\rangle}{\sqrt{3}},\frac{|0\rangle+|1\rangle+\omega|2\rangle}{\sqrt{3}}\right\}, \quad (6)$$

where $\omega=\exp(i2\pi/3)$ [16,17].

We implement our method in computer-generated holograms displayed on cost-effective Cambridge Correlators SLMs, with a resolution of $1024\times786$ pixels. A layout of the experimental setup used to perform the MUB test is shown in Fig. 2. A 3 mm wide single-mode HeNe laser beam goes through a polarizer that optimizes the diffraction efficiency of SLM-A. This SLM transforms the input flat-phase field into any of the states given in Eqs. (5) and (6). The beam then traverses a spatial filter that selects out all but the first order of diffraction. The half-wave plate modifies the polarization to optimize the diffraction efficiency of SLM-B, which applies a second modal transformation to the laser beam. Together with the single-mode fiber (SMF) and an iris, SLM-B projects the generated mode onto an arbitrary mode in Eqs. (5) and (6). We measure the strength of the projections with a power-meter at the output of the SMF. In other words, SLM-A forms the state and SLM-B and SMF together analyze the state.

Because of the fact that we use intensity masking, we have to normalize each projective measurement by the reflection efficiencies of the displayed holograms on each SLM. For example, when displaying an OAM eigenstate on SLM-A, no intensity masking is needed because we ignore the radial degree of freedom and it has a flat azimuthal intensity distribution. However, a superposition state, a so-called *angle* state, requires intensity masking since the azimuthal symmetry is broken. In dimension two, half of the light will be lost. We have to take this mode-dependent reflection efficiency into account. Thus, for each hologram displayed on SLM-A and SLM-B, we measure the power of the reflected light in the first order of diffraction of each SLM, and normalize the projection outcomes by the reflection efficiencies of each SLM. Figure 3 shows the normalized outcomes of the projections for $d=2$ and $d=3$ OAM Hilbert subspaces. We measure the quality of the system with a figure of merit called *similarity* $\mathcal{S}$ [18], an analogous quantity to the fidelity in the case of pair of states. Our system yields similarities of $\mathcal{S}=0.993$ and $\mathcal{S}=0.927$ for dimension two and three, respectively.

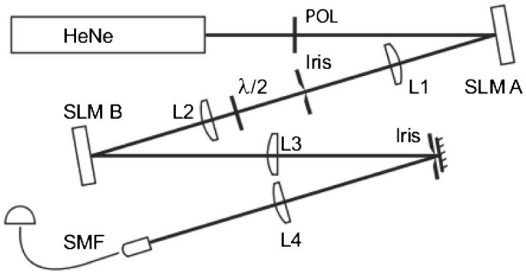


Fig. 2. Layout of the experimental setup used to encode and detect OAM qubit and qutrit states based on our new method. A HeNe laser beam illuminates SLM-A, which generates any of the MUBs. The $4f$ systems made of the lenses {L1,L2} image the plane of SLM-A to that of SLM-B with unit magnification. The SLM-B and a SMF act together as a mode projector on any of the MUBs states. We sequentially display all MUBs states on SLM-A and SLM-B, and acquire all combinations of projections. The last set of lenses, composed of {L3,L4, microscope objective}, take the far-field of SLM-B to the entrance facet of the SMF. The irises act as spatial filters which select the first order of diffraction of SLM-A and SLM-B. As SLMs are polarization sensitive, the polarizer (POL) and the half-wave plate ($\lambda/2$) optimize the diffraction efficiency.

Our method requires the calculation of the inverse sinc function for every pixel on the hologram, and this task can be computationally intensive for a standard computer. For simplicity and speed, it is sometimes more convenient to implement a hologram encryption method that only requires standard functions, unlike the inverse sinc function. We thus propose a simple improvement over the already simple technique first reported by Davis *et al.* [10]. In the case where the intensity modulation function is given by $\mathcal{M}=A$ and $\mathcal{F}=\Phi$, as proposed by Davis *et al.*, the optical transverse mode after spatial filtering is equal to $\mathrm{sinc}(\pi(A-1))\exp(i(\Phi+\pi A))$ in the near-field of the hologram. For this method, the amplitude profile of the generated beam $\mathrm{sinc}(\pi(A-1))$ is always rather close to that of the desired amplitude $A$ [see dashed blue curve in Fig. 1]. In fact, the normalized generated and desired amplitudes are never further apart than 0.161, $|\mathrm{sinc}(\pi(A-1))-A|<0.161$. The difference in amplitude distributions is not as significant as the difference in phase profiles. The generated phase profile can be completely modified by the supplementary term $\pi A$ in the exponential. We thus propose a simple improvement that consists in modifying the phase encryption $\mathcal{F}$ as in Eq. (4): $\mathcal{F}=\Phi-\pi A$. In principle, this new method does not yield an exact replica of the desired field since it does not correct for the gap in amplitude, but it should give good approximations because it solves the problem of the extra phase term, which is much more important.

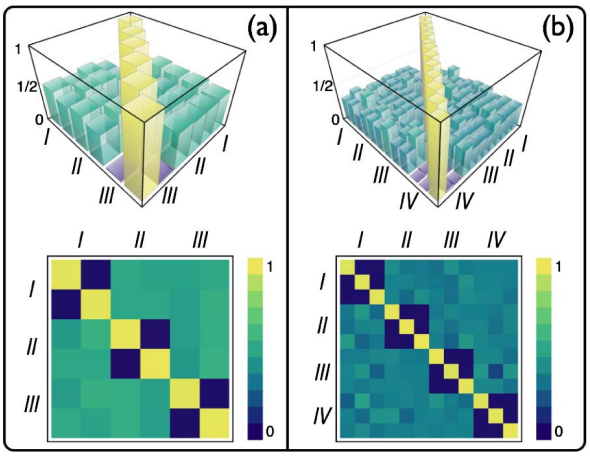


Fig. 3. Experimental projections between states in all MUBs in (a) $d=2$ and (b) $d=3$ OAM Hilbert subspaces, i.e., $P_{ij}=|\langle\alpha_i|\beta_j\rangle|^2$.

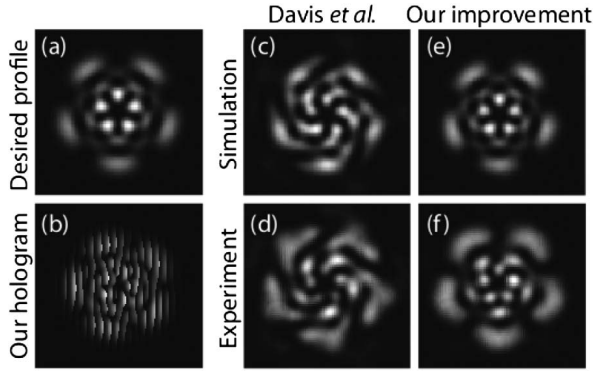


Fig. 4. Qualitative comparison of the method of Davis *et al.* and our proposed improvement of their technique. The desired intensity profile purposely has small features to accentuate the difference between the two methods. The experimentally recorded images are taken in the far-field of a HOLOEYE SLM.

Just like the original method of Davis *et al.*, it has the advantage of being very easy to implement. Note that the proposed method in [10] aimed to encode the *amplitude* of an optical field and not the phase.

We experimentally compare the method of Davis *et al.* with our proposed improvement by recording the intensity profiles of a transverse mode generated with each technique. The desired intensity profiles is that of a superposition of two Laguerre–Gaussian (LG) modes, $\mathrm{LG}_2^{-2} + \mathrm{LG}_1^3$, where $\mathrm{LG}_p^\ell$ is the LG mode with the radial and azimuthal indices of $p$ and $\ell$, respectively. Figure 4 shows the results of a numerical simulation with each method and the experimentally recorded intensity profiles, respectively. Although this comparison is only qualitative, the difference between the intensity profiles of the generated output modes is striking.

In conclusion, we have presented a new way of encoding the amplitude and the phase of an optical field into a pure-phase hologram. The encryption is based on intensity masking, whereby the amplitude distribution of a desired optical field modulates the profile of the encoded phase. In order to measure the accuracy of the method, we performed a complete test over all informationally independent OAM states in the subspaces of dimension two and three, the results of which are in excellent agreement with theory. This result suggests that our method allows the generation of arbitrary transverse spatial modes with high accuracy. We also proposed a simple improvement of the easy-to-implement method of Davis *et al.* A qualitative comparison of the intensity distribution of a mode with small features showed that the improvement is highly significant. We thus showed a very simple way of encoding phase-only holograms for the purpose of generating high fidelity spatial transverse modes.

E. B., N. B., E. K., and R. W. B. acknowledge the support of the Canada Excellence Research Chairs (CERC) Program. E. B. acknowledges the financial support of the FQRNT, grant number 149713. E. S. acknowledges the financial support of the Future and Emerging Technologies (FET) programme within the Seventh Framework Programme for Research of the European Commission, under FET-Open grant number 255914-PHORBITECH.

**References and Note**

1. W. S. Hell, Science **316**, 1153 (2007).
2. H. He, N. R. Heckenberg, and H. Rubinsztein-Dunlop, J. Mod. Opt. **42**, 217 (1995).
3. L. Paterson, M. P. MacDonald, J. Arlt, W. Sibbett, P. E. Bryant, and K. Dholakia, Science **292**, 912 (2001).
4. G. Gibson, J. Courtial, M. J. Padgett, M. Vasnetsov, V. Pasko, S. M. Barnett, and S. Franke-Arnold, Opt. Express **12**, 5448 (2004).
5. S. Franke-Arnold, L. Allen, and M. Padgett, Laser Photon. Rev. **2**, 299 (2008).
6. J. A. Neff, R. A. Athale, and S. H. Lee, Proc. IEEE **78**, 826 (1990).
7. V. Yu. Bazhenov, M. S. Soskin, and M. V. Vasnetsov, J. Mod. Opt. **39**, 985 (1992).
8. V. A. Soifer, eds., *Methods for Computer Design of Diffractive Optical Elements* (Wiley, 2002).
9. J. P. Kirk and A. L. Jones, J. Opt. Soc. Am. **61**, 1023 (1971).
10. J. A. Davis, D. M. Cottrell, J. Campos, M. J. Yzuel, and I. Moreno, Appl. Opt. **38**, 5004 (1999).
11. J. Leach, M. R. Dennis, J. Courtial, and M. J. Padgett, New J. Phys. **7**, 55 (2005).
12. V. Arrizón, U. Ruiz, R. Carrada, and L. A. González, J. Opt. Soc. Am. A **24**, 3500 (2007).
13. T. Ando, Y. Ohtake, N. Matsumoto, T. Inoue, and N. Fukuchi, Opt. Lett. **34**, 34 (2009).
14. W. K. Wootters and B. D. Fields, Ann. Phys. **191**, 363 (1989).
15. M. J. Padgett and J. Courtial, Opt. Lett. **24**, 430 (1999).
16. M. Wieśniak, T. Paterek, and A. Zeilinger, New J. Phys. **13**, 053047 (2011).
17. V. D'Ambrosio, F. Cardano, E. Karimi, E. Nagali, E. Santamato, L. Marrucci, and F. Sciarrino, arXiv:1304.4081.
18. The similarity is defined as $S = \left(\left(\sum_{ij}\sqrt{P_{ij}P'_{ij}}\right)^2 \Big/ \sum_{ij}P_{ij}\sum_{ij}P'_{ij}\right)$, where $P$ and $P'$ stand for experimental and expected theoretical projection matrix.

## 5.3 Supplementary information

### 5.3.1 Pixelated holograms

Our method does not take into account the pixelated nature of the hologram. If the number of pixels in one period of the grating is very low, namely, between 2 and 6, the pixelated nature of the hologram becomes important. High carrier frequencies are advantageous in experiments where the desired mode in the first order of diffraction must be as far as possible from the other orders. This occurs when the mode in question is very large. It would thus be relevant to test our method for such high carrier frequencies, and develop a more accurate one for this particular case.

### 5.3.2 Implications on the results of chapter 4

In the work on quantum key distribution with orbital angular momentum states (OAM) in chapter 4, we were using SLMs to detect OAM states and superpositions of OAM states. We didn't know about the new method presented here and implemented the intensity masking method of Davis *et al.* to calculate the computer-generated holograms for the superposition states, which intensity varies angularly. The inaccuracy of the employed method was thus a source of noise which was unaccounted for at the time. The noise was simply considered as coming from an eavesdropper. As a consequence, we could increase the secure information capacity of our quantum key distribution system by implementing the new hologram encryption method.

### 5.3.3 Computer program

We implemented our method in MATLAB, see appendix B. The program generates a pixelated hologram in the middle of a monitor chosen by the user. This program is also available on the website of the group of Prof. Boyd at the University of Ottawa: http://www.quantumphotonics.uottawa.ca/home.php.

# Chapter 6

# Conclusions and Outlook

We have completed four projects, all of which provide improvements to experimental procedures in either applied or fundamental quantum mechanics.

In the work on duality, we derived a novel relation between average visibility $\langle \mathcal{V} \rangle$ of an interference pattern and which-alternative knowledge $\langle \mathcal{P} \rangle$ in the presence of an environment: $\langle \mathcal{P} \rangle^2 + \langle \mathcal{V} \rangle^2 = 1 - \sigma_{\mathcal{P}}^2 - \sigma_{\mathcal{V}}^2$, where $\sigma_{\mathcal{P}}^2$ and $\sigma_{\mathcal{V}}^2$ are the variances of the predictability and visibility distributions, respectively. The environment allowed the interference pattern to vary, and its visibility has to be viewed as a distribution rather than a single value. Our relation is an equality when the pure state assumption is valid and turns into an inequality when we make no assumption. In the latter case, the bound is as tight as possible and cannot be improved. We pointed out that, instead of measuring the average visibility, Menzel *et al.* observed a single value of the visibility, which corresponded to a single element of the environment. As they did not measure the visibility for every slice of the two-dimensional interference pattern, our relation could not have been tested. Instead, they measured what we call the biased sampling relation: $\mathcal{B} = \mathcal{V}_{\max}^2 + \langle \mathcal{P} \rangle^2$, which is allowed by the laws of quantum mechanics to exceed unity. Duality was safe in this respect, but we went even further and theoretically modeled a similar experiment to that of Menzel *et al.* to test our new duality relation. Our relation is particularly relevant when the visibility varies significantly as a function of the degree of freedom of the environment, which was the case of our thought experiment. As expected, our relation was satisfied. This work explains the surprising experimental results of Menzel *et al.*, and improves the theory on duality. Our relation still has to be experimentally tested.

The second project was on quantum state determination with weak values. We

performed two experiments: i) we directly determined the two complex coefficients of a polarization state of light and ii) directly determined the elements of the corresponding 2-dimensional Dirac distribution. In both experiments, we measured weak values by weakly coupling the polarization state to the spatial degree of freedom with a tilted birefringent crystal. After a projection onto a final polarization state, the real and imaginary parts of a weak value were approximately related to the average position and average momentum of the spatial mode, respectively. In the first experiment, we assumed that the polarization state was pure, and we only needed one weak value to identify the state vector. We applied this procedure to many known initial states. The retrieved states corresponded almost exactly to the expected states except when the expected state was orthogonal to the final projection. In this case, the experimental result diverged from the expected one, because the weak-value approximation broke down. We theoretically quantified the effect of this break down by calculating the average fidelity between arbitrary initial states and the corresponding retrieved states with weak-value-assisted tomography. We found that the method is very accurate in the regime of very weak coupling. It yields an average fidelity higher than 0.998 when the spatial shift of the initial spatial mode is less than half of its 1/e width. The average fidelity decreases exponentially fast with the coupling strength and saturates at 0.873. This analysis was done for two-dimensional initial states, but could be generalizable to D-dimensional systems.

In the work on quantum key distribution, we experimentally implemented important features of quantum key distribution using photons entangled in the angular momentum degree of freedom. Photons pairs were generated through spontaneous parametric downconversion, and their transverse spatial modes were detected with spatial light modulators and singles mode fibers. We recorded the modal correlations between the photon pairs and calculated the amount of extractable secure information. By performing this analysis for many dimensions of the orbital angular momentum state-space, we found the one that maximized the secure information. We theoretically generalized this result by taking into account the photon generation rate, the coincidence detection time window and the non-unity detection efficiency. The experimental results showed that the maximum amount of extractable secure information was 1.3 bits per photon pair. Our theoretical model indicates the changes that have to be made in order to reach a given value of the secure information rate. Notably, it would be very helpful for future experiments if we were to change the

detection electronics to reduce the coincidence time window.

Finally, we showed how to obtain arbitrary spatial modes with a single phase-only hologram. Solutions to this problem already existed, but they were all approximate. We gave the exact solution to simultaneous encryption of the intensity and the phase of a given spatial transverse mode into a phase-only hologram. We quantitatively tested our method with state projections in mutually unbiased bases. In dimension 2 and 3, the metric for how close the results were to the theory, the *similarity*, was 0.993 and 0.927, respectively. Our method could be computationally intensive for it requires the calculation of a non-standard sinc inverse function. We thus provided an improvement over the easy-to-implement technique of Davis *et al.*. We applied an amplitude dependent correction on the phase encryption. As this correction is simple, it doesn't require much computing power. We qualitatively tested this method by observing the intensity pattern of a given mode in the far-field of a spatial light modulator. The improvement was fast and strikingly good. We expect our method to be used for engineering purposes, multiplexing and demultiplexing of spatial transverse modes for instance, and in many areas of research, such as quantum state tomography, microscopy and fundamental quantum mechanics. Since we assumed an infinite number of pixels on the holograms, it would be interesting to study the impact of finite pixel number on our method.

# Appendix A

# MATLAB code for our thought experiment on duality

```
%%%%% Program that computes the two-photon mode functions in the near-field
%%%%% and the far-field of the two-slit mask in a thought experiment
%%%%% inspired by the work of Menzel et. al.

clc;clear;

%%%%%%%% DEFINE PARAMETERS.................(Experiment of Menzel et. al.)
mum=1E-6;           %micrometer.........................................
phi=-19;            %phase-mismatch parameter.........................(?)
L=0.002;            %crystal thickness...............................(2mm)
d=70*mum;           %slit separation..................................(?)
delta=d/4;          %slit width.....................................(d/4)
w0=100*mum;         %pump width.....................................(25mum)
HG=1;               %1 (0) corresponds to a HG01 (Gaussian) pump mode...(1)
lambda=0.405*mum;   %wavelength in vacuum.........................(405nm)
n=1.65;             %index of refraction in the crystal.............(1.65)
kp=2*pi/lambda*n;   %total wavevector of the pump beam inside the crystal
N=1024;             %number of points in computation
wf=10*mum;           %1/e^(1/2) width of the fiber
dell=0;             %offset of the optical fiber
ctrfbr=-d/2-dell;   %y position of the optical fiber
```

```
speed=0;            %if speed=1, reduced resolution on the idler photon
%%%%%%%% END DEFINE PARAMETERS %%%%%%%%%%%%%%%%%%%%%%%%%%%%%%%%%%%%%%%%%%%

%define coordinate space and wavevector space
xmax=500*mum;                       %maximum value in coordinate space
X=linspace(-xmax,xmax,N);           %coordinate space
res=X(2)-X(1);                      %resolution in coordinate space
prange=2*pi/res;                    %wavevector range
P=linspace(-prange/2,prange/2,N);   %wavevector space

%specify the pump term and the phasematching term in Psi(r_s,r_i=0)
E0=pumpterm(w0,X,HG);                         %CALL pumpterm function
[F0 Ftilde]=phasematchingterm(X,P,phi,L,kp); %CALL phasematchingterm func.

%create the slit functions
[W T B] = CreateSlits(X,d,delta);

%Compute the signal probability distribution conditioned on an idler photon
%detection. Two loops scan r_ix and r_iy with resolution idlerres.
idlerres=2*res; if speed==1 idlerres=10*res; end
fmax=3*wf;
Rx=-fmax:idlerres:fmax;
Ry=Rx+ctrfbr;
lengthComp=length(Rx)^2;                        %length of computation

%initialize the results of the integrals
PT=zeros(N);PB=PT;PTprime=PT;PBprime=PT;PWprime=PT;
iteration=0;
for rix=Rx
    ri.x=rix;
    for riy=Ry
        ri.y=riy;
        iteration=iteration+1;
        disp(iteration/lengthComp*100);         %degree of completion
```

```
E=zeros(N);F=E;                          %initialize E and F

% We need to compute F(r_s-r_i) and E(r_s+r_i). For a given value
%of r_i, these function are identical to F0(r) and E0(r) up to a
%translation in coordinate space. In order to computer F and E, we
%thus move the center the matrix F0(r) at r=r_i and the center of
%the matrix E0(r) at r=-r_i.

b=centering(ri,N,res);                   %CALL centering function
                                         %(not shown in thesis)
%move the center of F0 at r=r_i, and the center of E0 at r=-r_i
F(b.Xbox,b.Ybox)  =F0(b.Xbox0,b.Ybox0);
E(b.Xbox0,b.Ybox0)=E0(b.Xbox,b.Ybox);

%Define the conditional modes after the slits
PsiCond=F.*E;
PsiW=W.*PsiCond;
PsiT=T.*PsiCond;
PsiB=B.*PsiCond;

%Apply a two-dimensional fft to the conditional mode after the
%slits to obtain the far-fiels interference pattern.
PhiT=fft2(PsiT);
PhiB=fft2(PsiB);
PhiW=PhiT+PhiB;

%calculate the optical fiber function
phix=exp(-rix.^2/2/wf^2);
phiy=exp(-(riy-ctrfbr).^2/2/wf^2);
phi2=abs(phix*phiy)^2;

%compute conditional probability distribution of
PTi=PsiT.*conj(PsiT)*phi2;               %near-field of top slit
PBi=PsiB.*conj(PsiB)*phi2;               %near-field of bottom slit
```

```
        PTprimei=PhiT.*conj(PhiT)*phi2;        %far-field of top slit
        PBprimei=PhiB.*conj(PhiB)*phi2;        %far-field of bottom slit
        PWprimei=PhiW.*conj(PhiW)*phi2;        %far-field of the two slits

        %perform the integrals
        PT=PT+PTi;
        PB=PB+PBi;
        PTprime=PTprime+PTprimei;
        PBprime=PBprime+PBprimei;
        PWprime=PWprime+PWprimei;
    end
end
PW=PT+PB;

%The marginal distributions
Nnorm=sum(sum(PWprime));  %normalization constant
MT=sum(PTprime')/Nnorm;
MB=sum(PBprime')/Nnorm;
MW=MT+MB;

%The visibility, predictability as a function of the environment
Visibility=     2*sqrt(MT.*MB)./MW;
Predictability= abs(MT-MB)./MW    ;

%Display relevant quantities;
rel.avgV=sum(MW.*Visibility);
rel.avgP=sum(MW.*Predictability);
rel.maxV=Visibility(ceil(N/2));
rel.varV=sum(MW.*(Visibility-rel.avgV).^2);
rel.varP=sum(MW.*(Predictability-rel.avgP).^2);
rel.OurEquality=rel.avgV^2+rel.avgP^2+rel.varV+rel.varP;
rel.ApparantViolation=rel.avgP^2+rel.maxV^2;
disp(rel)
```

```
%plotting the relevant quantities by calling function PlotRelevant
PlotRelevant(X,P*1E-5,E0,W,PW,PWprime,PT,PTprime,PB,PBprime,Visibility,...
    Predictability,MW,8,8,10);
```

### A.0.4 Function "pumpterm"

```
%%%Specify the joint wavefunction in the near-field
function E=pumpterm(w0,RS,HG,ri)

if ~exist('ri')    ri.x=0;ri.y=0; end

%pump field at the entrance facet of the crystal
Ex=exp(-(RS+ri.x).^2/8/w0^2);
Ey=exp(-(RS+ri.y).^2/8/w0^2);

if HG==1     Ey=(RS+ri.y).*Ey; end

E=Ex'*Ey;
```

### A.0.5 Function "phasematchingterm"

```
%%%%% Generate phase-matching term
function [F Ftilde]=phasematchingterm(X,P,phi,L,kp)

%specify the sinc function
a=0;
for py=P
    a=a+1;
    %note that sinc(x)=sin(pi*x)/(pi*x) in the version of MATLAB in which
    %this program was written. One must check if it is still the case.
    Ftilde(:,a)=sinc((phi+L/kp*(P.^2+py^2))/pi);
end

F=fftshift(fft2(Ftilde));
```

# Appendix B

# MATLAB code for computer-generated holograms

```
%%% Example program using the ComputeHologram function
% With 1024 pixels, our hologram takes about 0.35 second to calculate on an
% old laptop(to be compared with 0.23 second for the simple method of
% Davis et al.). Here, we only consider the time taken to calculate M and
% F, not the time taken to calculate the desired modes.

clc;clear;close all;

%Inputs with their suggested values
dp=16;%16           %Distance between two pixels on the SLM
pixels=512;%512     %Number of used pixels on one line of the desired mode
N=8;%8              %Number of pixels in one period of the grating
domain=dp*pixels;   %Length of the used domain of the SLM
w=600;%600          %Width of the desired mode in microns (near-field)

%Desired mode
%Superposition of LG modes (as shown in the paper)
LG1=LG_mode(-2,2,w,pixels,domain);LG1=LG1/sqrt(sum(sum(abs(LG1)^2)));
LG2=LG_mode(3,1,w,pixels,domain); LG2=LG2/sqrt(sum(sum(abs(LG2)^2)));
LG=LG1+LG2;inputMode=LG;
```

```
%Gaussian input beam (instead of a plane wave), for simulation purposes
gau=LG_mode(0,0,w*6,pixels,domain);

%Compute hologram (this takes around 350 ms)
OurHologram=ComputeHologram(inputMode,N);

% Display the hologram on the SLM
SingleKinoform(OurHologram,2,1);

% % or Display two holograms on one SLM (uncomment to try)
% TwoDisplaysOnSingleSLM(OurHologram,OurHologram',2,1);

% Transformed gaussian input beam, just after the hologram
PHI=gau.*exp(1i*OurHologram);

%Simulate the first order of diffraction of the SLM
PSI=fftshift(fft2(PHI,1024, 1024));      %Mode in the far-field of the SLM
mid=ceil(1024/2);
firstOrderx=mid+[round(-54):round(54)];
firstOrdery=mid+[round(-54):round(54)]+round(130*8/N);
I=PSI(firstOrderx,firstOrdery).^2;       %Intensity profile in first order
figure(2);imagesc(abs(I));               %Display intensity
axis image;colormap hot;
title('Intensity profile in the first order of diffraction')
```

### B.0.6 Function "ComputeHologram"

```
function Hologram=ComputeHologram(inputMode,N)

% program optimized for mode fidelity
% The grating is made of N pixels, where N is an integer.
% INPUTS
% inputMode:        desired mode in the near-field of the hologram
% N:                number of pixels in one period of the blazed grating
%
```

```
% OUTPUT
% Hologram:         Hologram as displayed on the SLM

% Number of pixels on one line of the desired mode
N2=size(inputMode);pixels=N2(1);

% Create grating pattern
step=2*pi/N;saw=[0:step:2*pi-step];nbsaw=floor(pixels/N);tgra=zeros(pixels);
grating=[]; for i=1:nbsaw     grating=[grating saw];end
grating(length(grating):pixels)=0;for i=1:pixels    tgra(i,:)=grating;end

% Generate sinc function
X=linspace(0,1,100000);y=sinc(X);

% Generate a table for the sinc inverse function
%(duration of 20 ms on a bad laptop)
t=0; g=10000-1;    yy=round(y*g);
for i=1:length(y)    if yy(i)==g-t
        t=t+1;        sincinverse(g-t+2)=i/length(y);
end;                 end

% Normalize the hologram profile such that the maximum is 1
inputMode=inputMode/max(max(abs(inputMode)))+1E-20;

% Time-efficient computation of the M function with the inverse sinc
M=1-sincinverse(ceil(abs(inputMode)*length(sincinverse)));

% Calculate hologram with Eq. 4 in the paper
F=angle(inputMode)-pi*M;
Hologram=mod(tgra+F,2*pi).*M;
```

### B.0.7 Function "LG_mode"

```
%Function that calculates an LG mode with azimuthal number l and radial
%number p. Its width is w, and it is calculated over the region "domain"
```

```
%with a number of pixels equal to pixelsXpixels.
%This function is not optimized for speed.

function LG = LG_mode(l,p,w,pixels,domain)

if ~exist('domain')   domain=1000E-6;   end
if ~exist('pixels')   pixels=64;        end

X=linspace(-domain,domain,pixels);
Y=linspace(-domain,domain,pixels);

a=0;
LG = zeros(length(X),length(Y));

for x=X
    a=a+1;ii=0;
    for y=Y
        ii=ii+1;
        rho=sqrt(x^2+y^2);     phi=atan2(x,y);
        LG(a,ii)=(rho*sqrt(2)/w)^(abs(l))*exp(-rho^2/w^2)*...
        L_polynomial(p,abs(l),(2*rho^2/w^2))*exp(1i*l*phi);
    end
end

%Calculate the Laguerre polynomial
function LaguerreL = L_polynomial(p,l,x)

L1= 0; LaguerreL= 1;
    for i= 1 : p
        L0= L1; L1= LaguerreL;
        LaguerreL= ((2* i- 1+ l- x).* L1- (i- 1+ l).* L0)/ i;
    end
```

# Bibliography


[1] J. Leach, **E. Bolduc**, D. J. Gauthier, and R. W. Boyd, "Secure information capacity of photons entangled in many dimensions," *Physical Review A*, vol. 85, no. 6, p. 060304, 2012.

[2] J. Z. Salvail, M. Agnew, A. S. Johnson, **E. Bolduc**, J. Leach, and R. W. Boyd, "Full characterization of polarization states of light via direct measurement," *Nature Photonics*, vol. 7, pp. 316–321.

[3] **E. Bolduc**, N. Bent, E. Santamato, E. Karimi, and R. W. Boyd, "Exact solution to simultaneous intensity and phase masking with a single phase-only hologram," *Optics Letters*, 2013.

[4] **E. Bolduc**, J. Leach, and R. Boyd, "The secure information capacity of photons entangled in high dimensions," in *Quantum Information and Measurement*, Optical Society of America, 2012.

[5] **E. Bolduc**, J. Leach, and R. W. Boyd, "The secure information capacity of photons entangled in high dimensions," in *Frontiers in Optics 2012/Laser Science XXVIII*, p. FTh4B.7, Optical Society of America, 2012.

[6] **E. Bolduc**, J. Leach, F. Miatto, G. Leuchs, and R. Boyd, "How to achieve high visibility and high which-way information in a single experiment," in *Physics of Quantum Electronics*, 2013.

[7] R. Menzel, D. Puhlmann, A. Heuer, and W. P. Schleich, "Wave-particle dualism and complementarity unraveled by a different mode," *Proceedings of the National Academy of Sciences*, vol. 109, no. 24, pp. 9314–9319, 2012.

[8] R. Menzel, A. Heuer, D. Puhlmann, K. Dechoum, M. Hillery, M. Spähn, and W. Schleich, "A two-photon double-slit experiment," *Journal of Modern Optics*, vol. 60, no. 1, pp. 86–94, 2013.

[9] J. S. Lundeen, B. Sutherland, A. Patel, C. Stewart, and C. Bamber, "Direct measurement of the quantum wavefunction," *Nature*, vol. 474, no. 7350, pp. 188–191, 2011.

[10] J. S. Lundeen and C. Bamber, "Procedure for direct measurement of general quantum states using weak measurement," *Physical review letters*, vol. 108, no. 7, p. 070402, 2012.

[11] B.-G. Englert, "Fringe visibility and which-way information: An inequality," *Physical review letters*, vol. 77, no. 11, pp. 2154–2157, 1996.

[12] N. Bohr, "Albert einstein: Philosopher-scientist," *Open Court, La Salle, Illinois*, pp. 200–241, 1949.

[13] W. K. Wootters and W. H. Zurek, "Complementarity in the double-slit experiment: Quantum nonseparability and a quantitative statement of bohr's principle," *Physical Review D*, vol. 19, no. 2, p. 473, 1979.

[14] G. Jaeger and A. Shimony, "Optimal distinction between two non-orthogonal quantum states," *Physics Letters A*, vol. 197, no. 2, pp. 83–87, 1995.

[15] B.-G. Englert and J. A. Bergou, "Quantitative quantum erasure," *Optics communications*, vol. 179, no. 1, pp. 337–355, 2000.

[16] D. M. Greenberger and A. Yasin, "Simultaneous wave and particle knowledge in a neutron interferometer," *Physics Letters A*, vol. 128, no. 8, pp. 391–394, 1988.

[17] O. Carnal and J. Mlynek, "Young's double-slit experiment with atoms: A simple atom interferometer," *Physical review letters*, vol. 66, no. 21, p. 2689, 1991.

[18] M. Arndt, O. Nairz, J. Vos-Andreae, C. Keller, G. Van der Zouw, and A. Zeilinger, "Wave–particle duality of c60 molecules," *nature*, vol. 401, no. 6754, pp. 680–682, 1999.

[19] M. Giustina, A. Mech, S. Ramelow, B. Wittmann, J. Kofler, J. Beyer, A. Lita, B. Calkins, T. Gerrits, S. W. Nam, *et al.*, "Bell violation using entangled photons without the fair-sampling assumption," *Nature*, 2013.

[20] P. D. Schwindt, P. G. Kwiat, and B.-G. Englert, "Quantitative wave-particle duality and nonerasing quantum erasure," *Physical Review A*, vol. 60, no. 6, p. 4285, 1999.

[21] C. H. Monken, P. S. Ribeiro, and S. Pádua, "Transfer of angular spectrum and image formation in spontaneous parametric down-conversion," *Physical Review A*, vol. 57, no. 4, p. 3123, 1998.

[22] H. D. L. Pires and M. van Exter, "Observation of near-field correlations in spontaneous parametric down-conversion," *Phys. Rev. A*, vol. 79, p. 041801, 2009.

[23] W. H. Peeters, J. J. Renema, and M. P. van Exter, "Engineering of two-photon spatial quantum correlations behind a double slit," *Physical Review A*, vol. 79, no. 4, p. 043817, 2009.

[24] K. Chan, J. Torres, and J. Eberly, "Transverse entanglement migration in hilbert space," *Physical Review A*, vol. 75, no. 5, p. 050101, 2007.

[25] H. D. L. Pires and M. van Exter, "Near-field correlations in the two-photon field," *Physical Review A*, vol. 80, no. 5, p. 053820, 2009.

[26] A. J. Scott, "Tight informationally complete quantum measurements," *Journal of Physics A: Mathematical and General*, vol. 39, no. 43, p. 13507, 2006.

[27] Y. Aharonov, D. Z. Albert, and L. Vaidman, "How the result of a measurement of a component of the spin of a spin-1/2 particle can turn out to be 100," *Physical review letters*, vol. 60, no. 14, p. 1351, 1988.

[28] N. Ritchie, J. Story, and R. G. Hulet, "Realization of a measurement of a ??weak value??," *Physical review letters*, vol. 66, no. 9, p. 1107, 1991.

[29] W. K. Wootters and W. H. Zurek, "A single quantum cannot be cloned," *Nature*, vol. 299, no. 5886, pp. 802–803, 1982.

[30] C. H. Bennett, G. Brassard, *et al.*, "Quantum cryptography: Public key distribution and coin tossing," in *Proceedings of IEEE International Conference on Computers, Systems and Signal Processing*, vol. 175, New York, 1984.

[31] A. K. Ekert, "Quantum cryptography based on bell's theorem," *Physical review letters*, vol. 67, no. 6, pp. 661–663, 1991.

[32] N. J. Cerf, M. Bourennane, A. Karlsson, and N. Gisin, "Security of quantum key distribution using d-level systems," *Physical Review Letters*, vol. 88, no. 12, p. 127902, 2002.

[33] D. Gabor, "A new microscopic principle," *Nature*, vol. 161, no. 4098, pp. 777–778, 1948.

[34] J. P. Kirk and A. L. Jones, "Phase-only complex-valued spatial filter," *JOSA*, vol. 61, no. 8, pp. 1023–1028, 1971.

[35] J. A. Davis, D. M. Cottrell, J. Campos, M. J. Yzuel, and I. Moreno, "Encoding amplitude information onto phase-only filters," *Applied optics*, vol. 38, no. 23, pp. 5004–5013, 1999.

[36] V. Arrizón, U. Ruiz, R. Carrada, and L. A. González, "Pixelated phase computer holograms for the accurate encoding of scalar complex fields," *JOSA A*, vol. 24, no. 11, pp. 3500–3507, 2007.